ENERGETICS OF NONLINEAR GENERATION OF HARMONICS THROUGH THE INTERACTION OF AN INTERNAL WAVE BEAM WITH A MODEL OCEAN PYCNOCLINE

A Thesis

Presented to the Faculty of the Graduate School

of Cornell University

in Partial Fulfillment of the Requirements for the Degree of

Master of Science

by

Anil Abdullah Aksu

February 2016

ENERGETICS OF NONLINEAR GENERATION OF HARMONICS THROUGH THE INTERACTION OF AN INTERNAL WAVE BEAM WITH A MODEL OCEAN PYCNOCLINE

by Anil Abdullah Aksu

This thesis/dissertation document has been electronically approved by the following individuals:

Diamessis,Peter J. (Chairperson)

Jenkins,James Thomas (Minor Member)

© 2016 Anil Abdullah Aksu

ALL RIGHTS RESERVED

ABSTRACT

The internal wave beam are generated by the interaction of the barotropic tides with topography [58]. The beams propagate from lower layer of the ocean to the pycnocline and interacts with it, generating harmonics. The interaction includes two significant physical processes which may cause or contribute to the harmonics generation. One of those processes is the internal wave beam overlap between the incident wave beam and the reflecting wave beam. The other physical process is the wave refraction caused by the stratification in the BV frequency which is the buoyancy frequency.

In this study, 2-D direct numerical simulation (DNS) has been performed to simulate harmonics generation. The spectral multidomain penalty method is used as the numerical method. This has allowed us to obtain higher resolution and higher accuracy results inside the pycnocline by ranging the subdomain height in the vertical direction. As a result of DNS, the perturbation pressure field p' and the velocity field $\vec{u}$ are obtained. This raw data is postprocessed to analyze the total energy transferred to the harmonics. The result of the post-processing shows that there is a peak of energy transmission in harmonics for the non-dimensional pycnocline thickness $h/\lambda_x = 0.1$ where h is the pycnocline thickness and λ_x is the wavelength of the primary frequency wave in x direction, in terms of the non-dimensional pycnocline strength $r = N_{max}/N_1$ which is the ratio of the maximum BV frequency inside the pycnocline to the lower layer BV frequency. In total, It is tested on five different $r = 2, 4, 6, 8, 10$ values for two different Reynolds numbers $Re = 530, 5300$. First, it was analyzed for $Re = 530$

and the results showed that the energy transmission is largely impacted by the viscous loss. To reduce the effect of the viscous dissipation, the Reynolds number is increased by the factor of 10 and the same analysis is performed again.

To clarify the understanding of the simulation results even further, an analytical model for the viscous loss is derived. The model relates the viscous loss to the BV profile and it helps to observe why the transmission peak occurs. Additionally, the nonlinear interaction is analytically modelled which shows the generation is mainly caused by the incident and the reflecting internal wave beam interation.

BIOGRAPHICAL SKETCH

The author was born on October 13 1989 in Ankara, Turkey. He did his 4-year undergraduate studies at Bogazici University in the Department of Civil Engineering and Mechanical Engineering. His graduation project was on numerical soluion of the nonlinear wave equation using radial basis functions. In 2013 he came to Cornell University and started the Master of Science program in Environmental Fluid Mechanics Hydrology and conducted research under the supervision of Professor Peter Diamessis on nonlinear interaction of the internal waves with the model oceanic pycnocline, which is the subject of this thesis.

This thesis is dedicated to my friends and Professors in Turkey for supporting me while I was struggling with certain difficulties and giving me worldclass education.

ACKNOWLEDGEMENTS

I would like to warmly thank Professor Peter Diamessis for giving me the opportunity to come to Cornell and teaching me computational fluid dynamics. He was a careful advisor, I learnt the importance of the scientific presentation from him. I would also like to thank Professor James Jenkins for teaching me continuum mechanics during my last summer eagerly in our meetings. Moreover, I would like to acknowledge Professor Teoman Pekoz for his advices on my career decisions.

TABLE OF CONTENTS

Biographical Sketch . . . iii
Dedication . . . iv
Acknowledgements . . . v
Table of Contents . . . vi
List of Tables . . . viii
List of Figures . . . ix

1 Introduction **1**
1.1 Background and Literature Review . . . 1
1.2 Background: Internal Waves . . . 9
1.2.1 The Bouyancy Frequency . . . 9
1.2.2 Boussinesq Internal Waves . . . 10
1.2.3 The Ray Paths and Group Velocities . . . 12
1.2.4 Critical Level of Reflection . . . 14
1.2.5 Harmonic Generation . . . 15
1.2.6 Objectives . . . 17

2 Simulation and Problem Configuration **18**
2.1 Governing Equations . . . 18
2.2 Numerical Method . . . 19
2.3 Simulation Description . . . 21
2.4 Governing Nondimensional Parameters . . . 22

3 Postprocessing Pressure and Velocity Data **25**
3.1 Band-pass Filtering . . . 27
3.2 Radial Basis Function Interpolation . . . 28
3.3 The IWB Path . . . 31
3.4 Triangular Region . . . 33
3.4.1 Energy Balance . . . 34
3.4.2 Viscous Dissipation . . . 36
3.5 Pycnocline downstream of entry zone . . . 38
3.6 Reflection Region . . . 38

4 Analytical Models **39**
4.1 Analytical Model for Viscous Decay Along Internal Wave Beam Path . . . 39
4.2 Analytical Model for Harmonic and Mean Flow Generation for Free Slip Surface Reflection Case . . . 44
4.3 The Analytical Model for The Harmonics Generation inside the Pycnocline . . . 48

5 Results **57**
5.1 Energy Evolution along IWB Path 57
5.2 Energy Balance inside The Triangular Region 60
5.3 Numerical and Analytical Viscous Decay Models 64
5.4 First Reflection 65
5.5 Energy Flux Evolution inside The Pycnocline 68
5.6 Re-Radiating Energy from Pycnocline 74

6 Discussion **76**

7 Conclusion and The Future Work **81**
7.1 Conclusion 81
7.2 Future Work 82

A Supplementary Figures **84**

B The Virtaul Forcing Region **95**

Bibliography **96**

LIST OF TABLES

2.1 The Simulation Parameters for $Re = 530$. 23
2.2 The Simulation Parameters for $Re = 5300$. 24

5.1 The energy budget table for $Re = 530$ 61
5.2 The energy budget table for $Re = 5300$ 62

LIST OF FIGURES

1.1 Sample (a) temperature, (b) salinity and (c) Buoyancy frequency profiles. In summer, there are three temperature maxima (the near-surface temperature maximum [NSTM], Pacific Summer Water [PSW] and Atlantic Water), two temperature minima (the remnant of the previous winter's surface mixed layer and Pacific Winter Water [PWW] and halocline is the strong vertical gradient in salinity profile) from www.polarresearch.net 2
1.2 Internal waves in the Sulu Sea between Malaysia and Philippines. From www.internalwaveatlas.com 3
1.3 Snapshots of density surfaces for $\epsilon k u_0/\omega = 0.5$ and various values of ϵ. The horizontal and vertical scales are nondimensionalized such that the bottom topography has a height proportional to $\cos x$ and internal tide rays are inclined at 45° [4]. 5
1.4 Internal wave beams generated by oscillating cylinder.[2] 13
1.5 Incident and reflecting ray paths of the internal waves 14
1.6 The group velocity in z direction for $r = 6$ and $h/\lambda_x = 0.1$ 16

2.1 Exploded simulation grid around the pycnocline for $r = 6$ $h/\lambda_x = 0.1$. 21
2.2 Simulation description. 22

3.1 The schematics of the regions of analysis. 26
3.2 The critical level of reflection for $r = 6$ and $h = 0.1$. 34
3.3 The control volume in triangular region. 35

4.1 The schematic illustration of the incident and the reflecting Beam for the case of reflection off a free slip surface [7]. 44
4.2 BV frequency profile for $r = 6$ and $h/\lambda_x = 0.1$ and the reflection Level at which $N(z_r) = \omega$. 48

5.1 Energy flux profile on the center of the Gaussian forcing region for $r = 6$ and $h/\lambda_x = 0.1$, $Re = 530$ 58
5.2 Energy flux along the internal wave beam path (IWB) for $r = 6$ and $h/\lambda_x = 0.1$, $Re = 530$ 59
5.3 Total energy flux along the internal wave beam path (IWB) for $r = 6$ and $h/\lambda_x = 0.1$, $Re = 530$ vs $Re = 5300$ 60
5.4 Energy flux evolution inside the triangular region $r = 6$ and $h/\lambda_x = 0.1$, $Re = 530$ 62
5.5 Energy flux evolution along IWB for $Re = 5300$ a) $r = 2$, $h/\lambda_x = 0.1$ b) $r = 4$, $h/\lambda_x = 0.1$ 63
5.6 Analytical and numerical viscous dissipation for $r = 4$ and $h/\lambda_x = 0.1$, $Re = 530$ 65

5.7 Analytical and numerical viscous dissipation for $r = 2$ and $h/\lambda_x = 0.1$, $Re = 530$ 66
5.8 The group velocity profile in z direction for $r = 2, 4, 6, 8, 10$. . . . 67
5.9 The evolution of the reflecting energy in lower Layer for $r = 6$ and $h/\lambda_x = 0.1$,$Re = 530$. 68
5.10 The energy distridution of the primary frequency wave for $r = 6$ and $h/\lambda_x = 0.1$ and $Re = 530$. 69
5.11 Energy flux evolution inside pycnocline for $Re = 530$ a) $r = 2$, $h/\lambda_x = 0.1$ b) $r = 4$, $h/\lambda_x = 0.1$ c) $r = 6$, $h/\lambda_x = 0.1$ d) $r = 8$, $h/\lambda_x = 0.1$ e) $r = 10$, $h/\lambda_x = 0.1$. $s = 0$ corresponds to entry of pycnocline downstream. 71
5.12 Energy flux evolution inside pycnocline for $Re = 5300$ a) $r = 2$, $h/\lambda_x = 0.1$ b) $r = 4$, $h/\lambda_x = 0.1$ c) $r = 6$, $h/\lambda_x = 0.1$ d) $r = 8$, $h/\lambda_x = 0.1$ e) $r = 10$, $h/\lambda_x = 0.1$.$s = 0$ corresponds to entry of pycnocline downstream. 73
5.13 BV frequency profile for $r = 6$ and $h/\lambda_x = 0.1$ and The Top and The Bottom Reflection Levels at which $N(z_r) = 2\omega$. 74
5.14 The reradiating energy flux from the pycnocline for $r = 2, 4, 6, 8, 10$, $h/\lambda_z = 0.1$ and $Re = 530$. 75
5.15 The reradiating energy flux from the pycnocline for $r = 2, 4, 6, 8, 10$, $h/\lambda_z = 0.1$ and $Re = 5300$. 75

6.1 xz-contours of mean horizontal velocity $< u >$, normalized by its maximum observed magnitude in space, (a) at $t/T = 30$ for T01, and (b) at $t/T = 45$ for T07, in the wave reflection zone. The prediction by inviscid weakly nonlinear theory19 for a same wave geometry as T01, is shown in (c). The reflecting surface is at the top boundary of each contour plot and the centerline of the wave beam intersect with the surface at x = 0. The superimposed white dashed line is the contour of temporally averaged local intensity of wave kinetic energy $\rho_0(< u^2 > + < w^2 >)/2$ at 120%of the corresponding value on the centerline of the incident (reflected) beam outside the reflection zone [7]. 77
6.2 Mean energy intensity for $Re = 530$ a) $r = 2$, b) $r = 4$. 78

A.1 Viscous dissipation inside triangular region numerical vs analytical Calculations for $Re = 530$ a) $r = 2$, $h/\lambda_x = 0.1$ b) $r = 4$, $h/\lambda_x = 0.1$ c) $r = 6$, $h/\lambda_x = 0.1$ d) $r = 8$, $h/\lambda_x = 0.1$ e) $r = 10$, $h/\lambda_x = 0.1$. 85
A.2 Mean pressure velocity product for $r = 2$ and $Re = 530$a) PU_{Total}/PU_{max}, b) PU_{ω}/PU_{max}, c) $PU_{2\omega}/PU_{max}$ magnified, d) PU_{mean}/PU_{max} magnified. 86

A.3 Mean pressure velocity product for $r = 4$ and $Re = 530$ a) PU_{Total}/PU_{max}, b) PU_{ω}/PU_{max}, c) $PU_{2\omega}/PU_{max}$ magnified, d) PU_{mean}/PU_{max} magnified. 87
A.4 Mean Pressure Velocity Product for $r = 6$ and $Re = 530$ a) PU_{Total}/PU_{max}, b) PU_{ω}/PU_{max}, c) $PU_{2\omega}/PU_{max}$ magnified, d) PU_{mean}/PU_{max} magnified. 88
A.5 Mean pressure velocity product for $r = 8$ and $Re = 530$ a) PU_{Total}/PU_{max}, b) PU_{ω}/PU_{max}, c) $PU_{2\omega}/PU_{max}$ magnified, d) PU_{mean}/PU_{max} magnified. 89
A.6 Mean pressure velocity product for $r = 2$ and $Re = 5300$ a) PU_{Total}/PU_{max}, b) PU_{ω}/PU_{max}, c) $PU_{2\omega}/PU_{max}$ magnified, d) PU_{mean}/PU_{max} magnified. 90
A.7 Mean pressure velocity product for $r = 4$ and $Re = 5300$ a) PU_{Total}/PU_{max}, b) PU_{ω}/PU_{max}, c) $PU_{2\omega}/PU_{max}$ magnified, d) PU_{mean}/PU_{max} magnified. 91
A.8 Mean pressure velocity product for $r = 6$ and $Re = 5300$ a) PU_{Total}/PU_{max}, b) PU_{ω}/PU_{max}, c) $PU_{2\omega}/PU_{max}$ magnified, d) PU_{mean}/PU_{max} magnified. 92
A.9 Mean pressure velocity product for $r = 8$ and $Re = 5300$ a) PU_{Total}/PU_{max}, b) PU_{ω}/PU_{max}, c) $PU_{2\omega}/PU_{max}$ magnified, d) PU_{mean}/PU_{max} magnified. 93
A.10 Mean energy Intensity for $Re = 530$ a) $r = 2$, b) $r = 4$, c) $r = 6$, d) $r = 8$, e) $r = 10$. 94

CHAPTER 1

INTRODUCTION

1.1 Background and Literature Review

The ocean consists of layers with different mass densities at different depths. Differential heating is one of the causes leading to this stratification. The sea surface is exposed to radiative heating more than lower layers. The heat at the sea surface does not diffuse easily to the lower layer and, as a result, the difference in heating creates differences in temperatures that result in the density stratification. Below a layer near the surface that is mixed by the wind, the density increases rapidly with depth in a layer known as the pycnocline. When the fluid density is continuously stratified, oscillatory motion will occur due to differences in buoyancy [2]. In contrast to surface waves, internal waves are not restricted to the interface; they can also propagate vertically [1][32]. They can be generated by an underwater vehicle or flow over topography. The underwater vehicle may leave a turbulent wake behind, and the wake generates internal waves. The internal waves generated by an underwater vehicle may carry coherent information about the vehicle [33].

This study focuses on an internal wave beam as a surrogate for the higher mode internal waves driven when a barotropic tidal current interacts with the topography. Barotropic flows are those in which the density gradient is aligned with the pressure gradient, so that it does not contribute to the vorticity evolution [1]. The fate of the energy carried by the internal waves generated by this current is investigated. Such barotropic tidal currents are generally considered to be the driving mechanism for vertical motions of the ocean surface [4][24].

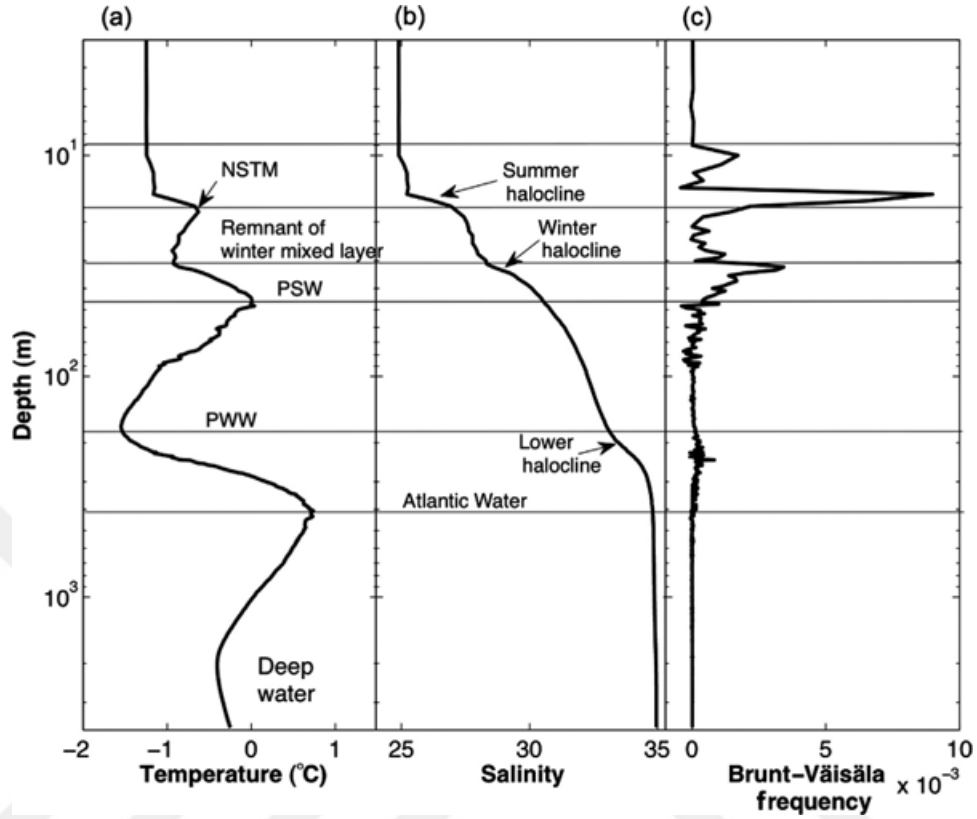

Figure 1.1: Sample (a) temperature, (b) salinity and (c) Buoyancy frequency profiles. In summer, there are three temperature maxima (the near-surface temperature maximum [NSTM], Pacific Summer Water [PSW] and Atlantic Water), two temperature minima (the remnant of the previous winter's surface mixed layer and Pacific Winter Water [PWW] and halocline is the strong vertical gradient in salinity profile) from www.polarresearch.net

The barotropic currents are nearly uniform, except near the seabed, where bottom friction is responsible for the non-uniformity[4]. Additionally, there are baroclinic currents that are also comparable with barotropic currents. These currents are driven by the vorticity field created by the vector product of the pressure gradient and the density gradient.

An initially barotropic tidal current results in baroclinic motion when it inter-

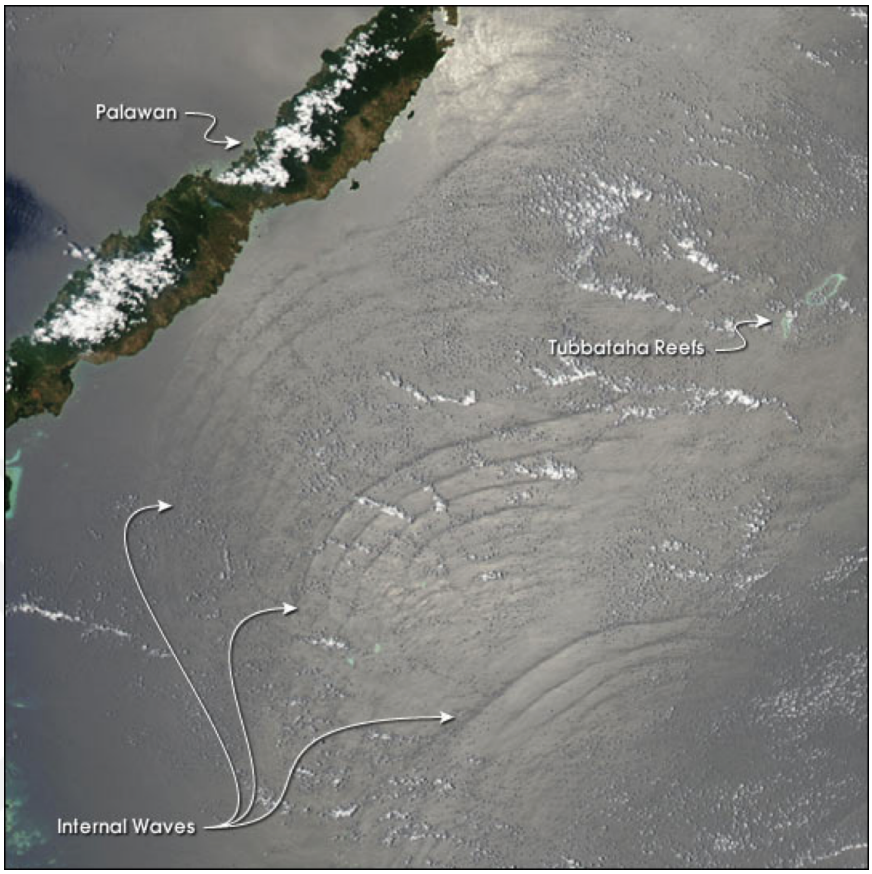

Figure 1.2: Internal waves in the Sulu Sea between Malaysia and Philippines. From www.internalwaveatlas.com

acts with the topography. During the conversion of the energy from barotropic to the baroclinic currents, internal wave beams radiate from the topography. In this, 10% of the total energy of the currents is transferred to the internal wave [4]. This energy transfer could have a considerable impact on the mixing of total energy in the deep ocean [4]. The internal waves produced do not generally have the forcing frequency. Depending on the topography, internal waves with higher frequency than the forcing frequency are also produced and the disturbance generated by the tidal frequency will contain higher frequencies. The normalized slope, ϵ, of the topography is

$$\epsilon = kh_0/\alpha. \tag{1.1}$$

Note that h_0 is a measure of the topographical height, and k is the wavenumber for a sinusoidal topography [4][23]. The term α comes from the stream function formulation of the linearized equation with the Coriolis frequency f and the buoyancy frequency N. In terms of the parameters given and the wave frequency ω, it is calculated as follows,

$$\alpha = (\frac{\omega^2 - f^2}{N^2 - \omega^2})^{1/2}. \tag{1.2}$$

The Coriolis frequency and the buoyancy frequency also sets limits for the wave frequency ω. The radiating internal waves are only generated if $f < \omega < N$ [4]. This limit implies that higher modes do not propagate long distances; because they become evanescent so they decay in the absence of viscosity [21], as its frequency exceeds the buoyancy frequency.

A topography that has a near or supercritical slope, where the critical slope occurs when $\epsilon = 1$ for $\epsilon > 1$, it is supercritical slope , will produce a high mode content. Only the low modes travel far from the region in which they are generated. The topographic generation mechanism should be introduced into the numerical model used to study the evolution of an internal wave beam. However, it is difficult implement anything other than a flat boundary. Instead, a virtual forcing region could be used to approximate the topographic mechanism. In addition to the generation mechanism, the propagation of the internal wave is also an open question. Internal waves can behave linear or nonlinear way. One of the interesting observation of the nonlinearity is the formation of solitary wave, for example, in the Bay of Biscay [27]. Solitary internal waves are

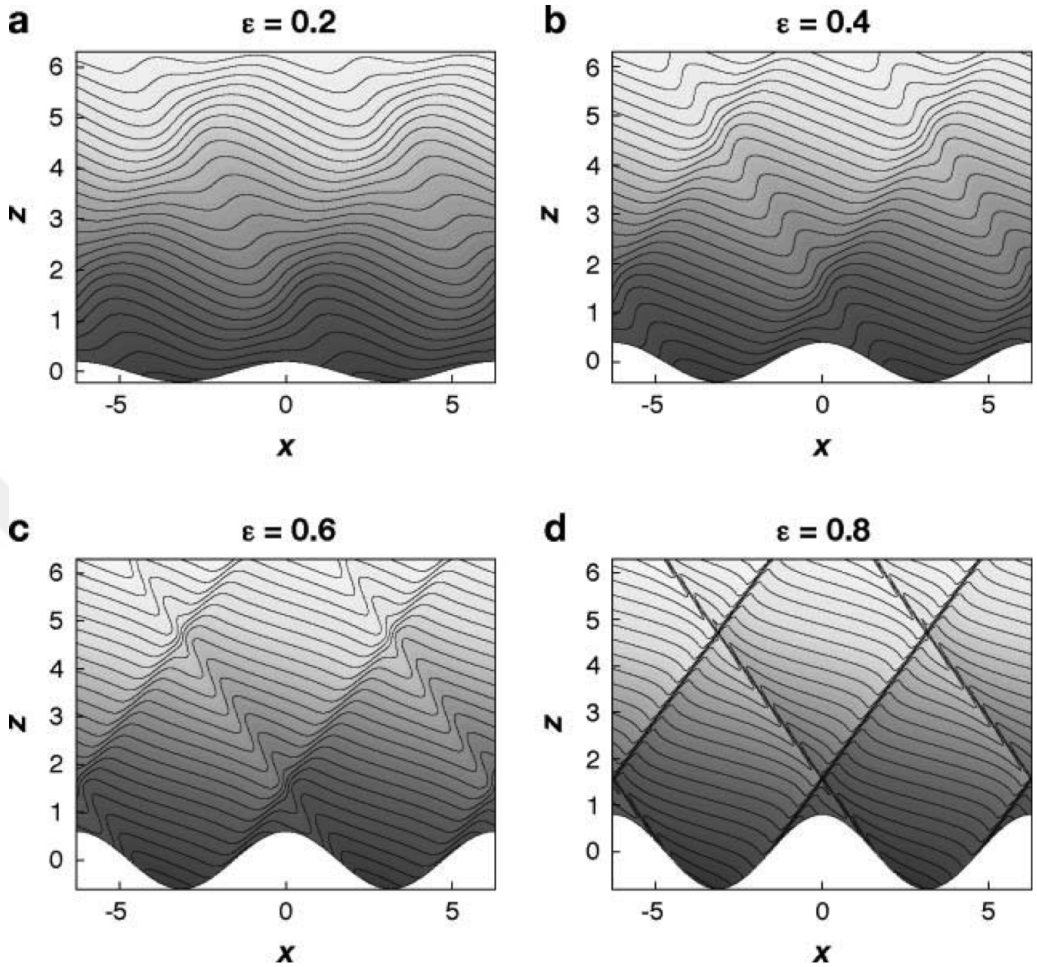

Figure 1.3: Snapshots of density surfaces for $\epsilon k u_0/\omega = 0.5$ and various values of ϵ. The horizontal and vertical scales are nondimensionalized such that the bottom topography has a height proportional to $\cos x$ and internal tide rays are inclined at 45° [4].

also obtained numerically [13][14][15]. The existence of solitary waves is one aspect of nonlinearity; in such waves, nonlinearity balances the effect of dispersion [1][11][40]. However, nonlinearity may also generate higher harmonics [5][8][22][28][25] and mean flows [12][5][9].

One important example of harmonic generation occurs when internal wave beams overlap [5]. Internal waves with the same frequency, interacting nonlinearl in a linear stratification where buoyancy frequency is constant, generate a

first higher harmonic [28][17][25]and a mean flow [5][28][12]. It is also known that two internal waves with frequencies ω_1 and ω_2 that interact nonlinearly in a linear stratification generate internal waves with frequencies $\omega_1 + \omega_2$ and $\omega_1 - \omega_2$ [5]. Based on this observation, if two interacting internal waves have the same frequency, their nonlinear interaction in a linear stratification generates a mean flow and the first higher harmonic. However, if the frequency of the first higher harmonic is less than the buoyancy frequency, the first higher harmonic can be evanescent. Nonetheless, the mean flow still survives. This type of mean flow generation is observed numerically [7][28] and in the laboratory [12].

A similar generation mechanism is also observed in nonuniform stratification. In this case, an internal wave beam changes its direction of propagation [10]. Thas is, nonuniform stratification causes the internal wave to change its orientation, called refraction. Some researchers also suspect that the wave refraction causes harmonic generation [9][19]. Another effect associated with nonuniform stratification is energy accumulation due to the change in magnitude of group velocities of the internal wave, which are the velocities at which the wave energy propagates. This effect may be the wave refraction.

In the presence of pycnoline, the effect of nonlinerity and the harmonic generation is numerically [3][22] and expermentally [22][9][13] observed. It is also shown that depending on the angle of incidence on pycnocline, harmonics generated inside the pycnocline may not reflect back to the lower layer where the internal wave beam is excited. The presence of the reflection level for harmonics determines if the harmonics generated inside the pycnocline reflects back to the lower layer.

The optimal configuration for the harmonics generation in terms of the pyc-

nocline strength, defined as $r = N_{max}/N_1$ where $N_{max]}$ is the maximum buoyancy frequency and N_1 is the buoyancy frequency at the bottom of the lower layer is verified experimentally [22], numerically [3] and analytically [3] for 45° angle of incidence to the pycnocline horizontally. At that optimal configuration, the energy transferred to the first higher harmonics is maximized for an orientation of 45°. Furhtermore, Issues of stability like wave breaking due to shear or convective instability are important to the phenomena studied here. They are also addressed by other researchers [5][18][31][26][20]. But stability analysis is outside the scope of this work.

Briefly, the propagation of the internal wave beam energy is analyzed along the internal wave beam path, which is the path of the ray below the pycnocline. It is mostly governed by the linear theory. Viscous decay of the wave is observed before it enters into the pycnocline and nonlinear generation of higher harmonics and solitary waves are observed after the wave enters the pycnocline. The interaction with the pycnocline is accompanied by two significant process: wave beam to change its orientation, and overlap of the incident and the reflecting wave beams. The first reflection occurs when the incident wave beam reaches a critical level of reflection. In the overlap region, it interacts with the incident wave beam. The nonlinear interaction between the incident and the reflecting internal wave beams could be the generation mechanism for the higher harmonics. For the propagation angle analyzed, the higher harmonics are trapped inside the pycnocline. However, higher harmonics could also reflect back into lower layer in a different configuration. The nonlinear interactions of the incident and the reflecting wave beams may also generate a mean flow. Because the mean flow does not exhibit spatial oscillations, it survives further inside the pycnocline. Higher wave numbers possess higher spatial gradients and, therefore,

higher viscous dissipation.

The purpose of this study is to understand the generation mechanism of the harmonics and the wave-induced mean flow inside the pycnocline. Another goal is to quantify how much energy goes into the harmonics and the mean flow. It is also important to note that viscous dissipation must be accounted for. This may be influenced by the variation of the buoyancy frequency in the model oceanic pycnocline, when we analyze the energy budget. The desired results of the analysis are the optimal configuration for the generation of higher harmonics and a description of their subsequent propagation.

1.2 Background: Internal Waves

1.2.1 The Bouyancy Frequency

Because of the density gradient inside the ocean, if a fluid particle with a particular potential density moves upward where it starts being pulled downward due to gravity around lighter fluid, and moves downward to a point where it starts being pushed upwards by the heavier fluid around, this causes oscillatory behaviour with a particular frequency called Brunt-Vaisala Frequency[1]. Under the Boussinesq approximation, The density field $\varrho(\vec{x}, t)$ inside the ocean could be model as a sum of the constant density part ρ_0, the background stratification part $\bar{\rho}(z)$ and the perturbation part $\rho(\vec{x}, t)$. The Boussinesq approximation suggests that the density perturbation is negligible and $\rho_0 >> \bar{\rho}(z) >> \rho(\vec{x}, t)$, as long as it does not affect the bouyancy forces. For an ocean mentioned above, the motion could be modelled as follows [1],

$$\rho_0 \frac{\mathrm{d}^2\delta_z}{\mathrm{d}t^2} = g\frac{\mathrm{d}\bar{\rho}}{\mathrm{d}z}\delta_z. \tag{1.3}$$

where δ_z is an infinitesimal vertical displacement of the fluid parcel form the balance state. It could be formulated more compactly,

$$\frac{\mathrm{d}^2\delta_z}{\mathrm{d}t^2} + N^2\delta_z = 0. \tag{1.4}$$

After arranging the terms in the equation (1.3), the BV frequency N can be obtained as follows,

$$N^2 = -\frac{g}{\rho_0}\frac{\mathrm{d}\bar{\rho}}{\mathrm{d}z}. \tag{1.5}$$

Based on this, it could be concluded that the vertically disturbed fluid particle will oscillate with the angular frequency N [1].

1.2.2 Boussinesq Internal Waves

Even though in ocean scale 50 – 500 km, the Coriolis effect is considerable, in the simplified case we are trying to simulate, we can neglect the Coriolis effect. It will complicate the physics we are trying to understand unnecessarily. Other than that, under Boussinesq approximation, the density change is not considered in the momentum equation but it is considered in the energy equation. Note that the energy equation comes from the thermal energy equation which assumes the speed of sound goes to infinity. Under this formulation, the momentum equation feels the effect of the stratification via the gravitational forces ρg. In 2-D case, the momentum equations could be formulated as follows,

$$\rho_0 \frac{Du}{Dt} = -\frac{\partial p}{\partial x} + \mu \nabla^2 u. \tag{1.6}$$

$$\rho_0 \frac{Dw}{Dt} = -\frac{\partial p}{\partial z} + \mu \nabla^2 w - g\rho. \tag{1.7}$$

Note that the pressure p is the dynamic pressure, the hydrostatic part $\bar{p}$ is cancelled out in the balance with the background density $\bar{\rho}$. The simplified energy equation modified by the density stratification is given as follows,

$$\frac{D\rho}{Dt} = -w\frac{\partial \bar{\rho}}{\partial z} + \kappa \nabla \rho \tag{1.8}$$

and the continuity equation is used,

$$\nabla \cdot \vec{u} = 0. \tag{1.9}$$

These are the governing equations used to model the internal wave generation numerically. However, to develop the linear theory, it should be linearized under simplifying assumption. The linear theory has some limitations, but it will give important insights about the governing physics.

To simplify the governing equations, Boussinesq approximation is commonly made. It assumes that the density stratification does not appear explicitly the momentum equations, but the energy equation [1]. Analyzing the behaviour of the small amplitude internal waves, the material derivative D/Dt could be replaced by $\partial/\partial t$. After that replacement and the stream function formulation, It could be reduced to a single equation[1],

$$[\partial_{tt}\nabla^2 + N^2\partial_{xx}]\psi = 0. \tag{1.10}$$

where $u = -\partial_z\psi$ and $w = \partial_x\psi$. Note that the viscous effects are also neglected for sake of the simplicity of the fundamental theory. Even though it does not account for the nonlinear effects, the linear theory explains important notions like the group velocities and the ray paths that could be derived from the diserpsion relation. However, it does not explain how the wave amplitude evolves. The dispersion relation shows how the wave frequency ω is related to the wavenumber vector $\vec{k}$. It could be derived by Fourier Transforming the equation(1.10), the corresponding dispersion relation can be written as follows,

$$\omega^2 = \frac{N^2 {k_x}^2}{\sqrt{{k_x}^2 + {k_z}^2}}. \tag{1.11}$$

Note that k_x and k_z are the wavenumber in x and z direction. This relation also determines a limit for the propagating wave. If $\omega < N$, the internal wave propagates. However, if $\omega > N$, the characteristic of the equation changes and the internal wave becomes evanescent so it decays exponentially. For the propagating internal wave, the velocity field u, w, the perturbation pressure field p and the perturbation density field ρ are obtained as follows[1],

$$u = -N\frac{k_z}{\sqrt{k_x^2 + k_z^2}}A_\xi \sin(\phi) \tag{1.12}$$

$$w = N\frac{k_x}{\sqrt{k_x^2 + k_z^2}}A_\xi \sin(\phi) \tag{1.13}$$

$$\rho = \rho_0\frac{1}{H}A_\xi \cos(\phi). \tag{1.14}$$

$$p = -\rho_0\frac{N^2}{k_x}\frac{k_x k_z}{k_x^2 + k_z^2}A_\xi \sin(\phi). \tag{1.15}$$

where $\phi = k_x x + k_z z - \omega t$ and A_ξ is the internal wave amplitude. In this study, these relations will be the foundation of postprocessing the simulation data as well. While analyzing the linear region, it will simplfy the analysis and form the basis for the energetics analysis. Particularly, using the time averaging over a one wave period helps us to differentiate the energy flux of the different frequencies. In our case, it will correspond to the differentiation between the primary wave signal and the harmonics signal which would be the integer multiple of the primary frequency ω. Besides, by time averaging over one wave period, it could also be shown that the bouyancy flux $\rho g w$ induced by an internal wave is equal to zero in the linear region. This will help us to analyze the energy budget in a simpler way.

1.2.3 The Ray Paths and Group Velocities

Using the dispersion relation, the group velocity vector $\vec{Cg}$ can be derived. The derivative of the frequency ω with respect to k_x will give the group velocity in

x-direction Cg_x,

$$Cg_x = \frac{\partial \omega}{\partial k_x} = \frac{N}{\sqrt{k_x^2 + k_z^2}} - \frac{N k_x^2}{\sqrt{(k_x^2 + k_z^2)^3}}. \tag{1.16}$$

The derivative of the frequency ω with respect to k_z will give the group velocity in z-direction Cg_z,

$$Cg_z = \frac{\partial \omega}{\partial k_z} = -\frac{N k_x k_z}{\sqrt{(k_x^2 + k_z^2)^3}}. \tag{1.17}$$

Based on those relations, it could be shown that the group velocity vector $\vec{Cg}$ and the wavenumber vector are orthogonal to each other. In the case of linear stratification where BV frequency N is constant, if the fluid at rest is forced by oscillating cylinder with $\omega < N$, it sends out the internal wave beams as in figure (1.4).

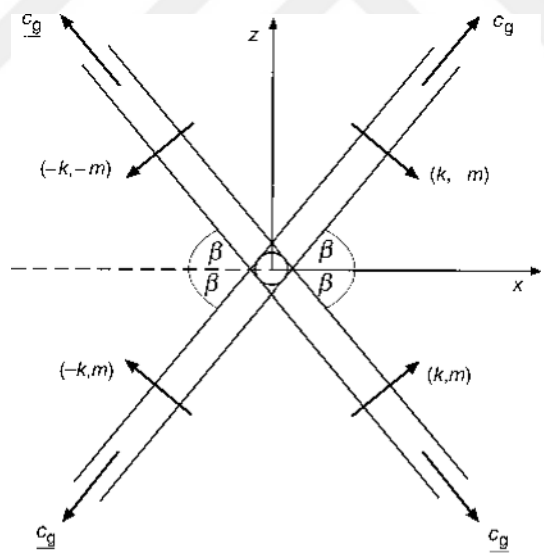

Figure 1.4: Internal wave beams generated by oscillating cylinder.[2]

Apart from the theoretical concerns, the group velocities could be tracked to observe the evolution of the wave amplitude numerically. In the absence of the background shear, the path that the wave amplitude follows could be derived by integrating the group velocities in time.

1.2.4 Critical Level of Reflection

In the case of the variable stratification, the group velocity vector $\vec{Cg}$ changes its direction and the magnitude. If it reaches to a point where the extrinsic frequency $\Omega = \omega - k_x\bar{U}$ matches the background BV frequency $N(z)$, the internal wave reflects. Note that $\bar{U}$ denotes the background flow. In the absence of the background flow $\bar{U}$, the extrinsic frequency Ω is equal to the intrinsic frequency ω. The reflecting part of the wave starts propagating downwards.

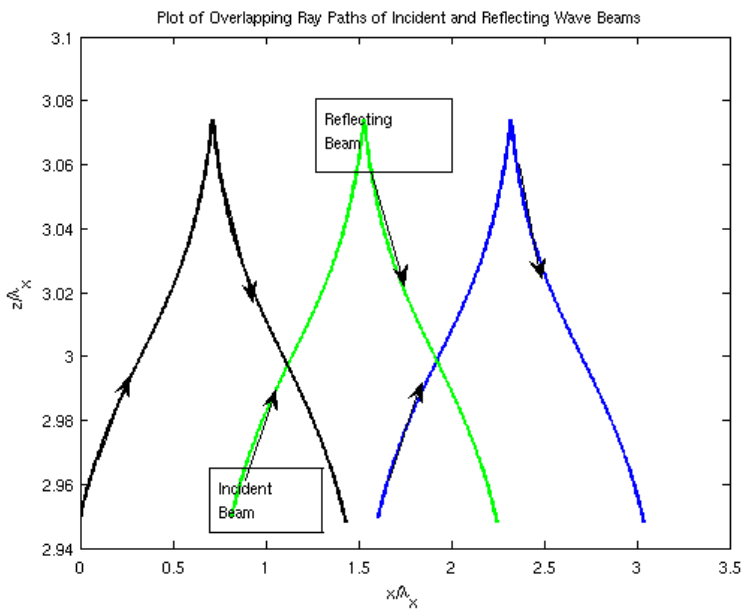

Figure 1.5: Incident and reflecting ray paths of the internal waves

Note that λ_z and λ_x are the wave lengths of the primary frequency wave in z and x directions respectively. Moreover, $z/\lambda_z = 0$ corresponds to the bottom of lower layer and $x/\lambda_x = 0$ corresponds to the point where the ray path tracked at the left edge of the internal wave beam enters into the pycnocline. In the model pycnocline in which we are trying to approximate the ocean stratification. The reflection levels are also encountered at upper layer of the pycnocline. It is not

expilicit in the equation (1.18), however the pycnocline thickness could be estimated by finding the level at which $N(z = z_0 - h/2) = (N_{max} + N_1)/2$ where h is the pycnocline thickness [3]. Moreover,

$$\frac{N^2(z)}{{N_1}^2} = (r^2 - \frac{1}{2})sech^2(\frac{z - z_0}{\delta_t}) + \frac{1}{2}(1 - tanh(\frac{z - z_0}{\delta_t})). \tag{1.18}$$

In this model pycnocline, $r = N_{max}/N_1$ shows the strength of the pycnocline. δ_t is a measure of the pycnocline thickness. z_0 is the centerline of the pycnocline. The reflection also causes the internal wave overlap which would lead to nonlinear interaction between the incident and the reflecting internal wave beam.

1.2.5 Harmonic Generation

In the variable stratification, the effect of nonlinearity is felt strongly around the pycnocline region. One of the nonlinear effect observed in that region is the higher order harmonics generation. The harmonics have the integer multiple of the primary frequency $n\omega$. Moreover, as a result of the nonlinear interaction caused by the density stratification, mean flow generation is also observed in the pycnocline. These nonlinear interactions are driven by the internal wave beam refraction and the internal wave beam overlap. The internal wave beam overlap is caused by the collision between the incident and the reflecting internal wave beam. It has been shown that the nonlinear interaction in colliding internal wave beams generate harmonis with frequencies with the sum of the and difference of primary frequency in the uniform stratification[5]. The difference of the primary frequency corresponds to mean flow. However, in the case

of variable stratification, internal wave beam refraction is also observed. Even though it may not be the primary generation mechanism, it could enhance the generation rate [3]. In the pycnocline region where the BV frequency changes sharply, the group velocity $\vec{Cg}$ changes orientation. It affects the flux of the internal wave energy.

$$\vec{F} = \vec{Cg} < E > . \tag{1.19}$$

where the total mean energy $< E > \propto A_{\xi}^{2}$. In inviscid case, when the internal wave field reaches the quasi-steady-state that the wave amplitude A_{ξ} is constant. The energy flux is from the source is also constant. If the group velocity decreases in some particular region, it leads to an accumulation of the total energy in that region.

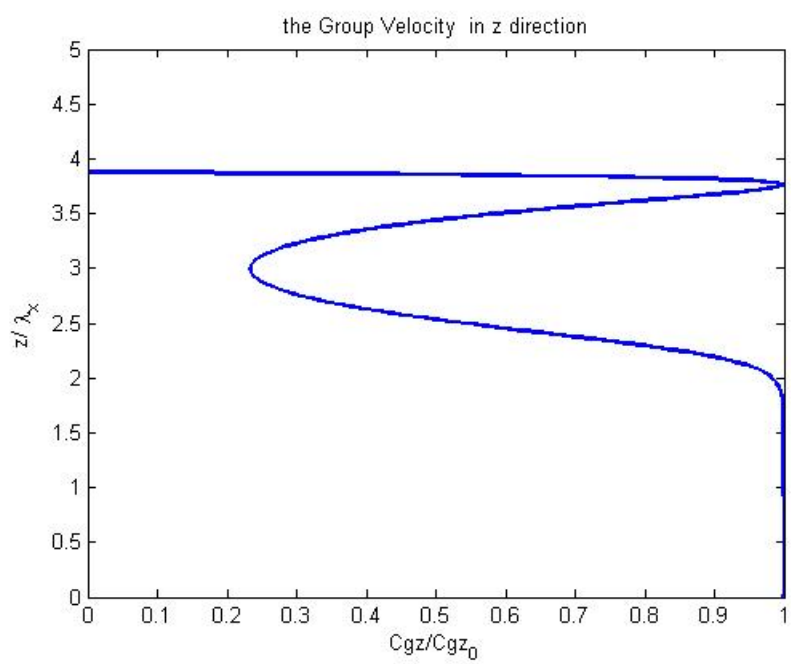

Figure 1.6: The group velocity in z direction for $r = 6$ and $h/\lambda_x = 0.1$

In our problem, this region corresponds to the overlap region in figure (1.5). Even though the internal wave beam refraction may not directly cause the har-

monics generation, it may enhance the generation rate by increasing the amount of the incident and the reflecting internal wave beam energy in the overlap region. However, in viscous case, the accumulation of the internal wave energy is reduced by the effect of the viscosity which is amplified in the pycnocline region.

1.2.6 Objectives

In this study, the objectives are focused on the generation mechanism of the harmonics and the mean flow when the incident internal wave beam interacts with the model oceanic pycnocline. It could be listed as:

1. Quantify nonlinear energy transfer from primary IWB frequency into other modes, which are harmonics and mean flow, upon incidence on pycnocline.
2. Focus on specific processes like reflection and refraction at different locations along IWB path.
3. Estimate transmission, absorption and primary and secondary reflection coefficients.
4. Analyze and Quantify the effect of viscous loss which will determine how far on downstream the waves will propagate.

CHAPTER 2

SIMULATION AND PROBLEM CONFIGURATION

2.1 Governing Equations

As stated earlier, to model the internal wave dynamics, Navier-Stokes Equation under Boussinesq approximation are used. However, simulating the barotropic tides interacting with the obstacle on the bottom boundary complicates the numerical implementation unnecessarily. Instead, a virtual forcing region is used to mimic the same generation mechanism. In total, the governing equations are two-dimensional Navier-Stokes equations and the density equation,

$$\frac{\partial \mathbf{u}}{\partial t} + \mathbf{u} \cdot \nabla \mathbf{u} = -\frac{1}{\rho_0} \nabla p + \mathbf{F}_g + \nu \nabla^2 \mathbf{u} + \mathbf{F}_u + \mathbf{S}_u, \tag{2.1}$$

$$\frac{\partial \rho}{\partial t} + \mathbf{u} \cdot \nabla(\rho + \bar{\rho}(z)) = \kappa \nabla^2 \rho + \mathbf{F}_\rho + S_\rho, \tag{2.2}$$

$$\nabla \cdot \mathbf{u} = 0 \tag{2.3}$$

where p and ρ denotes perturbation pressure and density respectively. Note that the gravity force acts in z direction:

$$\mathbf{F}_g = -g \frac{\rho}{\rho_0} \hat{k} \tag{2.4}$$

In this formulation, as in the theoretical formulation, ρ, p are the perturbation density and pressure respectively. $\mathbf{u} = (u, w)$ is the two-dimensional velocity field in $x - z$ coordinate system. Besides, $\mathbf{S}_u$ and S_ρ sponge layer terms are used to avoid the periodicity in x direction caused by the numerical method [6]. These terms leads to a decay of the velocity field at the boundaries. In x

direction, the Fourier series are used. As a result of it, the internal wave leaving the domian from the right edge turns back into the domain from the left edge. These Rayleigh-type sponge layer terms damp out the internal wave at the right boundary so that it does not propagate into the domain from the left edge. They are also used around the bottom boundary to avoid the reflection from the bottom boundary. However, they are not used around the top boundary. Moreover, $\mathbf{F_u}$ and F_ρ are virtual paddles simulate the forcing caused by the baroclinic tides (Appendix B). For top and bottom boundaries, homogeneous Neumann boundary conditions are applied for ρ. Homogeneous Dirichlet bounary conditions are used for all velocity component at the boundaries. Additionally, to avoid a reflection from the bottom boundary, sponge layer terms are also effective at the bottom boundary. However, at the top boundary, the free-slip boundary condition is used. Note that it was not directly set as a boundary condition on the boundaries in x direction, however it was implied by the presence of the sponge layer.

2.2 Numerical Method

In this particular problem, for the strong pycnoclines at which the background BV frequency is much bigger than that at the base of the lower layer, high resolution is required to capture the physics with an high accuaracy. Additionally, the domain geometry is simplifid by the substitution of the virtual forcing region which would enable to implement the numerical technique easily. Considering these issues, the two-dimensional multidomain penalty method is used. Initially, the model was intented for the localized high Reynolds number problems. In this method, as mentioned earlier, the Fourier series are used in the

horizontal and Legendre polynomials are used in vertical direction. The use of Legendre polynomials allows us to seperate the domain into subdomains in vertical so that the resolution could be increased around the region where the nonlinear effects are more pronounced. As for the implementation for the particular equation time splitting scheme is used. In the time splitting method, the convective terms are intergrated explicitly adn the diffusve terms are integrated implicitly [29][6]. Finally, the pressure Poisson equation is solved. The stability of the method is provided by both the spectral filtering and a multidomain penalty scheme which also help subdomains to communicate with each other.

2.3 Simulation Description

The main motivation behind the simulation is to quantify the amount of the energy deposited into harmonics and keep track of the evolution of it. For that purpose, the resolution inside the pycnocline is increased. It is done by decreasing the thickness of the subdomain, covering the pycnocline such that the number Gauss-Legendre-Lobatto points are kept the same for all subdomains.

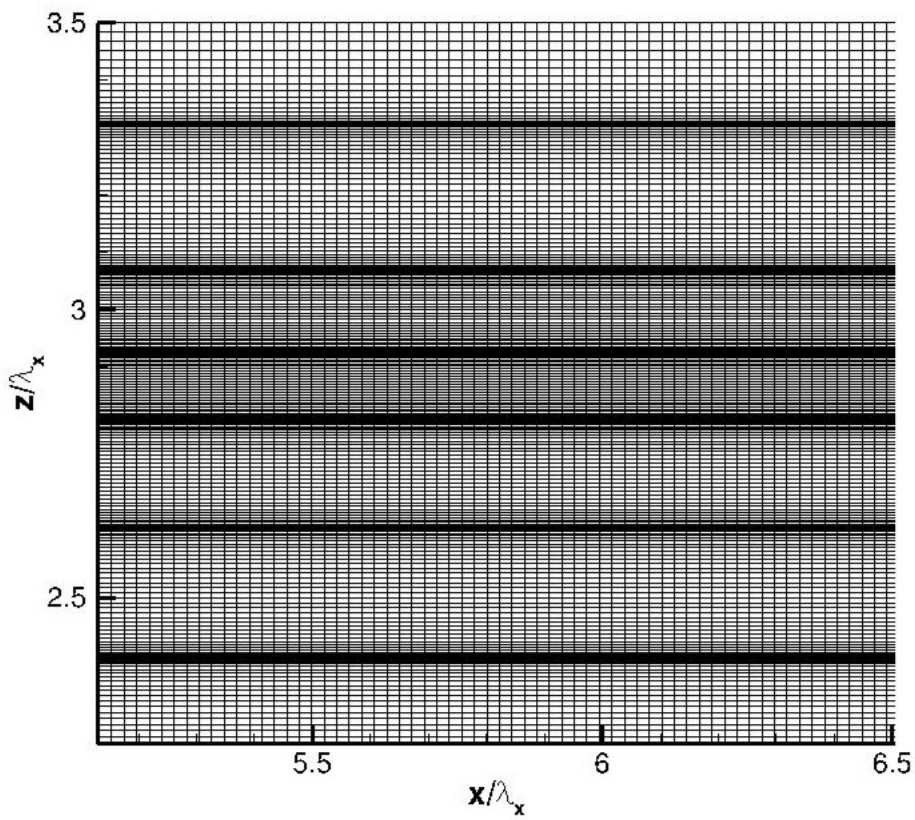

Figure 2.1: Exploded simulation grid around the pycnocline for $r = 6$ $h/\lambda_x = 0.1$.

The Internal wave beam is excited at a particular forcing region. The forcing region generates upward propagating internal wave beam. The upward prop-

agating internal wave beam reaches the pycnocline. For the particular case we are analyzing, the propagation direction is inclined at $\theta = 45°$ to the horizontal. Relying on the governing physics (see Chapter 1 Sec 1.2) , the harmonics will be trapped within the pycnocline for that angle. However the primary frequency internal wave reflects back into the lower layer. Besides, some part of the harmonics generated initially also leads to the generation of the primary frequency wave within the pycnocline. It radiates back into the lower layer.

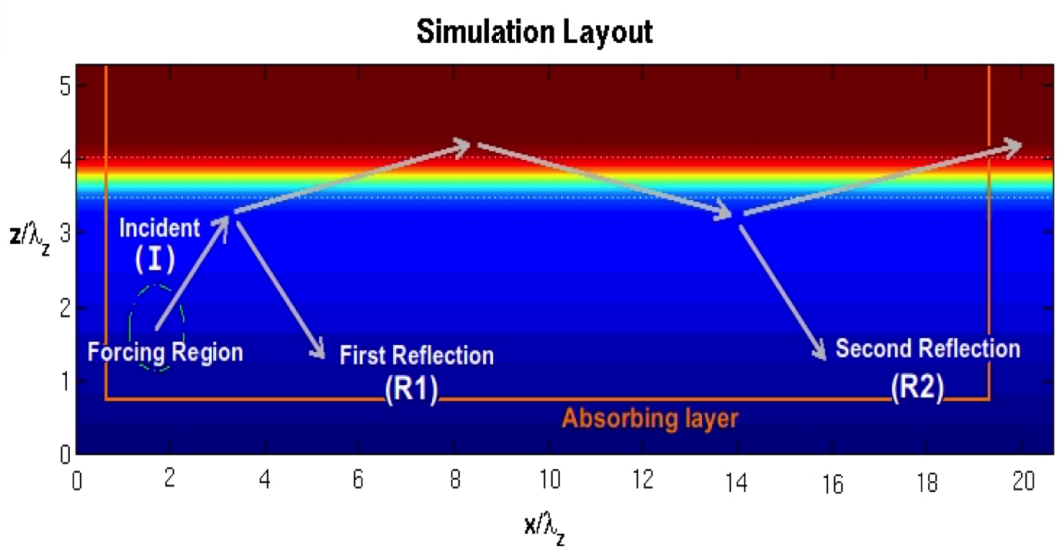

Figure 2.2: Simulation description.

2.4 Governing Nondimensional Parameters

To capture the physics we are trying to understand and to provide the stability of both physics and the numerical method, the choice of the nondimensional parameters plays key role. In this particular problem, the waves steepening due to nonlinearity should be avoided, this is set by the ratio A_ξ/λ_x. The other parameter which determines the effect of the nonlinearity is Reynolds number

$Re = U_{max}\lambda_x/\nu$ which controls if the flow is dominated by viscous forces or inertial forces. It could be kept same for all simulations. The choice of the Reynolds number is more important for the stability of the physics. Furthermore, the pycnocline strength could be measured as the ratio of the lower layer background BV frequency to the maximum BV frequency inside the pycnocline $r = N_{max}/N_1$. In that aspect, the thickness of the pycnocline also affects the physics of the problem both by increasing the viscous loss and the region of noninear interaction. For the given BV frequency profile in equation (1.18), δ_t is measure of pycnocline thickness. By adjusting that parameter the pycnocline thickness h could be arranged. The pycnocline thickness is nondimensionalized with respect to the wavelength in x direction λ_x. The analysis are done for the thin pycnocline case $h/\lambda_x = 0.1$ for all simulations.

r	2	4	6	8	10
h	0.1	0.1	0.1	0.1	0.1
δ_t	0.034	0.028	0.027	0.022	0.025
x_c	0.2	0.2	0.2	0.2	0.2
z_c	0.13	0.13	0.13	0.13	0.13
z_0	0.2625	0.2625	0.2625	0.2625	0.2625
λ_x	0.0875	0.0875	0.0875	0.0875	0.0875
ρ_0	1000	1000	1000	1000	1000
N_1	0.78	1.56	2.34	2.34	3.9
ν	10^{-7}	10^{-7}	10^{-7}	10^{-7}	10^{-7}
Num	512	512	512	512	512
Range	200-441	200-378	200-345	200-454	200-316
σ_x	0.1014	0.1014	0.1014	0.1014	0.1014
N_x	384	384	512	512	768
N_z	491	491	491	491	533

Table 2.1: The Simulation Parameters for $Re = 530$.

where measure of pycnocline thickness is δ_t, the coordinates of the center of the forcing pedal are x_c,z_c, the vertical coordinate of pycnocline center z_0, base BV frequency is N_1, kinematic viscosity is ν, the number of time steps is Num,

r	2	4	6	8	10
h	0.1	0.1	0.1	0.1	0.1
δ_t	0.034	0.028	0.027	0.022	0.025
x_c	0.2	0.2	0.2	0.2	0.2
z_c	0.13	0.13	0.13	0.13	0.13
z_0	0.2625	0.2625	0.2625	0.2625	0.2625
λ_x	0.0875	0.0875	0.0875	0.0875	0.0875
ρ_0	1000	1000	1000	1000	1000
N_1	0.78	1.56	2.34	2.34	3.9
ν	10^{-7}	10^{-7}	10^{-7}	10^{-7}	10^{-7}
Num	512	512	512	512	512
$Range$	200-447	200-417	300-443	200-423	300-414
σ_x	0.1014	0.1014	0.1014	0.1014	0.1014
N_x	384	384	512	512	768
N_z	491	491	491	491	533

Table 2.2: The Simulation Parameters for Re = 5300.

the time interval on which the quantities are time-averaged is $Range$, the deviation of the Gaussian forcing profile is σ_x, the number of simulation point in x direction is N_x, the number of simulation point in z direction is N_z.

CHAPTER 3

POSTPROCESSING PRESSURE AND VELOCITY DATA

After generating the perturbation pressure field p and the velocity field u in x-direction, w in z-direction, it should also be postprocessed to calculate how much energy goes to harmonics and the zeroth mode. Postprocessing addresses three important regions in the internal wave field which are IWB path, Pycnocline and Reflection zone. In each region, the product of the perturbation pressure and velocity vector is computed along the group velocity vector $\vec{Cg}$. To compute the total energy flux, it is integrated along the wavenumber direction $\vec{k} = k_x\hat{i}$, $k_z\hat{k}$ six wavelengths which covers the total energy as it has Gaussian forcing region leading to similar spatial distribuiton for pressure and velocity field. First region of analysis is the IWB path on which the primary wave caused by the gaussian forcing region is propagating. In this region, linear theory gives accurate results. To analyze the energy flux in this region, the ray paths of the primary wave beam can be tracked. The ray paths for the linear internal wave beam can be calculated by using the linear dispersion relation. Since we are tracking the wave packet, these velocities should be integrated in time,

$$\vec{x}(t) = \int \vec{Cg}dt \tag{3.1}$$

After the IWB path, the primary wave beam enters into tri-angular region where the non-linear interactions are more effective and harmonics and the zeroth mode flow is generated. In this region, the ray paths of the primary wave beam could still be tracked to see the evolution of the energy flux where it is defined as:

$$F = \int_{-3\lambda}^{3\lambda} < p(x,z,t), \vec{u}(x,z,t) > \vec{n}dl \tag{3.2}$$

where $\vec{n}$ is aligned in the direction of the upward propagating group velocity vector $\vec{Cg}$. A fraction of the energy flux reflects back into the lower layer. It could

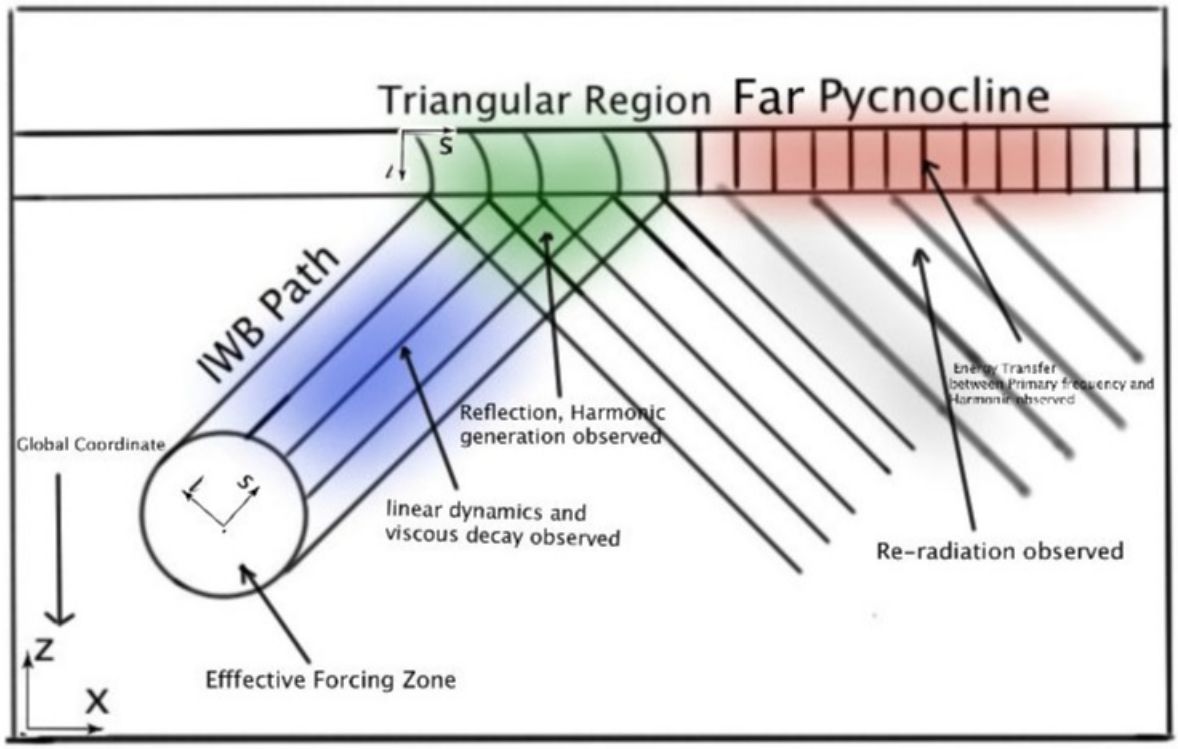

Figure 3.1: The schematics of the regions of analysis.

be tracked by following the reflecting group velocities. Note that the reflecting group velocities differ from the incident group velocities only by the sign of the group velocity in z direction. The part of the energy flux reflected back into the lower layer only shows linear behaviour. For the incident angle $\theta = 45°$, the harmonics don't reflect back into the lower layer as the background BV frequency N is smaller than any harmonic frequency. Because of that, the harmonic signal becomes evanescent in the lower layer. At the end of the triangular region, the energy flux enters into the downstream region of the pycnocline. In that region, the harmonic signal gets trapped for the particular angle of incidence. Furthermore, the primary wave and the harmonic signals follow more complicated Ray

paths. Taking that into account, to keep track of the energy flux evolution, calculating the energy flux on vertical control surfaces which covers the pycnocline could be a more efficient way of analyzing the energy flux evolution. However, the energy flux trapped in the pycnocline decays. It happens both due to viscosity and the re-radiation of the energy from the pycnocline. An efficient way of observing the energy flux is to integrate it over an horizontal control surface at the base of the pycnocline.

3.1 Band-pass Filtering

When the primary frequency wave beam interacts with the model pycnocline, harmonic and the zeroth mode generation is observed. To analyze the harmonics and the zeroth mode signal, the time series of the data can be Fourier transfomed in time. In our case, the Fourier transform in time will give distinct frequency peaks which are the integer multiples of the primary frequency. This property of the perturbation pressure and the velocity signal could be used to design the appropriate band-pass filter for this problem. If the frequency peaks are not distinct, Heavy-side function type band-pass filtering would lead to Gibb's oscillation, however in this case, it does not lead to that effect.

The Fourier transform of the velocity and the perturbation pressure signal can be band-pass filtered and back transformed. Note that since the filtering operation will be done numerically, there is no need to deal with the convolution integral in the time space. We can simply multiply the filter function $F_1(\omega)$ with the Fourier transform of the velocity field in time series $\hat{U}(\omega)$. Note that the filter function $F_1(\omega)$ is used to isolate the primary frequency signal and it is cen-

tered around the primary frequency ω_0, the filter function $F_2(\omega)$ is used to isolate first harmonic signal and it is centered around the first harmonic frequency $2\omega_0$, the filter function $F_0(\omega)$ is used to isolate zeroth mode signal and it is centered around the zeroth mode. The filtered x velocity signals are:

The Zeroth Mode Signal

$$\hat{U}_0(\omega) = \hat{U}(\omega)F_0(\omega). \tag{3.3}$$

The Primary Frequency Signal

$$\hat{U}_1(\omega) = \hat{U}(\omega)F_1(\omega). \tag{3.4}$$

The First Harmonic Signal

$$\hat{U}_2(\omega) = \hat{U}(\omega)F_2(\omega). \tag{3.5}$$

This filtering operation should be done on u velocity field, w velocity field and the perturbation pressure field p'. After filtering, the signal should be back-transformed into the time domain.

3.2 Radial Basis Function Interpolation

To make the interpolation more efficient, using all data from full field should be avoided. Instead, the data points in the particular neigbourhood should be used for the interpolation. For this purpose the radial basis function interpolation is an effective tool. In this method, we are trying to represent our function as a

sum of particular basis functions which are dependent on radial distance. In the code, multiquadric function which is defined as follows,

$$f(x, z; x_j, z_j) = \sqrt{(x - x_j)^2 + (z - z_j)^2 + c^2}. \tag{3.6}$$

Note that x_j and z_j are the coordinates of a particular data point for the basis function and also there is no particular formula for c. But, c value is usually computed as $2r_{min}$ where r_{min} is the minimum radial distance between the data points. The function we want to write as a sum of the basis functions can be written as follows,

$$u(x, z) = \sum_{j=1}^{N} \alpha_j f(x, z; x_j, z_j). \tag{3.7}$$

Note that α_j is the corresponding weight coefficient for each basis function. These coefficients will represent the time dependent part of the solution and they are implicitly calculated at each time step.

This implicit calculation will be described. Based on the definition above, at each time step, the velocity and the pressure at the data points can be written in terms of the radial basis functions as follows,

$$u(x_i, z_i) = \sum_{j=1}^{N} \alpha_j f(x_i, z_i; x_j, z_j). \tag{3.8}$$

Note that it is only x-velocity, but the same formulation is used for z-velocity and pressure. Let's write it in shorthand notation,

$$u_i = \sum_{j=1}^{N} \alpha_j f_{i,j}. \tag{3.9}$$

This can also be written as the following linear system for $N = 3$,

$$\begin{bmatrix} u_1 \\ u_2 \\ u_3 \end{bmatrix} = \begin{bmatrix} f_{1,1} & f_{1,2} & f_{1,3} \\ f_{2,1} & f_{2,2} & f_{2,3} \\ f_{3,1} & f_{3,2} & f_{3,3} \end{bmatrix} \begin{bmatrix} \alpha_1 \\ \alpha_2 \\ \alpha_3 \end{bmatrix} \tag{3.10}$$

Usually, the total number of data points N is approximately 200 in our simulation, but to show the method more compactly, here $N = 3$ is used. Besides, the velocity in x-direction u_i is the velocity data coming from the main solver, not the interpolated values. Those values are used in interpolation. This method also has one very useful property: $f_{i,j}$ values are independent of time. So, if we invert the matrix generated by $f_{i,j}$ values, we can use it for each time step. This operation will reduce the computational effort for the interpolation. Furthermore, if we multiply the velocity vector in equation (3.10) with the inverse of the matrix $f_{i,j}$ from left handside, we obtain α_j as follows,

$$\begin{bmatrix} f_{1,1} & f_{1,2} & f_{1,3} \\ f_{2,1} & f_{2,2} & f_{2,3} \\ f_{3,1} & f_{3,2} & f_{3,3} \end{bmatrix}^{-1} \begin{bmatrix} u_1 \\ u_2 \\ u_3 \end{bmatrix} = \begin{bmatrix} \alpha_1 \\ \alpha_2 \\ \alpha_3 \end{bmatrix} \tag{3.11}$$

Additionally, since the pressure is also generated at the same grid points by the main solver, the same inverted matrix could also be used for the interpolation of pressure. However, α_j are different for the pressure and the velocity in z-direction. Finally, the main purpose of the interpolation is to calculate the velocities and the perturbation on the points where the ray paths of the primary frequency wave beam. Let's denote the ray path points as x_r and z_r. If those coordinates are plugged into the interpolation function, the velocity and

the perturbation pressure can be obtained as follows,

$$u(x_r, z_r) = \sum_{j=1}^{N} \alpha_j f(x_r, z_r; x_j, z_j). \tag{3.12}$$

This can be also written as a linear system, however the matrix is not necessarily square. To write it simply, let's show the calculation for one point on the ray path,

$$u(x_r, z_r) = \begin{bmatrix} f_{r,1} & f_{r,2} & f_{r,3} \end{bmatrix} \begin{bmatrix} \alpha_1 \\ \alpha_2 \\ \alpha_3 \end{bmatrix} = \begin{bmatrix} f_{r,1} & f_{r,2} & f_{r,3} \end{bmatrix} \begin{bmatrix} f_{1,1} & f_{1,2} & f_{1,3} \\ f_{2,1} & f_{2,2} & f_{2,3} \\ f_{3,1} & f_{3,2} & f_{3,3} \end{bmatrix}^{-1} \begin{bmatrix} u_1 \\ u_2 \\ u_3 \end{bmatrix} \tag{3.13}$$

This formulation reduces the computational effort, as the product of $f_{r,i} f_{i,j}^{-1}$ can be generated once and stored for the rest of the postprocessing. Even though it requires matrix inversion, it is still cheaper than solving linear system at each time step.

3.3 The IWB Path

The main solver provides us with the data on the multidomain grid points given before (see Ch2 Section 3), however it does not coincide with the points on the ray paths of the primary wave beam. Therefore the data for the pressure and the velocity should be interpolated on the points of the ray paths of the internal wave beam.

The time averaged energy flux is integrated along the wave number vector $\vec{k}$ direction to get the full energy flux originating from the excitation zone. Integration limits are chosen in accordance with the Gaussian structure of the perturbation pressure and the velocity profile. This integration is defined as follows,

$$\int_{-3\lambda}^{3\lambda} < p(x,z,t), \vec{u}(x,z,t) > \vec{n}dl = \int_{-3\lambda}^{3\lambda} (\frac{1}{T}\int_{0}^{T} p(x,z,t)\vec{u}(x,z,t)dt)\vec{n}dl \tag{3.14}$$

Note that T is the period of the primary frequency ω and the unit normal vector $\vec{n} = \vec{Cg}/\,||Cg||$. Besides, time-averaging plays more important role when the energy flux inside the pycnocline is analyzed. It helps to differentiate the energy flux signal in between harmonics and the primary frequency wave. Besides, The linear theory for internal waves works sufficiently wll along the internal wave beam path. One of the consequences of the linear theory is that the velocity field and the perturbation density field are out of phase. The velocity field is given as follows,

$$u = N\frac{k_z}{\sqrt{k_x^2 + k_z^2}}A_\xi \sin(\phi) \tag{3.15}$$

$$w = N\frac{k_x}{\sqrt{k_x^2 + k_z^2}}A_\xi \sin(\phi) \tag{3.16}$$

Note that the incident beam phase $\phi = k_x x - k_z z - \omega t$ [1]. The corresponding perturbation density field is given as follows,

$$\rho = \rho_0 \frac{1}{H} A_\xi \cos(\phi). \tag{3.17}$$

where the characteristic depth $H = g/N_0^2$. As a result of it, the time averaged

bouyancy flux is negligible. It is calculated as follows,

$$\int_{-3\lambda}^{3\lambda} g < \rho(x,z,t), w(x,z,t) > \vec{n}dl = \int_{-3\lambda}^{3\lambda} g(\frac{1}{T}\int_{0}^{T} \rho(x,z,t)w(x,z,t)dt)\vec{n}dl \approx 0. \quad (3.18)$$

The time-averaged surface kinetice energy flux is calculated as shown in equation (3.14). The time-averaged Buoyancy flux is calculated as shown in equation (3.18) as it is evaluated in the lower layer, where the linear theory works sufficiently well in energy budget calculations, due to the orhogonality relation, it is very small so that it could be neglected. it could be said that evaluating only kinetic energy flux gives total energy flux along the internal wave beam path where the non-linerity is negligible.

3.4 Triangular Region

The generation of the harmonics and the zeroth mode structure is first observed in the triangular region. At the level where the BV frequency $N(z)$ matches the primary frequency ω, the internal wave beam reaches the critical level of reflection. When the wave reaches that level, all the wave reflects back into lower region. It causes the beam overlap where the incident and reflecting primary frequency wave beam overlaps, it is one of the phenomena which could cause the harmonics generation. Apart from this, the wave refraction is also stronger in this region, it could be associated with the harmonic generation. To analyze this region more clearly, it should be analyzed when this region reaches the quasi-steady-state. The quasi-steady-state refers to a state at which the wave amplitude reaches the steady-state. It will help to avoid the complications coming from transient effects.

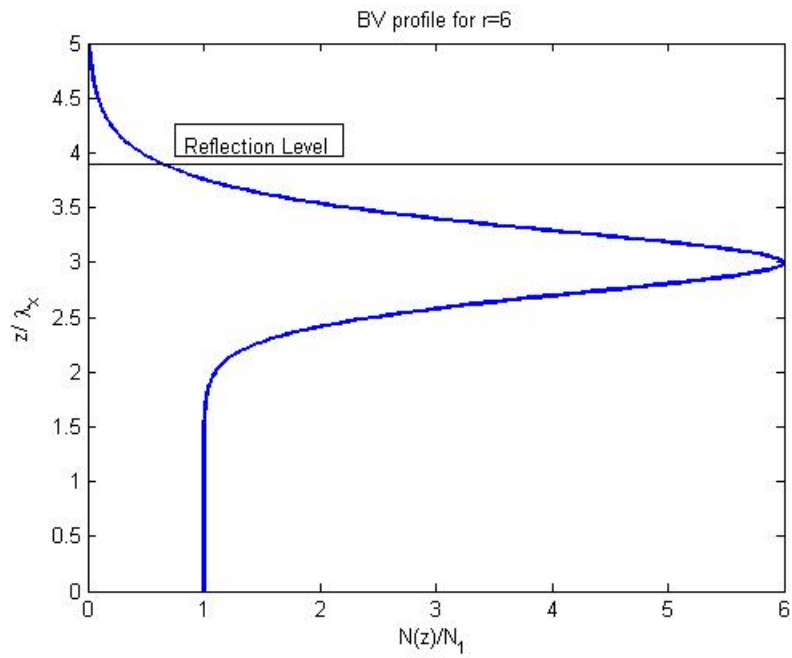

Figure 3.2: The critical level of reflection for $r = 6$ and $h = 0.1$.

3.4.1 Energy Balance

The energy flux comes from the incident primary frequency wave as product of the perturbation pressure field and the velocity field. Based on the control volume shown in the figure (3.3), when the system reaches the quasi-steady-state, the energy flux flowing into the control volume must be equal to the sum of the energy flowing out of the control volume and the viscous loss within the control volume. As shown in the figure(3.3), the energy influx due to the incident internal wave beam is the energy intake for the triangular zone. In the entry region of the incident wave beam, the effect of nonlinearity is negligible as the background BV frequency $N(z)$ is very close to constant in that region. Taking that into account and the linear theory, the buoyancy flux will be negligible from the incident wave beam as the perturbation density field and the velocity field is out of phase. When the perturbation and the velocity field product is

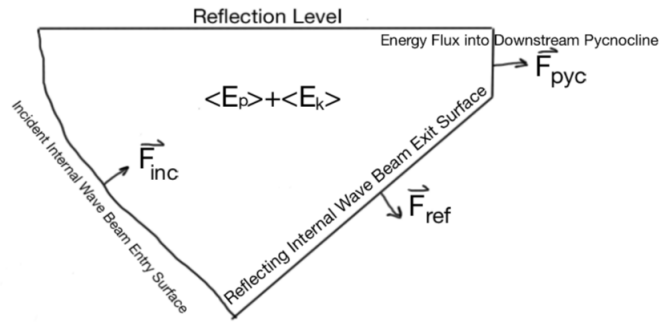

Figure 3.3: The control volume in triangular region.

time-averaged, it cancels out. The same argument applies to the energy outflux from the reflection zone. Except for the incident and the reflecting internal wave beam, some part of the energy flux goes inside the pycnocline and some part is lost due to viscous dissipation. In total energy balance in quasi-steady-state could be written as follows,

$$\frac{\partial}{\partial t}\int\int_{V_{tri}} < E_K > + < E_P > \mathrm{d}x\mathrm{d}z = \int_{Inc} < p(x,z,t)\vec{u}(x,z,t)\vec{n} > \mathrm{d}\eta - \int_{Ref} < p(x,z,t)\vec{u}(x,z,t)\vec{n} > \mathrm{d}\eta - \int_{Pyc} < p(x,z,t)\vec{u}(x,z,t)\vec{n} > \mathrm{d}\eta - \Phi. \tag{3.19}$$

where Φ denotes the total time averaged viscous dissipation inside the triangular zone. When the control volume, triangular region reaches the quasi-steady-state, the left handside of the equation cancels out. As a result the energy balance can be written as follows,

$$\int_{Inc} < \vec{F}_{inc}\vec{n} > \mathrm{d}\eta = \int_{Ref} < \vec{F}_{ref}\vec{n} > \mathrm{d}\eta + \int_{Pyc} < \vec{F}_{pyc}\vec{n} > \mathrm{d}\eta + \Phi. \tag{3.20}$$

Band-pass filtering is also applied to the energy flux inside the triangular zone to observe the harmonics generation. To observe the evolution of the energy flux, the group velocities are tracked inside the triangular zone as well. The

effect of nonlinearity is felt strongly inside the triangular zone, therefore the harmonics generation is considerable. To track the reflecting internal wave beam, the group velocities propagating downwards also generated. It also shows the evolution of how much energy is deposited into the reflecting internal wave beam inside the triangular zone.

3.4.2 Viscous Dissipation

Viscous dissipation should also be integrated numerically to compute the energy balance, however the path generated to follow the energy flux is curved inside the triangular region and most of the integration algorithms are developed for the rectangular grids. Taking that into account, the grid should be mapped onto a rectangular domain so that the integration algorithm used before will work accurately.

The coordinate is mapped from $x - z$ to $\xi - \eta$. The unit normals of the new coordinate system are $\vec{Cg}, \vec{k}$. In the $x - z$ coordinate system, the time averaged viscous dissipation is calculated as follows,

$$2\mu < D_{ij}D_{ij} >= 2\mu < ((\frac{\partial u}{\partial x})^2 + \frac{1}{2}(\frac{\partial u}{\partial z} + \frac{\partial w}{\partial x})^2 + (\frac{\partial w}{\partial z})^2) > \tag{3.21}$$

It should be integrated over the entire triangular region. Integral of the time averaged viscous dissipation is defined as,

$$\Phi = \int_{V_{tri}} 2\mu < D_{ij}D_{ij} > dxdz \tag{3.22}$$

Note that Φ denote total time averaged viscous dissipation and V_{tri} denotes the integration area in $x - z$ coordinates. To integrate it numerically, the integral

should be transfromed into $\xi - \eta$ coordinates system. Let's represent the new coordinate system numerically,

$$\xi(x,z) = I_N \xi(x,z) \tag{3.23}$$

$$\eta(x,z) = I_N \eta(x,z) \tag{3.24}$$

where I_N stands for an interpolation with N points. The interpolation points used for the perturbation pressure and the velocity could be used in this interpolation as well. Furthermore, when the time averaged viscous dissipation integral is mapped into $\xi - \eta$ coordinate system. The determinant of the jacobian appears as follows,

$$dxdz = det(\frac{\partial(x,z)}{\partial(\xi,\eta)})d\xi d\eta. \tag{3.25}$$

However, in this case, the determinant of the jacobian matrix can not be computed directly as x, z are not known as function of ξ, η. It could be indirectly computed as follows,

$$\frac{\partial(x,z)}{\partial(\xi,\eta)} = \begin{bmatrix} \frac{\partial x}{\partial \xi} & \frac{\partial x}{\partial \eta} \\ \frac{\partial z}{\partial \xi} & \frac{\partial z}{\partial \eta} \end{bmatrix} = \begin{bmatrix} \frac{\partial \xi}{\partial x} & \frac{\partial \xi}{\partial z} \\ \frac{\partial \eta}{\partial x} & \frac{\partial \eta}{\partial z} \end{bmatrix}^{-1}. \tag{3.26}$$

Based on this argument, the coordinate mapping of the integral can be represented as follows,

$$dxdz = \frac{1}{det(\partial(\xi,\eta)/\partial(x,z))} d\xi d\eta. \tag{3.27}$$

In total, the time averaged viscous dissipation integral can be written as follows,

$$\Phi = \int_{V_{tri}} 2\mu < D_{ij} D_{ij} > \frac{1}{det(\partial(\xi,\eta)/\partial(x,z))} d\xi d\eta. \tag{3.28}$$

After this mapping, The Romberg integration algorithm is used to calculate it with a good accuracy.

3.5 Pycnocline downstream of entry zone

In the downstream pycnocline region, the ray paths do not follow numerically trackable path differing form the triangular zone and IWB path. However, the primary wave, harmonics and mean flow propagate to the right along the horizontal. Considering that, calculating energy flux on a vertical cross-section which covers all pycnocline region gives the energy evolution and it is less complicated than keeping track of the group velocities as shown in the figure (3.1). Other than numerical aspects of the downstream pycnocline, physically in that region, nonlinerity shows its effect stronger which causes harmonics generation. However, harmonics do not reflect back into lower layer for the internal wave beam forming an angle $\theta = 45°$ with the horizontal as it reaches another critical level of reflection at the base of pycnocline where the background BV frequency $N(z_l) = n\omega$. However, the reflecting harmonics collide each other and may transfer their energy to the primary frequency wave which may re-radiate back into lower layer.

3.6 Reflection Region

In the reflection region, to observe the evolution of the reflecting energy flux, The downward propagating group velocities are tracked. the linear theory works accurately in the refleciton region. It is also expected to see viscously decaying energy flux along the reflection path.

CHAPTER 4

ANALYTICAL MODELS

4.1 Analytical Model for Viscous Decay Along Internal Wave Beam Path

The viscous dissipation within triangular region could be calculated numerically. However, to test the reliability of the numerical calculation, the same viscous dissipation analysis is performed analytically under simplified conditions. It can be used as a reference framework for the numerical model as well. Now, let's write the primary wave beam in $x - z$ coordinates and transform it into appropriate coordinate system so that the derivation of the model could be written more compactly [16]. For a plane wave, the velocity field is given as follows,

$$u = -N_0 \sin\theta A_\xi \sin\varphi. \tag{4.1}$$

$$w = N_0 \cos\theta A_\xi \sin\varphi. \tag{4.2}$$

where $\theta = \tan^{-1}(-k_z/k_x)$ and $\varphi = k_x x - k_z z - \omega t$. Note that there is a negative sign in front of k_z which simulates our case as it dictates the primary wave propagates upwards. This velocity field could be reduced to single component with the following mapping from $x - z$ to $\xi - \eta$. Under this mapping, η is in the direction of the wave number $\vec{k}$ and ξ is in the direction of the group velocity $\vec{Cg}$. The velocity field under this mapping reduces to the single component in ξ direction,

$$u_\xi = N_0 A_\xi \sin\varphi. \tag{4.3}$$

also $\varphi = k_\eta \eta - \omega t$ where $k_\eta = \sqrt{k_x^2 + k_z^2}$. The coordinate transform is done for plane wave, however the actual case is a wave beam. The velocity field for a plane wave could be used as a basis for the internal wave beam which could be formulated as follows,

$$u_\xi(\xi, \eta) = A(\xi, \eta) \sin \varphi. \tag{4.4}$$

Note that the base BV frequency N_0 is embedded into the wave amplitude $A(\xi, \eta)$. In our numerical simulations, the velocity field with respect to the coordinate system $\xi - \eta$ has a Gaussian profile. By using this fact, the wave amplitude could be decomposed as follows,

$$A(\xi, \eta) = A(\xi) \exp(\frac{-\eta^2}{2\sigma^2}). \tag{4.5}$$

After writing the wave beam in the transformed coordinate system, the viscous dissipation relation could be derived for quasi-steady-state form at which the wave amplitude is independent of time. Let's start from the time averaged energy equation,

$$\frac{\partial < E_K >}{\partial t} = -\frac{\partial < F_\xi >}{\partial \xi} - 2\mu < D_{ij} D_{ij} > . \tag{4.6}$$

where $F_\xi = C g_\xi < E >$ and the time averaged total energy $< E >$ could be computed as the sum of the time averaged potential energy $< E_p >$ and the time averaged kinetic energy $< E_k >$. From the linear theory, $< E_k > = < E_p >$ [1]. Based on that argument, the time averaged kinetic energy could be computed and multiplied by 2 to get the total time averaged energy as follows,

$$< E >= 2\frac{1}{T}\int_0^T \frac{\rho_0 u_\xi^2}{2} dt = \frac{1}{2}\rho_0 A^2(\xi)\exp(\frac{-\eta^2}{\sigma^2}). \tag{4.7}$$

Note that T is the period of the primary wave frequency ω. Before calculating the energy flux and the viscous dissipation, let's relate IWB half-width σ with the wavenumber k_η. One argument to relate them could be that the number of the wavelengths will fit under σ along the ray path even though the wavelength changes. Based on this, it could be assumed that $\sigma k_\eta = \sigma_0 k_{\eta 0}$. Note that σ_0 and $k_{\eta 0}$ are the initial deviation and the wavenumber. Under that assumption, the deviation σ could be implicitly written as function $k_\eta(\xi)$. Now, let's calculate the viscous dissipation term $2\mu < D_{ij}D_{ij} >$ [30]. The strain rate tensor D_{ij} could be calculated as follows in the transfomed coordinate system,

$$D_{ij} = \begin{bmatrix} \frac{\partial u_\xi}{\partial \xi} & \frac{1}{2}\frac{\partial u_\xi}{\partial \eta} \\ \frac{1}{2}\frac{\partial u_\xi}{\partial \eta} & 0 \end{bmatrix}. \tag{4.8}$$

Now, using the strain rate tensor, let's calculate the inner product of the strain tensor by itself $D_{ij}D_{ij}$,

$$D_{ij}D_{ij} = (\frac{\partial u_\xi}{\partial \xi})^2 + \frac{1}{2}(\frac{\partial u_\xi}{\partial \eta})^2. \tag{4.9}$$

The time averaging of the inner product of the strain rate tensor by itself gives the following expression,

$$< D_{ij}D_{ij} >= (\frac{1}{2}(\frac{\partial A}{\partial \xi})^2 + \frac{\eta^2}{4\sigma^4}A^2 + \frac{1}{4}k_\eta^2 A^2)\exp(\frac{-\eta^2}{\sigma^2}). \tag{4.10}$$

Let's replace the terms back in equation (4.10),

$$\frac{1}{2}\frac{\partial(\rho_0 A^2(\xi) C g_\xi(\xi))}{\partial \xi}\exp(\frac{-\eta^2}{\sigma^2}) = -\mu((\frac{\partial A}{\partial \xi})^2 + \frac{\eta^2}{2\sigma^4}A^2 + \frac{1}{2}k_\eta^2 A^2)\exp(\frac{-\eta^2}{\sigma^2}). \tag{4.11}$$

To simplify it even further, let's integrate it in η direction,

$$\int_{-\infty}^{\infty} \frac{1}{2}\frac{\partial(\rho_0 A^2(\xi) C g_\xi(\xi))}{\partial\xi} \exp(\frac{-\eta^2}{\sigma^2}) + \mu((\frac{\partial A}{\partial\xi})^2 + (\frac{\eta^2}{2\sigma^4} + \frac{1}{2}k_\eta^2)A^2) \exp(\frac{-\eta^2}{\sigma^2}) d\eta = 0. \quad (4.12)$$

After integrating and simplifying the terms coming from the integration above, the equation reduces to the following ordinary differential equation,

$$\frac{1}{2}\frac{\partial(\rho_0 A^2(\xi) C g_\xi(\xi))}{\partial\xi} = -\mu(\frac{\partial A}{\partial\xi})^2 - \frac{\mu A^2}{2}(k_\eta^2 + \frac{1}{2\sigma^2}). \quad (4.13)$$

This form could also be further simplified if the left-hand side of the equation is expanded,

$$\rho_0 A \frac{\partial A}{\partial\xi} C g_\xi + \frac{\rho_0}{2} A^2 \frac{\partial C g_\xi}{\partial\xi} = -\mu(\frac{\partial A}{\partial\xi})^2 - \frac{\mu A^2}{2}(k_\eta^2 + \frac{1}{2\sigma^2}). \quad (4.14)$$

Let's divide both sides by $\rho_0 A^2 C g_\xi$,

$$\frac{1}{A}\frac{\partial A}{\partial\xi} + \frac{1}{2Cg_\xi}\frac{\partial Cg_\xi}{\partial\xi} = -\frac{\nu}{Cg_\xi}(\frac{1}{A}\frac{\partial A}{\partial\xi})^2 - \frac{\nu}{2Cg_\xi}(k_\eta^2 + \frac{1}{2\sigma^2}). \quad (4.15)$$

Note that after that division, the dynamic viscosity μ is replaced by the kinematic viscosity $\nu = \mu/\rho_0$. The derivative of the group velocity Cg_ξ could be calculated numerically using the equations (1.16) and (1.17). Let's define a new variable y to simplify the equation even further,

$$y = \log(\frac{A(\xi)}{A_0}). \quad (4.16)$$

Let's replace it back into the equation (4.15),

$$y' = -\frac{1}{2Cg_\xi}\frac{\partial Cg_\xi}{\partial\xi} - \frac{2\nu}{Cg_\xi}(y')^2 - \frac{\nu}{Cg_\xi}(k_\eta^2 + \frac{1}{2\sigma^2}). \quad (4.17)$$

where $y' = dy/d\xi$. Under the assumption that $\sigma k_\eta = \sigma_0 k_{\eta 0}$, the equation (4.17) could be written as follows,

$$y' = -\frac{1}{2Cg_\xi}\frac{\partial Cg_\xi}{\partial \xi} - \frac{2\nu}{Cg_\xi}(y')^2 - \frac{\nu k_\eta^2}{Cg_\xi}(\frac{1}{2(\sigma_0 k_{\eta 0})^2} + 1). \tag{4.18}$$

The wave number k_η could be written in terms of BV frequency profile by using the dispersion relation,

$$y' = -\frac{1}{2Cg_\xi}\frac{\partial Cg_\xi}{\partial \xi} - \frac{2\nu}{Cg_\xi}(y')^2 - \frac{\nu N^2 k_x^2}{Cg_\xi \omega^2}(\frac{1}{2(\sigma_0 k_{\eta 0})^2} + 1). \tag{4.19}$$

It is the final form of the ordinary differential equation to estimate the viscous loss along the internal wave beam path. Except for the numerical results, it gives also important insight about the physics governing the problem. From the equation (4.19), it could be said that the viscous dissipation is affected strongly by the strength of the pycnocline. Nonetheless, it should also be noted that this equation has limitations. First, it can not capture the reflecting part of the primary frequency wave beam. Moreover, it can not include the non-linear effects. These limitations distort the result in some cases we analyzed where the reflection is too strong. In terms of non-linearity, it is still a good estimate as in most of our simulations the non-linear effects are relatively weak compared to the primary frequency wave propagation. The model captures the viscous decay alon IWB and inside the triangular region. Along IWB, the nonlinear effects are negligibly small and it is very weak inside the triangular region. As a result of this, the analytical approximation and the fully numerical computations give close results (see Figure A.1).

4.2 Analytical Model for Harmonic and Mean Flow Generation for Free Slip Surface Reflection Case

The beam overlap is one of the generation mechanism for zeroth mode evolution and the harmonics generation, however the overlap region geometry is complicated in terms of the pycnocline structure to derive the relation analytically. As a test case, the uniform stratification and free-slip surface reflection to verify the generation mechanism analytically. However, in this case, there is no refraction so that the effect of the beam overlap can be observed seperately.

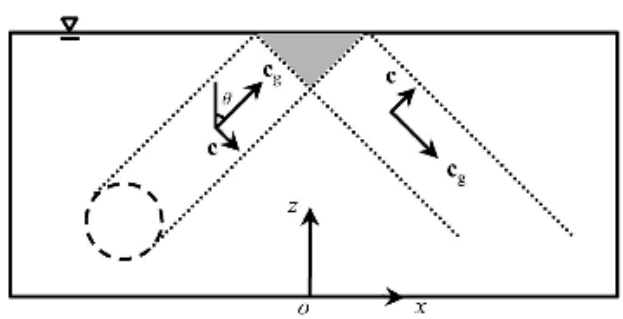

Figure 4.1: The schematic illustration of the incident and the reflecting Beam for the case of reflection off a free slip surface [7].

Note that the shaded area in figure (4.1) shows the interaction region where we observe the harmonic and the mean flow generation. Numerically, localized 45° angle wave beam can be excited using gaussian forcing region, but since we want to derive a simple analytical model let's impose our linear incident and the reflecting beam on the field and evaluate the convective terms. It prepares also a good basis for the energy flux formulation in case of pycnocline. In this particular formulation, the purpose is to take the product of the velocity with the momentum equation to obtain the energy equation for the each frequency. This operation is described in detail in the section (4.3).

Incident and Reflecting Plane Wave

Let's start with the incident beam phase $\phi_i = k_x x - k_z z - \omega t$. For the given phase, the linear velocity field could be written as follows,

$$u_i = N_0 \frac{k_z}{\sqrt{k_x^2 + k_z^2}} A_i \sin(\phi_i) \tag{4.20}$$

$$w_i = N_0 \frac{k_x}{\sqrt{k_x^2 + k_z^2}} A_i \sin(\phi_i) \tag{4.21}$$

Note that the subscript i denotes the incident wave. Let's write also the reflecting beam with $\phi_r = k_x x + k_z z - \omega t + \phi_0$. The phase of the reflecting beam has the phase change ϕ_0. For the given phase, the linear velocity field could be written as follows,

$$u_r = N_0 \frac{k_z}{\sqrt{k_x^2 + k_z^2}} A_r \sin(\phi_r) \tag{4.22}$$

$$w_r = N_0 \frac{-k_x}{\sqrt{k_x^2 + k_z^2}} A_r \sin(\phi_r) \tag{4.23}$$

In this case, the subscript r denotes the reflecting beam. Now, to obtain the total velocity field let's add them up,

$$u = u_i + u_r = N_0 \frac{k_z}{\sqrt{k_x^2 + k_z^2}} (A_i \sin(\phi_i) + A_r \sin(\phi_r)) \tag{4.24}$$

$$w = w_i + w_r = N_0 \frac{k_x}{\sqrt{k_x^2 + k_z^2}} (A_i \sin(\phi_i) - A_r \sin(\phi_r)) \tag{4.25}$$

By using the velocity field above, let's calculate the convective terms in the momentum equation:

$$u\frac{\partial u}{\partial x} + w\frac{\partial u}{\partial z}. \tag{4.26}$$

$$\frac{\partial u}{\partial x} = N_0 \frac{k_z k_x}{\sqrt{k_x^2 + k_z^2}}(A_i \cos(\phi_i) + A_r \cos(\phi_r)) \tag{4.27}$$

$$\frac{\partial u}{\partial z} = N_0 \frac{{k_z}^2}{\sqrt{k_x^2 + k_z^2}}(-A_i \cos(\phi_i) + A_r \cos(\phi_r)) \tag{4.28}$$

In total, we end up with the following equation from x-momentum equation.

$$u\frac{\partial u}{\partial x}+w\frac{\partial u}{\partial z} = {N_0}^2 \frac{{k_z}^2 k_x}{k_x^2 + k_z^2} A_i A_r((\cos(\phi_i)\sin(\phi_r)+\cos(\phi_r)\sin(\phi_i))+(\cos(\phi_i)\sin(\phi_r)-\cos(\phi_r)\sin(\phi_i))) \tag{4.29}$$

If we use the trigonometric identities it can be written as follows,

$$u\frac{\partial u}{\partial x} + w\frac{\partial u}{\partial z} = {N_0}^2 \frac{{k_z}^2 k_x}{k_x^2 + k_z^2} A_i A_r(\sin(\phi_r + \phi_i) + \sin(\phi_i - \phi_r)) \tag{4.30}$$

One of those phase sum will correspond to first harmonic forcing, the other is zeroth mode forcing, If we write it explicitly,

$$u\frac{\partial u}{\partial x} + w\frac{\partial u}{\partial z} = {N_0}^2 \frac{{k_z}^2 k_x}{k_x^2 + k_z^2} A_i A_r(\sin(2k_x x - 2\omega t + \phi_0) + \sin(-2k_z z - \phi_0)) \tag{4.31}$$

We calculate the convective forcing for x-momentum equation. Let's compute it for the z-momentum equation as well,

$$u\frac{\partial w}{\partial x} + w\frac{\partial w}{\partial z}. \tag{4.32}$$

$$\frac{\partial w}{\partial x} = N_0 \frac{{k_x}^2}{\sqrt{k_x^2 + k_z^2}}(A_i \cos(\phi_i) + A_r \cos(\phi_r)) \tag{4.33}$$

$$\frac{\partial w}{\partial z} = N_0 \frac{-k_x k_z}{\sqrt{k_x^2 + k_z^2}} (A_i \cos(\phi_i) + A_r \cos(\phi_r)) \tag{4.34}$$

After rearranging the terms,

$$u\frac{\partial w}{\partial x} + w\frac{\partial w}{\partial z} = {N_0}^2 \frac{{k_x}^2 k_z}{k_x^2 + k_z^2} A_i A_r (\sin(2k_x x - 2\omega t + \phi_0) - \sin(-2k_z z - \phi_0)) \tag{4.35}$$

Under that type of forcing field, we should observe a sine type of mean flow structure with a half wave length of the incident wave beam in z-direction. The simulation results also produce similar spatial structure in vertical direction. The results prepare basis for the pycnocline case. This formulation allows to derive energy equation for the zeroth mode and harmonics seperately. The momentum equations are multiplied by the mean flow and first harmonic velocity to derive the energy equation for them seperately.

4.3 The Analytical Model for The Harmonics Generation inside the Pycnocline

Differing from the uniform stratification, at the presence of the pycnocline, the harmonics may get trapped into pycnocline. The angle of propagation determines if harmonics get trapped inside the pycnocline. For instance, the first harmonic has the frequency $2\omega_0$, if it exceeds the lower layer BV frequency $N(0)$ which increases negligibly till it reaches the pycnocline, there exists another critical level of reflection at which$2\omega_0$ matches the BV frequency $N(z_l)$. Note z_l denotes the lower critical level of reflection but there also exists a seperate upper critical level z_u of reflection for the first harmonic at which $2\omega_0$ matches the BV frequency $N(z_u)$. The exact locations could be calculated for the model pycnocline

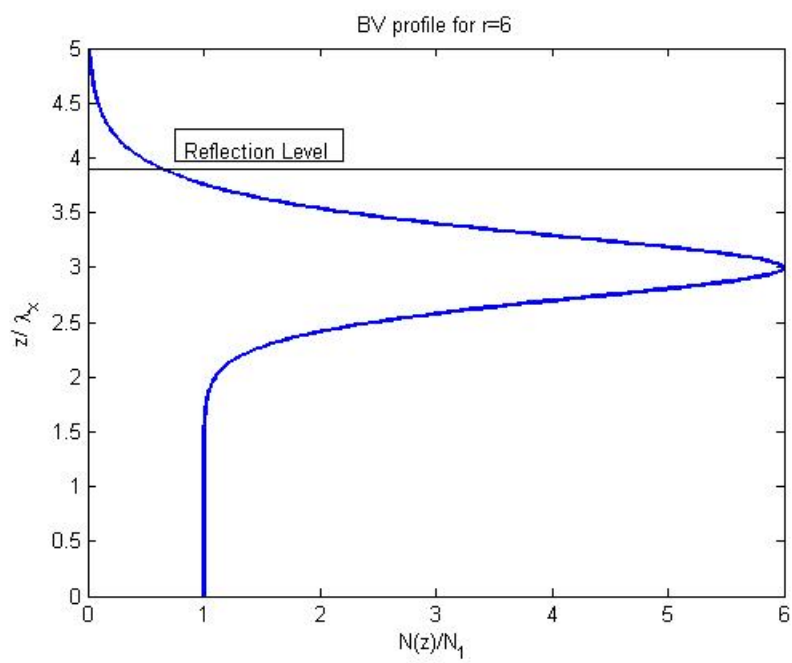

Figure 4.2: BV frequency profile for $r = 6$ and $h/\lambda_x = 0.1$ and the reflection Level at which $N(z_r) = \omega$.

In the presence of a pycnocline, instead of free-slip surface which causes the reflection of the primary frequency wave, there is a critical level of reflection for the primary frequency wave. At that level, the primary frequency ω matches the BV frequency. It also cases the wave reflection. While setting up the analytical model for this scenario, the primary frequency wave could be decomposed of the incident wave and the reflecting wave. The incident and the reflecting wave will differ by the wavenumber vector directions, therefore the group velocity vector directions. Let's write down the incident wave beam,

$$u^i = A_u^i(X, Z, T)\cos(\phi_i). \tag{4.36}$$

$$w^i = A_w^i(X, Z, T)\cos(\phi_i). \tag{4.37}$$

Note that $\phi_i = k_x x - \int_0^z k_z(z')dz' - \omega t$ and the slow variables $X_i = \epsilon(x - \int_0^t Cg_x dt')$, $Z_i = \epsilon(z - \int_0^t Cg_z dt')$, $T = \epsilon^2 t$. The effect of the variable stratification is felt via the variable group velocities and $k_z(z)$. It directly affects the phase and the slow variables. The slow variables are used to describe the evolution of the wave amplitude and $\epsilon = \sigma k_\eta << 1$. It also assumes that the wave amplitude is centered around a particular wavenumber vector $\vec{k}$ in Fourier space. By using this argument, the slow variables could be derived using Schrdinger's equation [1]. Additionally, the amplitudes $A_u^i(X, Z, T)$ and A_w^icould be related to each other using the continuity,

$$\frac{\partial u^i}{\partial x} + \frac{\partial w^i}{\partial z} = 0. \tag{4.38}$$

The continuity condition leads to the following expression,

$$k_x A_u^i(X_i, Z_i, T)\sin(\phi_i) - k_z A_w^i(X_i, Z_i, T)\sin(\phi_i) + \epsilon\cos(\phi_i)\left(\frac{\partial A_u^i(X_i, Z_i, T)}{\partial X} + \frac{\partial A_w^i(X_i, Z_i, T)}{\partial Z}\right) = 0. \tag{4.39}$$

As $\epsilon << 1$, at the leading order, it reduces to the following equivalence,

$$\frac{k_z}{k_x} A_w^i(X_i, Z_i, T) \approx A_u^i(X_i, Z_i, T). \tag{4.40}$$

Let's also write down the reflecting wave beam and plug it into continuity equation,

$$u^r = A_u^r(X_r, Z_r, T)\cos(\phi_r). \tag{4.41}$$

$$w^r = A_w^r(X_r, Z_r, T)\cos(\phi_r). \tag{4.42}$$

Note that $\phi_r = k_x x + \int_0^z k_z(z')dz' - \omega t + \phi_0$,where ϕ_0 is the phase diffence, and the slow variables $X_r = \epsilon(x - \int_0^t Cg_x dt')$, $Z_r = \epsilon(z + \int_0^t Cg_z dt')$, $T = \epsilon^2 t$. After the same manipulation, at the leading order, the wave amplitudes could be related as follows,

$$\frac{k_z}{k_x} A_w^r(X_r, Z_r, T) \approx -A_u^r(X_r, Z_r, T). \tag{4.43}$$

It may be substituted into the momentum equations directly. However to proceed more compactly and depending on the problem, let's denote the first harmonic directly as the sum of upward and downward propagating wave as follows,

$$u_{2\omega_0} = A_u^{2\omega_0}(X^{2\omega_0}, Z^{2\omega_0}, T) f_1(x, z)\cos(2\omega t). \tag{4.44}$$

$$w_{2\omega_0} = A_w^{2\omega_0}(X^{2\omega_0}, Z^{2\omega_0}, T) g_1(x, z)\cos(2\omega t). \tag{4.45}$$

Here the slow variables are defined with the different indices $X^{2\omega_0}$ and $Z^{2\omega_0}$ denotes the slow variables for the wave amplitude. In terms of the fast vari-

ables, spatial structure is defined seperately from the time as the resultant energy equation will be time-averaged. $f_1(x,z)$ and $g_1(x,z)$ are spatially oscillatory part of the first harmonic wave.

The zeroth mode signal does not show the characteristics of the propagating wave so It does not have spatiotemporally structure, it could be denoted as follows,

$$u_0 = A_u^0(T) f_2(x,z). \tag{4.46}$$

$$w_0 = A_w^0(T) g_2(x,z). \tag{4.47}$$

After defining the primary frequency wave, first harmonic wave and the mean flow, let's write down the momentum equations in terms of the pressure gradient, the convective term and the diffusive term. The purpose of the following analysis is to understand the nonlinear generation mechanism caused by the incident and the reflecting primary internal wavebeam overlap. Having said these, it is based on the assumption that the energy of the primary frequency wave is much higher than the harmonics and the mean flow, therefore while calculating the diffusive and convective terms, the effect of the mean flow and the harmonics are neglected. The momentum equation is expressed in terms of the convective and diffusive operators:

$$\frac{\partial \mathbf{u}}{\partial t} + N(\mathbf{u}) = -\frac{1}{\rho_0}\nabla p + D(\mathbf{u}) + \mathbf{F}_g. \tag{4.48}$$

where $N(\mathbf{u})$ is the convective operator, $D(\mathbf{u})$ is the diffusive operator. Let's calculate first the nonlinear operator $N(\mathbf{u})$ in x momentum equation for the conditions given above,

$$u\frac{\partial u}{\partial x} = (u_i + u_r)\frac{\partial(u_i + u_r)}{\partial x} = k_x(A_u^i(X, Z, T)\cos(\phi_i) + A_u^r(X_r, Z_r, T)\cos(\phi_r))(A_u^i(X, Z, T)\sin(\phi_i) + A_u^r(X_r, Z_r, T)\sin(\phi_r)). \tag{4.49}$$

Note that the variation in the amplitude is much smaller than the oscillatory part as it is modelled with slow variables so that the effect is negligible as $dA_i/dx = \epsilon dA_i/dX_i << 1$.

$$w\frac{\partial u}{\partial z} = (w_i + w_r)\frac{\partial(u_i + u_r)}{\partial z} = k_z(\frac{k_x}{k_z}A_u^i(X, Z, T)\cos(\phi_i) - \frac{k_x}{k_z}A_u^r(X_r, Z_r, T)\cos(\phi_r))(-A_u^i(X, Z, T)\sin(\phi_i) + A_u^r(X_r, Z_r, T)\sin(\phi_r)). \tag{4.50}$$

Based on this computation, in total it could be written as follows,

$$u\frac{\partial u}{\partial x} + w\frac{\partial u}{\partial z} = k_x A_u^i A_u^r(\sin(\phi_i + \phi_r) + \sin(\phi_i - \phi_r)) = k_x A_u^i A_u^r(\sin(2k_x x - 2\omega t + \phi_0) + \sin(-2\int_0^z k_z(z')dz' - \phi_0). \tag{4.51}$$

The same derivation is also done for the convective operator in z momentum equation,

$$u\frac{\partial w}{\partial x} + w\frac{\partial w}{\partial z} = k_z A_u^i A_u^r(\sin(\phi_i + \phi_r) - \sin(\phi_i - \phi_r)) = k_z A_u^i A_u^r(\sin(2k_x x - 2\omega t + \phi_0) - \sin(-2\int_0^z k_z(z')dz' - \phi_0)). \tag{4.52}$$

After calculating the convective operator $N(\mathbf{u})$, let's calculate the diffusive operator $D(\mathbf{u})$,

$$\frac{\partial^2 u}{\partial x^2} + \frac{\partial^2 u}{\partial z^2} = (k_x^2 + k_z^2)(A_u^i\cos(\phi_i) + A_u^r\cos(\phi_r)). \tag{4.53}$$

and also,

$$\frac{\partial^2 w}{\partial x^2} + \frac{\partial^2 w}{\partial z^2} = (k_x^2 + k_z^2)\frac{k_x}{k_z}(A_u^i\cos(\phi_i) - A_u^r\cos(\phi_r)). \tag{4.54}$$

After calculating the convective and the diffusive terms, let's derive seperate energy equations for the first harmonic by taking the product of the first harmonic velocity vector and the momentum equation. Each frequency can be differentiated by using the orthogonality relation. The first harmonic velocity vector is orthogonal to the terms that do not contribute to the generation of it, therefore the evolution equation equation can be obtained for the first harmonic seperately. To calculate the energy evolution of the first harmonic signal, let's multiply the momentum equation with the first harmonic velocity $\mathbf{u}^{2\omega_0}$ and time average over one primary frequency period T,

$$\mathbf{u}^{2\omega_0}(\frac{\partial \mathbf{u}}{\partial t} + N(\mathbf{u}) = -\frac{1}{\rho_0}\nabla p + D(\mathbf{u}) + \mathbf{F}_g). \tag{4.55}$$

Note that $\mathbf{u}^{2\omega_0}$ is ortogonal to the every term at the right handside of the equation over one primary frequency period T as they are induced linearly by the presence of the primary frequency signal. However, the time derivative and the convective term is not. Let's write the product of the first harmonic and the time derivative explicitly:

$$\begin{aligned} A_u^{2\omega_0}(X^{2\omega_0}, Z^{2\omega_0}, T) f_1(x,z)\cos(2\omega t)(&\frac{\partial A_u^{2\omega_0}(X^{2\omega_0}, Z^{2\omega_0}, T) f_1(x,z)}{\partial t}\cos(2\omega t) \\ &-2\omega A_u^{2\omega_0}(X^{2\omega_0}, Z^{2\omega_0}, T) f_1(x,z)\sin(2\omega t)) \\ +A_w^{2\omega_0}(X^{2\omega_0}, Z^{2\omega_0}, T) g_1(x,z)\cos(2\omega t)(&\frac{\partial A_w^{2\omega_0}(X^{2\omega_0}, Z^{2\omega_0}, T) g_1(x,z)}{\partial t}\cos(2\omega t) \\ &-2\omega A_w^{2\omega_0}(X^{2\omega_0}, Z^{2\omega_0}, T) g_1(x,z)\sin(2\omega t)). \end{aligned} \tag{4.56}$$

Note that the primary frequency and the mean flow is not included as it will vanish after the time averaging. After time averaging, it reduces to the following:

$$\frac{1}{4}\frac{\partial((A_w^{2\omega_0}g_1(x,z))^2 + (A_u^{2\omega_0}f_1(x,z))^2)}{\partial t} \tag{4.57}$$

Note that again the variation in amplitude is much smaller than in the oscillatory part so the amplitude can be assumed constant over one wave period. Let's perform the time averaging on the product of the first harmonic velocity and the convective operator,

$$\begin{aligned}\mathbf{u}^{2\omega_0}N(\mathbf{u}) = A_u^{2\omega_0}k_xA_u^iA_u^r\sin(2k_xx - 2\omega t + \phi_0)\sin(2k_xx + \phi_0)\cos(2\omega t)+ \\ A_w^{2\omega_0}k_zA_u^iA_u^r(\sin(2k_xx - 2\omega t + \phi_0))g_1(x,z)\cos(2\omega t).\end{aligned} \tag{4.58}$$

This form of the product of the convective operator and the first harmonic signal indicates that depending on the phase difference and the position in x direction, the rate of the first harmonic energy generation changes. To show it more clearly, let's decompose $\sin(2k_xx - 2\omega t + \phi_0)$,

$$\sin(2k_xx - 2\omega t + \phi_0) = \sin(2k_xx + \phi_0)\cos(2\omega t) - \cos(2k_xx + \phi_0)\sin(2\omega t). \tag{4.59}$$

Let's time average it over one primary frequency period T by using the identities given above:

$$2 < \mathbf{u}^{2\omega_0}N(\mathbf{u}) >= k_xA_u^{2\omega_0}A_u^iA_u^r\sin(2k_xx + \phi_0)f_1(x,z) + k_zA_w^{2\omega_0}A_u^iA_u^r\sin(2k_xx + \phi_0)g_1(x,z). \tag{4.60}$$

Let's combine the equation (4.57) and (4.60) to form the initial evolution of the first harmonic signal:

$$\begin{aligned}\frac{1}{2}\frac{\partial((A_w^{2\omega_0}g_1(x,z))^2 + (A_u^{2\omega_0}f_1(x,z))^2)}{\partial t} = -k_xA_u^{2\omega_0}A_u^iA_u^r\sin(2k_xx + \phi_0)f_1(x,z) \\ -k_zA_w^{2\omega_0}A_u^iA_u^r\sin(2k_xx + \phi_0)g_1(x,z).\end{aligned} \tag{4.61}$$

This equation can be simplified even further and solved but let's focus on what it suggests in terms of physics. First, the left-hand side clearly shows that the excitation of harmonic is dependent on the phase difference of the overlaping part of the incident and the reflecting primary frequency of the internal wave beam. Moreover, the excitation of the first harmonic signal is dependent on the product of the amplitude of the incident internal wave beam A_u^i and the reflecting internal wave beam A_u^r. The effect of variable stratification is implied by the slow variables and $k_z(z)$. These amplitudes are also correlated with the kinetic energy of the internal wave beam therefore if the incident wave energy and the reflecting wave energy accumulates on a particular region it will enhance the first harmonic generation. In our case, the overlap region inside the pycnocline corresponds to that.

The same derivation can be done to capture the mean flow content. Let's multiply the momentum equation with the mean velocities $\mathbf{u}_0$,

$$\mathbf{u}^0(\frac{\partial \mathbf{u}}{\partial t} + N(\mathbf{u}) = -\frac{1}{\rho_0}\nabla p + D(\mathbf{u}) + \mathbf{F}_g). \tag{4.62}$$

Again, when it is time averaged, every term on the right-hand side will vanish as they are linearly induced by the presence of the primary frequency wave and it is functionally orthogonal to the mean velocities. Taking that into account, the time averaging operation will reduce it to the following equation:

$$\begin{aligned}\frac{1}{2}\frac{\partial((A_u^0 f_2(x,z))^2 + (A_w^0 g_2(x,z))^2)}{\partial t} &= -k_x A_u^0 A_u^i A_u^r \sin(-2\int_0^z k_z(z')dz' - \phi_0) f_2(x,z) \\ &+ k_z A_w^0 A_u^i A_u^r \sin(-2\int_0^z k_z(z')dz' - \phi_0) g_2(x,z).\end{aligned} \tag{4.63}$$

This equation can be solved after further simplifications, however it also gives an insight about the spatial excitation of the mean flow structure. Finally it suggests that the excitation of the mean flow is dependent on the product of the amplitude of the incident internal wave beam A_u^i and the reflecting internal wave beam A_u^r.

CHAPTER 5

RESULTS

After understanding the underlying physics and developing the numerical analysis tools, those tools are applied to the thin pycnocline cases where $h/\lambda_x = 0.1$ for $r = 2, 4, 6, 8, 10$. Note that $r = N_{max}/N_1$ and h is the pycnocline thickness. The highest energy transfer to the first harmonic is observed at $r = 6$ case and the highest energy transfer to the mean flow is observed at $r = 4$ case for $Re = 530$. To reduce the effect of the viscous loss, the Reynolds number is increased to 5300. The thin pycnocline case is chosen intentionally as it shows the highest energy transfer to the harmonics experimentally [9],[3]. In the case of reduced viscosity, the effect of the wave steepening slightly observed as the Reynolds number $U_{max}\lambda_x/\nu = 530$ is increased to 5300. However, it did not cause the wavebreaking for $r = 2, 4, 6$ cases. Nonetheless, the order of the spectral filter is decreased to provide the stability, as the solution has blown up for $r = 8, 10$ in the reduced viscosity without changing the order of the spectral filter. But the change in viscosity did not affect the ray paths and the analysis tools developed previously as it comes from the linear theory mentioned previously.

5.1 Energy Evolution along IWB Path

The internal wave beam is excited at the lower layer by a virtual forcing pedal which has Gaussian profile centered around a particular location. That type forcing region also leads to a Gaussian profile for the velocity at that cross-section. This allows us to capture the most of the energy flux within six wavelengths.

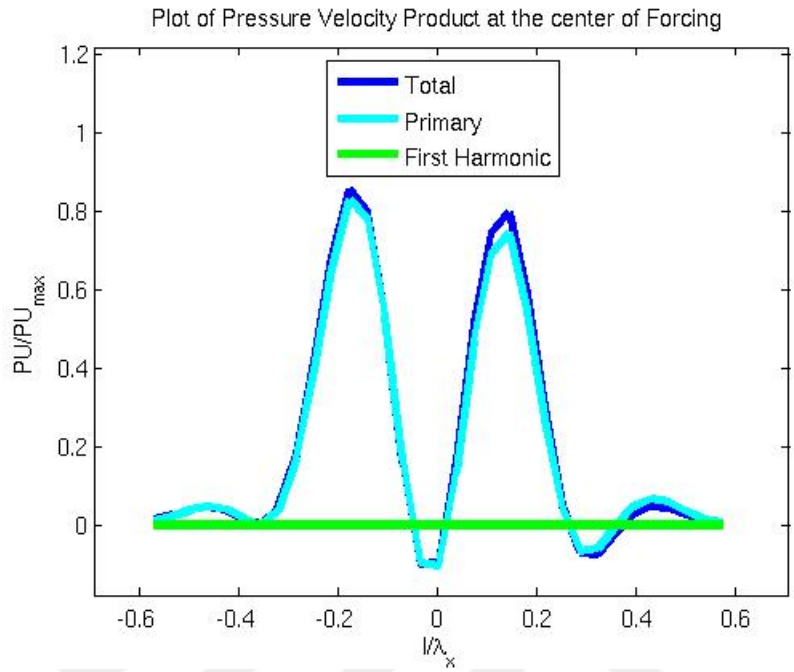

Figure 5.1: Energy flux profile on the center of the Gaussian forcing region for $r = 6$ and $h/\lambda_x = 0.1$, $Re = 530$

The internal wave beam reaches its peak energy flux not at the center of the forcing region, but $0.7\lambda_x$ distance after that center of forcing along the group velocity vector direction. Besides, as expected, the effect of nonlinearity is negligible up to a point where the effect of pycnocline started being felt.

As shown in the figure (5.2), the total energy flux decays 10% due to viscous dissipation till it reaches the entry of the triangular region. The same profile is observed for $r = 2, 4, 8, 10$ along IWB. Note that $s = 0$ is the center of the forcing region shown in the figure (3.1) and it increases along IWB path. In the case of the reduced viscosity, the viscous dissipation along IWB is reduced to 2% of the total energy flux. However, as seen in the figure (5.5b), the effect of high Reynolds number shows itself as a small disturbance in the energy flux for the reduced viscosity case. It is still not very effective for $r = 2, 4, 6$, as mentioned earlier, it leads to unstable solution for $r = 8, 10$ case. This problem is solved by

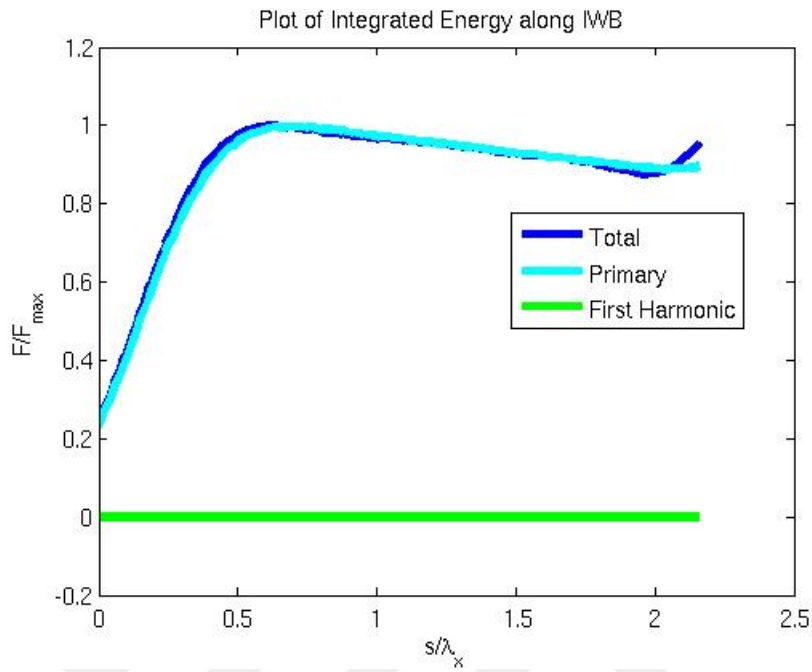

Figure 5.2: Energy flux along the internal wave beam path (IWB) for $r = 6$ and $h/\lambda_x = 0.1$, $Re = 530$

adjusting the spectral filter.

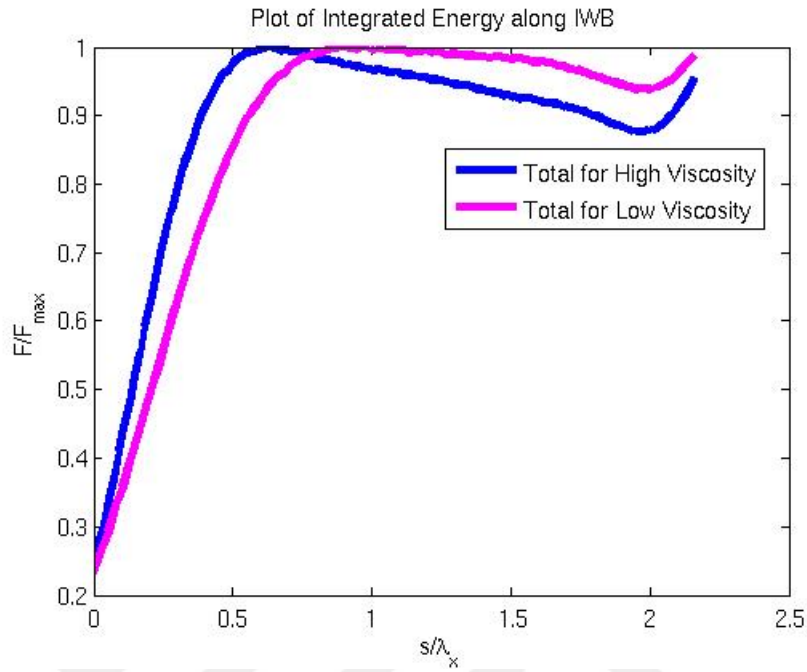

Figure 5.3: Total energy flux along the internal wave beam path (IWB) for $r = 6$ and $h/\lambda_x = 0.1$, $Re = 530$ vs $Re = 5300$

5.2 Energy Balance inside The Triangular Region

The energy influx into the triangular region is provided by the flux from the IWB path. The total influx is approximately 90% of the peak energy flux for high viscosity cases. It is approximately 98% of the peak energy flux for the reduced viscosity. However, the effect of nonlinearity changes for different pycnocline strengths. It also affects the viscous loss, therefore the amount of the reflecting energy. To verify the energy balance, the energy budget table is prepared. In the energy budget table, the ratio of how much energy flux transferred or dissipated at each case is given.

Let's define the corresponding coefficients. $TRI = F_{tri}/F_{max}$ which is the ratio of the energy flux transmited to triangular zone to the maximum energy flux

along IWB. The transmission coefficient $TR = F_{tr}/F_{max}$ which is the ratio of the energy flux transmited to pycnocline to the maximum energy flux along IWB. The viscous loss coefficient $VIS = F_{vis}/F_{max}$ which is the ratio of the energy loss due to viscous dissipation along triangular zone to the maximum energy flux along IWB. The reflection coefficient $REF = F_{ref}/F_{max}$ which is the ratio of the energy flux reflected back to the lower layer at first reflection to the maximum energy flux along IWB which occurs around $s = 0.5\lambda_x$ as shown figure (5.2). The reflection coefficient $RAD = F_{rad}/F_{max}$ which is the ratio of the energy flux re-radiated back to the lower layer along pycnocline to the maximum energy flux along IWB.

r	2	4	6	8	10
TRI	0.91	0.881	0.877	0.9	0.856
TR	0.0116	0.3	0.288	0.134	0.13
VIS	0.162	0.346	0.388	0.55	0.479
REF	0.747	0.235	0.201	0.214	0.244
RAD	0.0094	0.189	0.2	0.00759	0.01

Table 5.1: The energy budget table for $Re = 530$

Note that $TRI = TR + VIS + REF$ as the energy is conserved. As the results suggest the maximum energy transfer into pycnocline occurs at $r = 4$ for $Re = 530$ case. However, this does not give a clear idea about the content of the energy reaching the pycnocline in terms of frequency distribution. The viscous loss is more dominant for the stronger pycnocline cases. In the reduced viscosity simulations, its effect diminished though it is not halted. It affects the amount of the energy transferred to the pycnocline considerably. Additionally, The first harmonic generation is noticeable inside the triangular zone.

As figure (5.4) shows the first harmonic generation becomes noticeable towards the end of the triangular zone though it reaches its peak in the entry

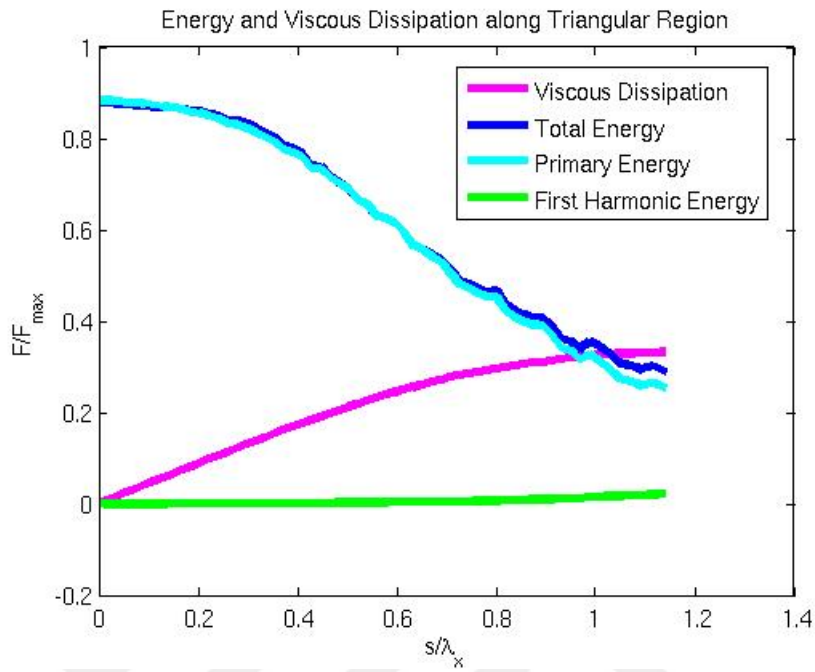

Figure 5.4: Energy flux evolution inside the triangular region $r = 6$ and $h/\lambda_x = 0.1$, $Re = 530$

region of the downstream pycnocline. As for the reduced viscosity case, the table is given (Table 5.2).

r	2	4	6	8	10
TRI	0.97	0.98	0.95	0.792	0.856
TR	0.012	0.394	0.33	0.11	0.14
VIS	0.094	0.21	0.34	0.123	0.15
REF	0.856	0.247	0.248	0.169	0.25
RAD	0.007	0.296	0.11	0.00534	0.018

Table 5.2: The energy budget table for $Re = 5300$

The viscous dissipation is reduced for $r = 2, 4, 6$ as expected for $Re = 5300$ even though its effect is still considerable as the pycnocline strength increases. However, $r = 8$ and $r = 10$ cases do not confirm the energy conservation. As mentioned before, the simulations for $r = 8$ and $r = 10$ has blown up for the same filter order used for $r = 2, 4, 6$ in the reduced viscosity simulations. They

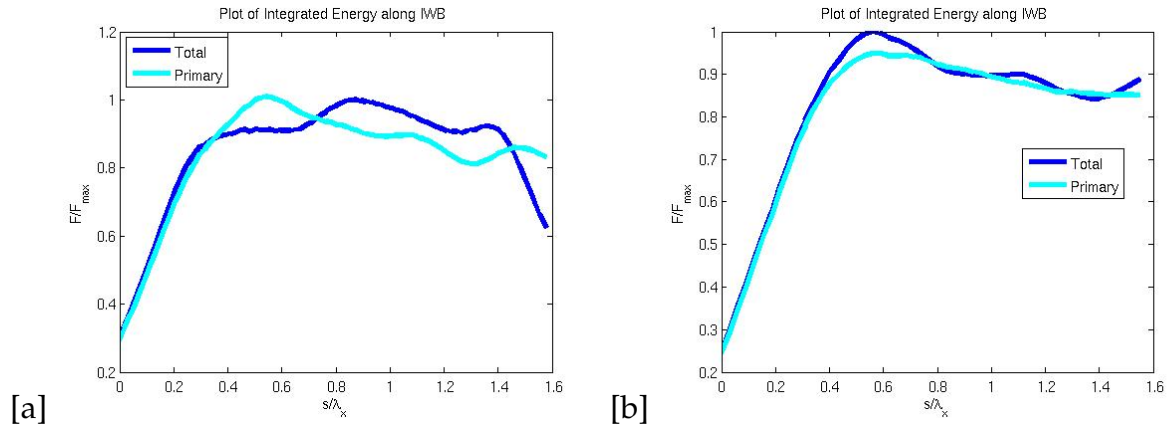

Figure 5.5: Energy flux evolution along IWB for $Re = 5300$ a) $r = 2$, $h/\lambda_x = 0.1$ b) $r = 4$, $h/\lambda_x = 0.1$

converged to a stable solution when the order of the filter is reduced. The effect of the unstable growth could be observed along IWB as well for those cases.

The spectral filtering causes energy loss within the triangular region due to the unstable growth. This is the reason why $TRI \neq TR + VIS + REF$ for those cases. It means spectral filter acts on the scale of hte wavelengths λ_x and λ_z. The unstability is induced by higher Reynolds number for the reduced viscosity simulations. It is more amplified for $r = 8$ and $r = 10$ cases. A significant part of energy is lost in the spectral filtering operation.

5.3 Numerical and Analytical Viscous Decay Models

The simplified analytical model is developed both to verify the numerically calculated viscous dissipation approximately and to observe the effect of the varying pycnocline strength. Based on the equation (4.19), the internal wave amplitude decays roughly exponentially $\exp(-c \int N^2 d\xi)$ with increasing pycnocline strength. Although the results coming from the analytical model is calculated using numerical integration to consider the effect of the change in group velocity and the wave amplitude variation along the group velocity direction. The numerical integration of the analytical model starts at the point where the energy flux reaches its peak which is around $0.5\lambda_x$ far from the center of the forcing region. To make an appropriate comparison of the analytical model and the numerical calculation done by using the simulation data, they started being compared when the energy flux reduces to level of the energy flux into the triangular region as there is no specified triangular region for the analytical model (see Figure A.1).

Note that the vertical line in figure (5.6) show the location where the triangular region starts. However, the analytical model can not capture the effect of the reflection. In the cases where the reflecting energy is stronger, the analytical model shows more deviation from the actual viscous dissipation. In $r = 2$ case, the reflecting energy is stronger so that the analytical model diverges from the numerically calculated viscous dissipation.

The main motivation to develop analytical model is to have an approximate numerical result for the viscous dissipation and have an idea about how the strength of the pycnocline affects the viscous dissipation. These results are not

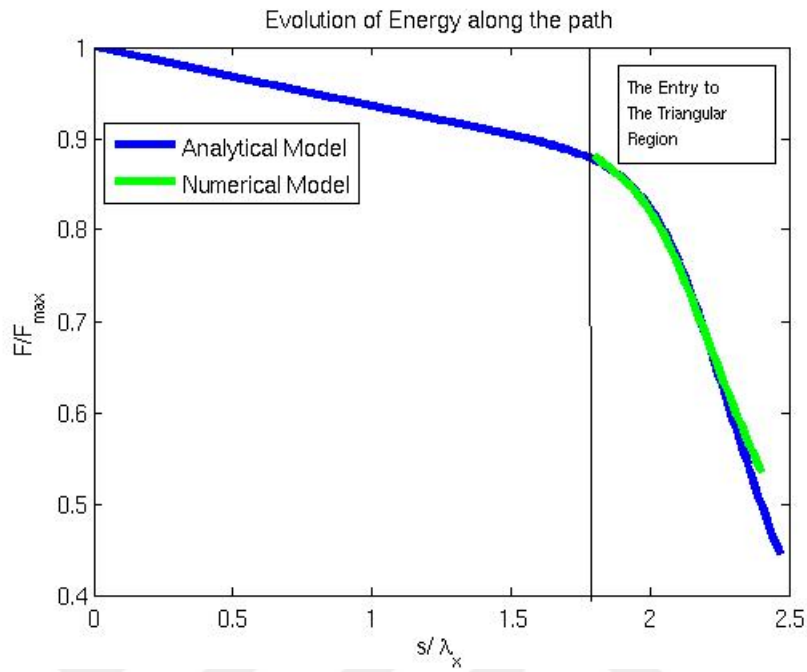

Figure 5.6: Analytical and numerical viscous dissipation for $r = 4$ and $h/\lambda_x = 0.1$, $Re = 530$

used to do the energy budget analysis (See Appendix A.1).

5.4 First Reflection

The first reflection occurs when the incident internal wave beam reaches the reflection level where $\omega = N(z_r)$. The reflecting part of the internal wave beam triggers the nonlinear interactions. It deposits some part of its energy due to nonlinear interations. The group velocity vector for the reflecting primary frequency wave beam changes its sign in z direction and it stays same in x direction. The magnitude of the group velocity vector for the reflecting internal wave beam is independent of the reflecting internal wave energy as it is derived from the dispersion relation which is a function of the wave frequency ω,

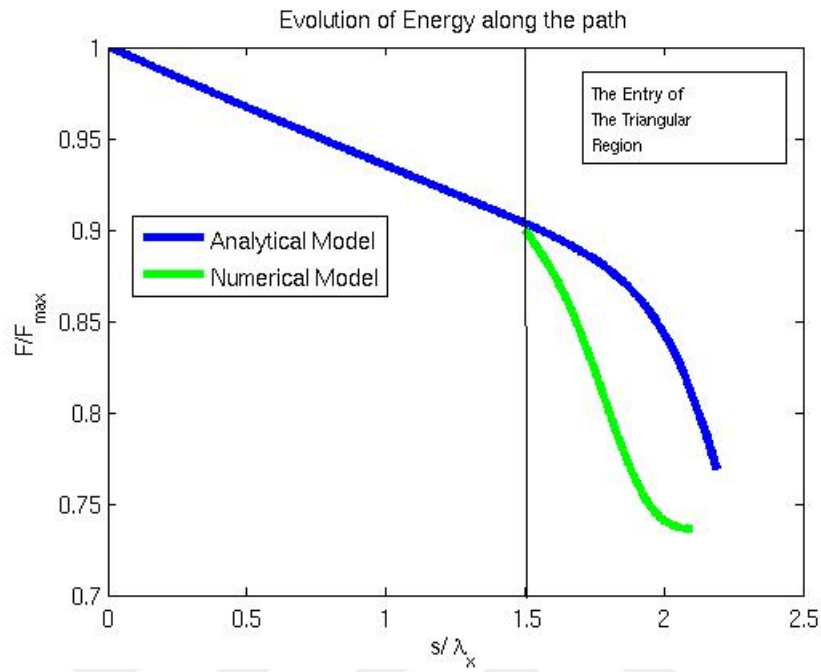

Figure 5.7: Analytical and numerical viscous dissipation for $r = 2$ and $h/\lambda_x = 0.1$, $Re = 530$

the wavenumber vector $\vec{k}$ and the background BV frequency $N(z)$. However the dependence on the background BV frequency results in the accumulation of the reflecting internal wave beam energy in some regions where the group velocity decelerates.

The accumulation of the internal wave energy occurs in the incident internal wave beam. That accumulation is particularly stronger in the overlap region of the incident and the reflecting internal wave beam. As it is shown earlier, the generation of the harmonics and the mean flow is dependent on the product of the incident internal wave beam amplitude A_i and the reflecting internal wave beam amplitude A_r. As the figure (5.8) shows, the reduction in the magnitude of the group velocity in z direction increases as the pycnoline gets stronger. The reduction in the group velocity leads to an accumulation in the pycnocline region which amplifies the nonlinear interactions. In that nonlinear interaction,

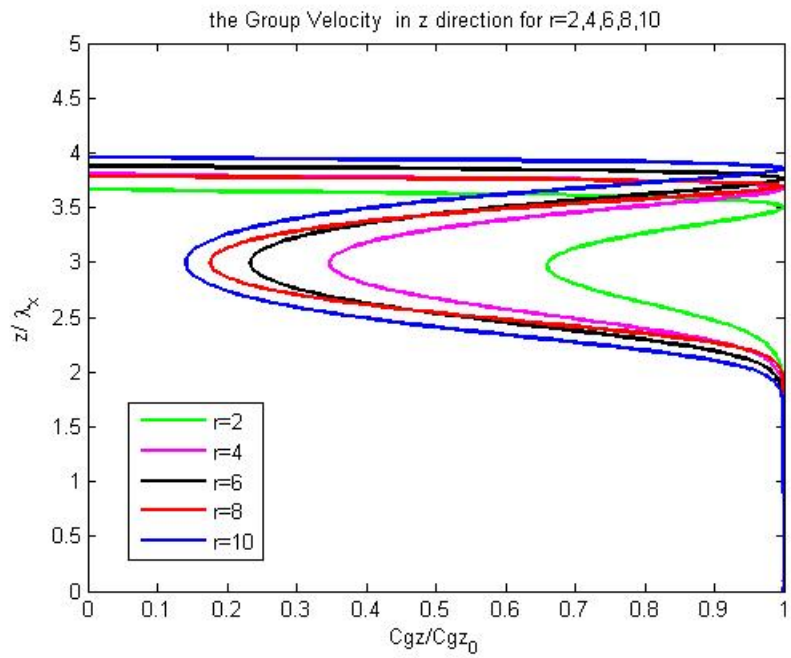

Figure 5.8: The group velocity profile in z direction for $r = 2, 4, 6, 8, 10$.

the first harmonic and the mean flow are generated. Both the incident and the reflecting internal wave beam transfer some part of its energy into the harmonics and the mean flow.

Note that in figure (5.9), $s = 0$ starts at the reflecting edge of the triangular region shown in the figure (3.3) and it increases along the reflecting group velocity vector propagating downwards. However, some part of the reflecting wave leaves the triangular region. The part of energy flux reflected back into the lower layer after the first refletion decays viscously as it propagates downwards.

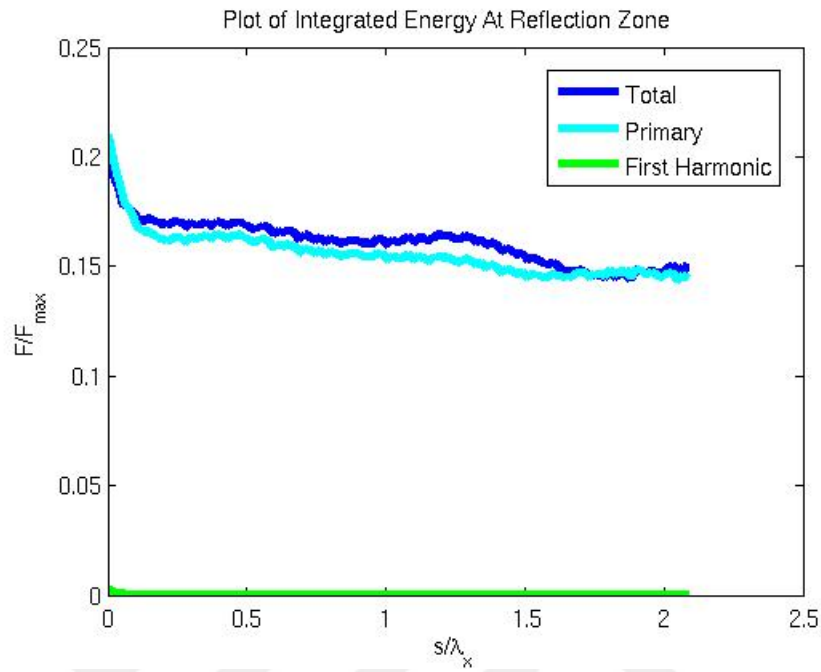

Figure 5.9: The evolution of the reflecting energy in lower Layer for $r = 6$ and $h/\lambda_x = 0.1, Re = 530$.

5.5 Energy Flux Evolution inside The Pycnocline

After the incident internal wave beam reaches the pycnocline, it interacts with the reflecting internal wave beam. This nonlinear interaction generates the first harmonic and the mean flow. The ray path of the first harmonic and the primary frequency wave is harder to track. For that reason, the energy flux evolution is observed using vertical cross-sections. Besides, as shown in the figure (5.8) the group velocity in z direction Cg_z decelarates in the pycnocline. It leads to the incident and reflecting wave energy accumulation inside the pycnocline.

As the equations (4.61) and (4.63) show, the nonlinear interactions are dependent on the product of the incident and the reflecting internal wave beam amplitude. As the strength of the pycnocline increases, the group velocity in z

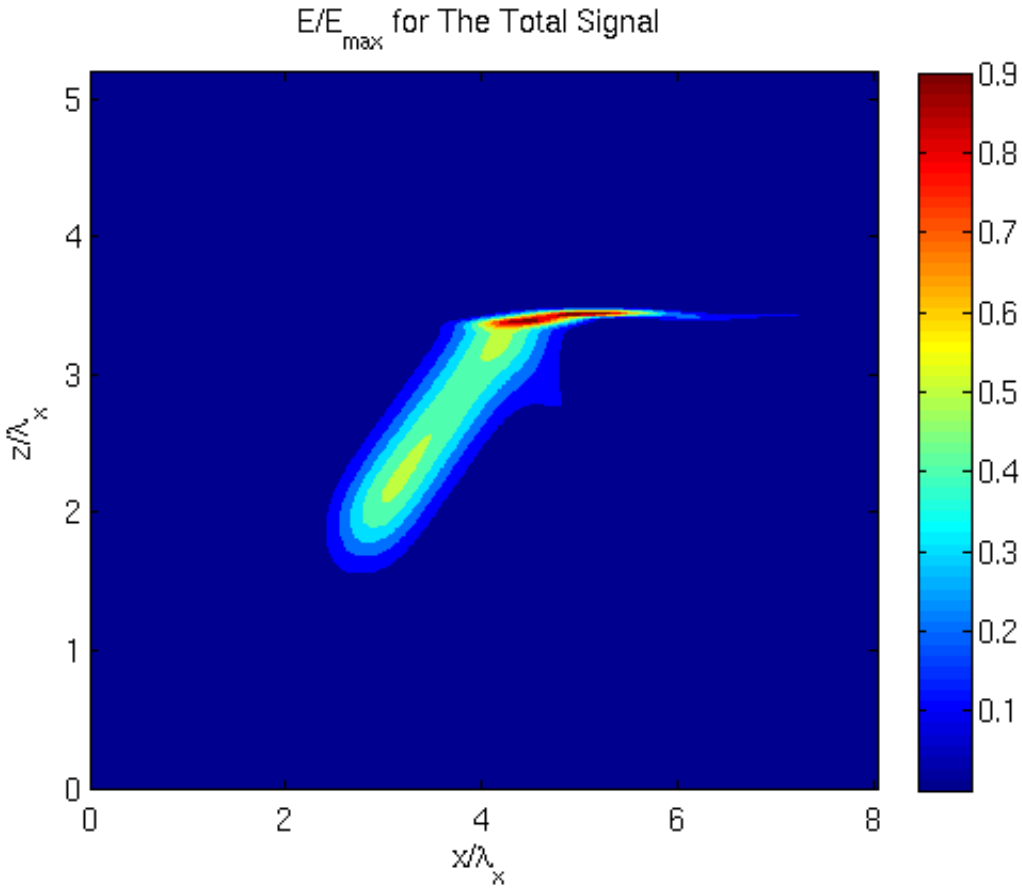

Figure 5.10: The energy distridution of the primary frequency wave for $r = 6$ and $h/\lambda_x = 0.1$ and $Re = 530$.

direction decreases as shown in the figure (5.10) so that it leads to even higher the wave energy accumulation. However, at the same time, the wavenumber increases and it leads to higher viscous dissipation. The optimal conditions for the nonlinear interaction between the incident and the reflecting internal wave beam occurs around $r = 6$ for $h/\lambda_x = 0.1$ and $Re = 530$. Even under optimal conditions, the energy flux transferred to the first harmonic is 4% of the maximum energy flux along IWB. Just after it reaches its peak, it decays over one horizontal wavelenght λ_x. The majority of the first harmonic signal dissipation occurs due to the viscous dissipation. However, the first harmonic signal also

nonlinearly interacts with the primary frequency wave and it also causes energy transfer both back into the primary frequency and the second harmonic [5]. The same generation mechanism applies for the higher order harmonics, even though it may become evanescent depending on the strength of the pycnocline due to $N < n\omega$ restriction. Besides, the effect of the viscous dissipation inside pycnocline will be even stronger on higher order harmonics as they have higher wavenumbers. Numerically calculated higher order harmonics are also negligible. The optimal configuration for the mean flow generation occurs at $r = 8$ for $h/\lambda_x = 0.1$ and $Re = 530$. The maximum mean flow energy is around 3% of the maximum energy flux along IWB. Even though the mean flow signal is not strong it survives further inside pycnocline as it is not affected by the strength of the pycnocline as the internal wave signals are affected which is explained in detail in the next paragraph.

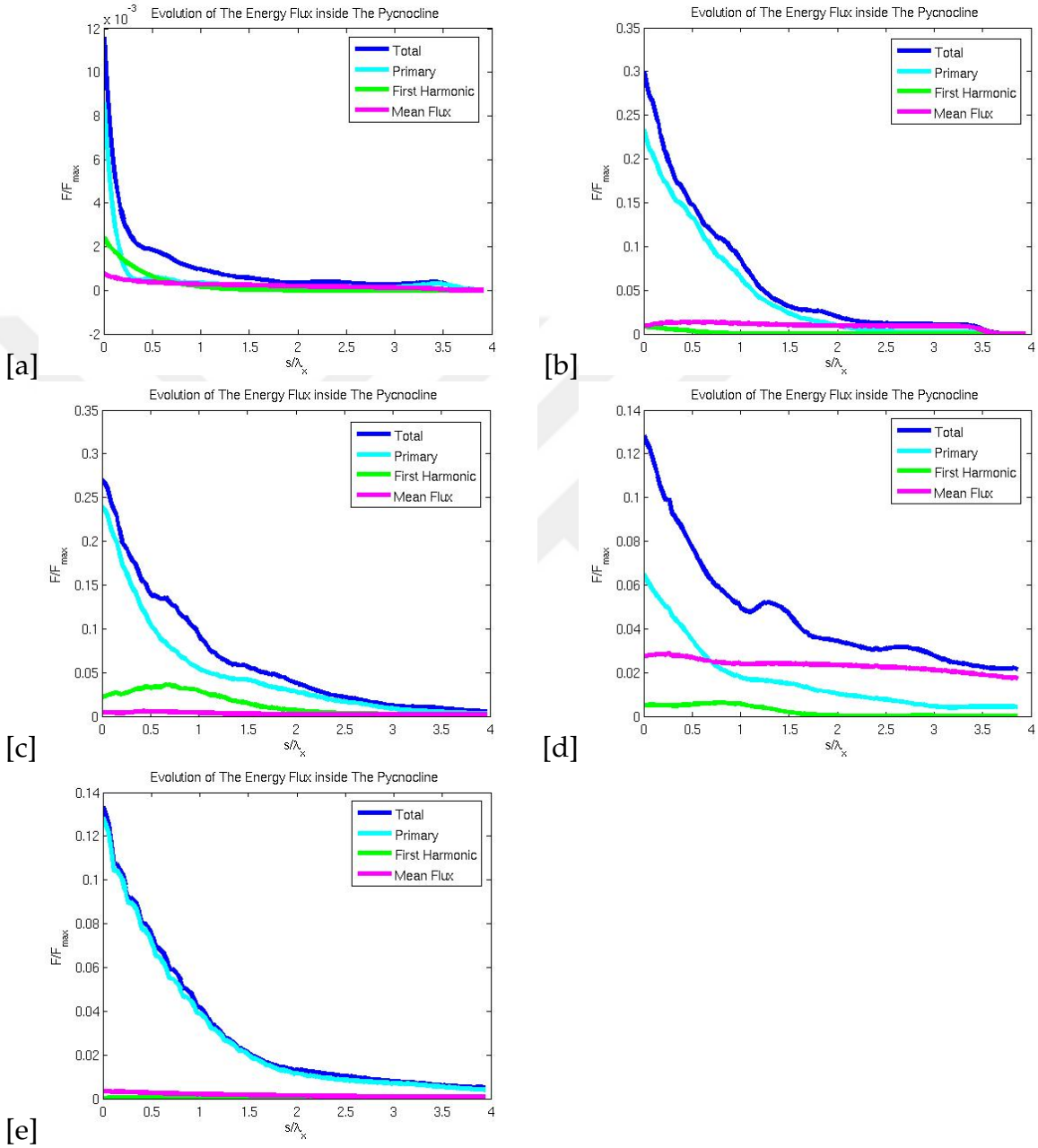

Figure 5.11: Energy flux evolution inside pycnocline for $Re = 530$ a) $r = 2$, $h/\lambda_x = 0.1$ b) $r = 4$, $h/\lambda_x = 0.1$ c) $r = 6$, $h/\lambda_x = 0.1$ d) $r = 8$, $h/\lambda_x = 0.1$ e) $r = 10$, $h/\lambda_x = 0.1$. $s = 0$ corresponds to entry of pycnocline downstream.

In the table 5.1, the energy flux evolution is normalized with respect to the maximum energy flux along IWB for that particular case. Besides, the optimal configuration for the mean flow generation occurs around $r = 8$ for $h/\lambda_x = 0.1$ and $Re = 530$. Differing from the first harmonic signal, the mean flow survives further inside the pycnocline as it does not show oscillatory motion as the harmonics and the primary frequency wave do. The optimal configuration is achieved by the balance between the viscous loss and the accumulation of the energy inside the pycnocline. The harmonic generation could be enhanced by decreasing the viscosity. To observe the effect of the viscous loss, the Reynolds number is increased to $Re = 5300$. As the viscosity calculation shows, it significantly reduces the viscous loss along IWB, however it does not affect the viscous dissipation inside the triangular region as much. Nonetheless, it still increases the energy flux into the downstream pycnocline. For the reduced viscosity simulations, the optimal configuration is again achieved at $r = 6$ for the first harmonic generation. The amount of the energy flux transferred to the first harmonic is around 6% of the maximum energy flux along IWB. Even though the first harmonic signal is noticeable, higher order harmonics are still negligible in the reduced viscosity simulations as the effect of the viscosity is still strong inside the pycnocline.

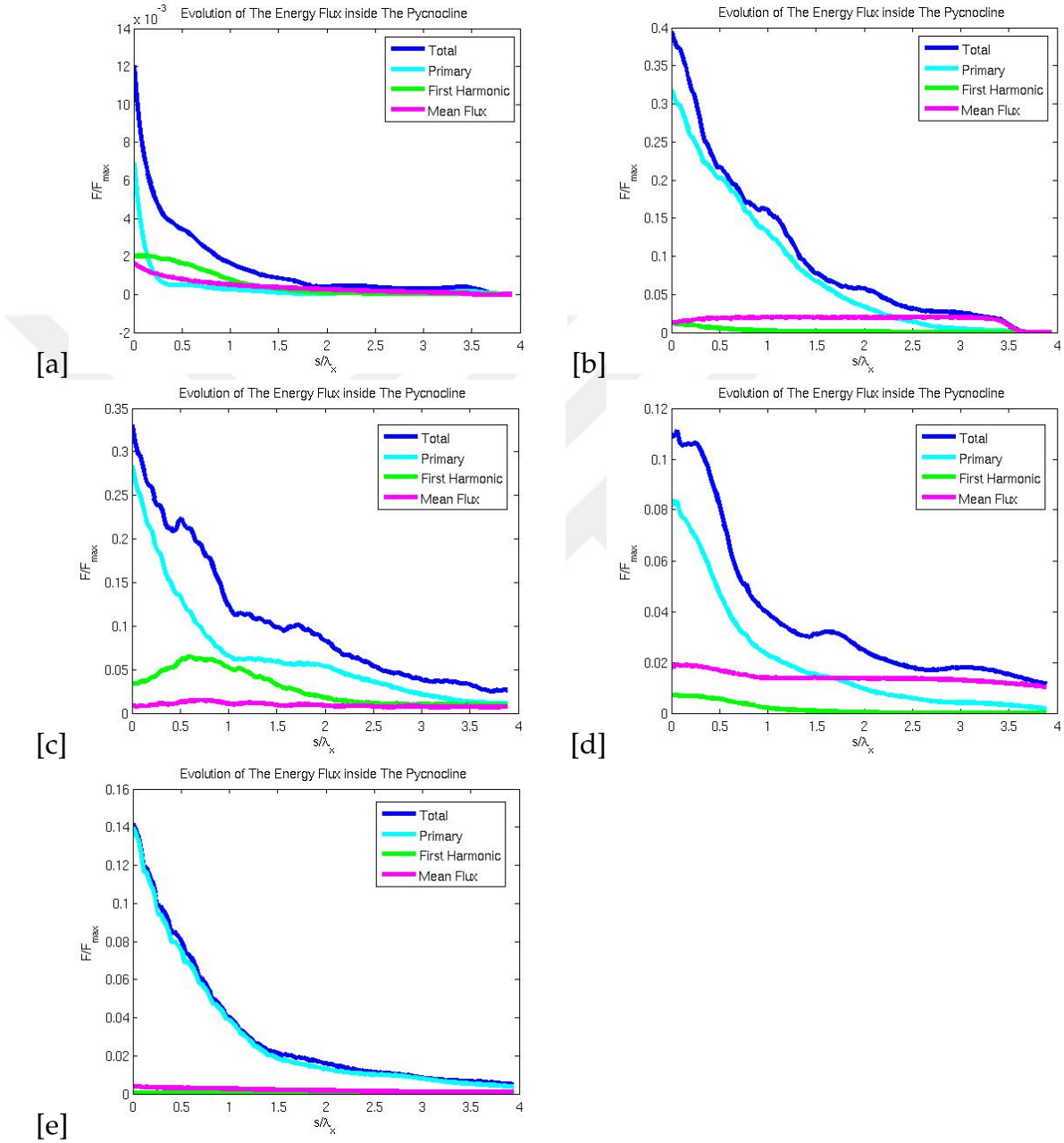

Figure 5.12: Energy flux evolution inside pycnocline for $Re = 5300$ a) $r = 2$, $h/\lambda_x = 0.1$ b) $r = 4$, $h/\lambda_x = 0.1$ c) $r = 6$, $h/\lambda_x = 0.1$ d) $r = 8$, $h/\lambda_x = 0.1$ e) $r = 10$, $h/\lambda_x = 0.1$.$s = 0$ corresponds to entry of pycnocline downstream.

5.6 Re-Radiating Energy from Pycnocline

The majority of the wave energy is reflected back into the lower layer at the first reflection. However, some part of the energy flux gets trapped inside the pycnocline, the harmonics signal trapped inside the pycnocline can not re-radiate back into the lower layer as it reaches another critical level of reflection around the base of the pycnocline. There is also another critical level of reflection at the top of the pycnocline, therefore the pycnocline acts as a wave-guide for the first harmonic signal.

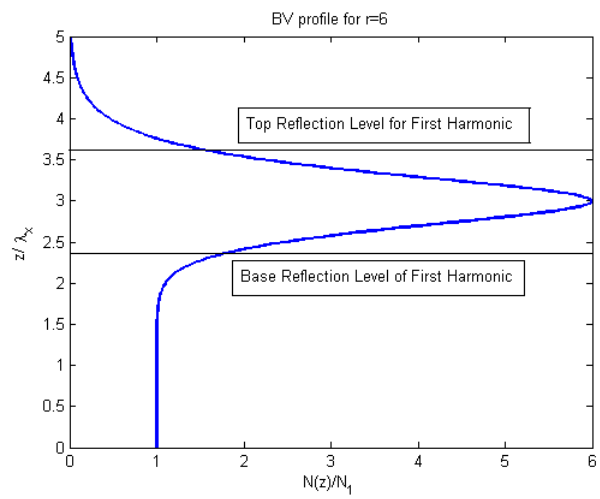

Figure 5.13: BV frequency profile for $r = 6$ and $h/\lambda_x = 0.1$ and The Top and The Bottom Reflection Levels at which $N(z_r) = 2\omega$.

For the particular configuration, the harmonics energy can not re-radiate back into the lower layer. However, it may interact nonlinearly with the primary frequency internal wave beam and it may transfer its energy to the primary frequency wave [5]. The energy flux transferred to the primary wave may re-radiate back into the lower layer. This is the another way of how the energy flux trapped inside the pycnocline dissipates. In the case of the reduced viscosity, the energy flux re-radiating back into the lower layer increased negligibly

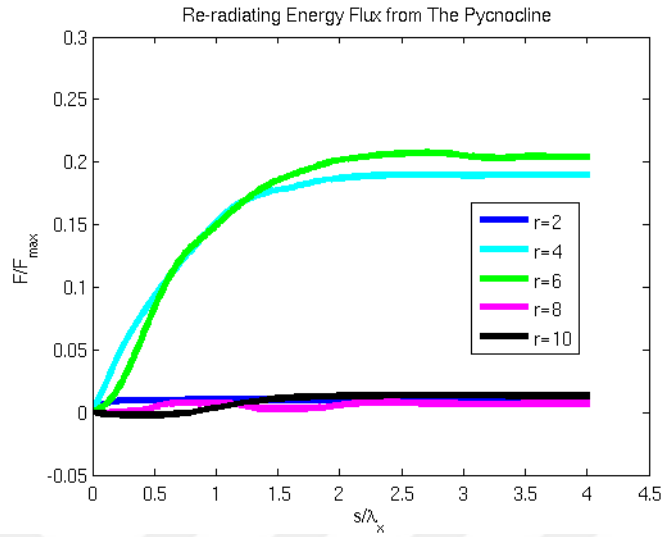

Figure 5.14: The reradiating energy flux from the pycnocline for $r = 2, 4, 6, 8, 10$, $h/\lambda_z = 0.1$ and $Re = 530$.

as the total viscous dissipation does not change so that the re-radiating energy flux stays similar to the high viscosity case.

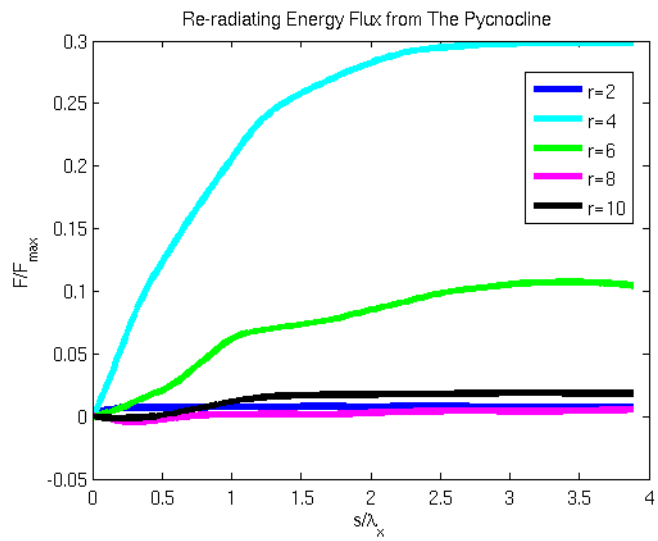

Figure 5.15: The reradiating energy flux from the pycnocline for $r = 2, 4, 6, 8, 10$, $h/\lambda_z = 0.1$ and $Re = 5300$.

CHAPTER 6

DISCUSSION

Briefly, harmonics and mean flow are generated by the inciedent and the reflecting internal wave beam overlap. The harmonic and the mean flow generation is derived analytically in the framework of the colliding internal waves [5]. The same generation mechanism occurs in the case of pycnocline, the interaction between the incident and the reflectin internal wave beam generates them. Free-slip surface reflection case is a useful starting point to analyze the generation mechanism inside the pycnocline. Differing from the free-slip surface reflection case, internal wave beam starts refracting in the entrance of the pycnocline which complicates the physics. The primary frequency incident wave reaches the reflection level and it reflects back into the lower layer. However, the incident and the reflecting internal wave beam interacts in the overlap region. To isolate the effect of the internal wave beam overlap from the internal wave refraction, it should be analyzed in a uniform stratification and in the presence of the reflection surface. In the previous research, this situation is simulated and the result are generated for an internal wave beam propagating with 45° angle. It simply simulates the effect of the beam overlap. Nonetheless, it is not very useful to understand the harmonics generation for the angle of propogation analyzed 45°. As mention before, harmonic signal becomes evanescent due to $N < n\omega$ restriction. The harmonics generation could also be observed for lower angle of propartion. However, it is very useful to verify the structure of the mean flow generated by the internal wave beam overlap. The nonlinear forcing due to the incident and the reflecting beam overlap is derived in the equations (4.31), (4.35). These equation show that the mean flow should have sinusoidal structure with a wavelength $\lambda_z/2$. The results presented in the figure

(6.1) verifies the effect of the incident and the reflecting beam overlap.

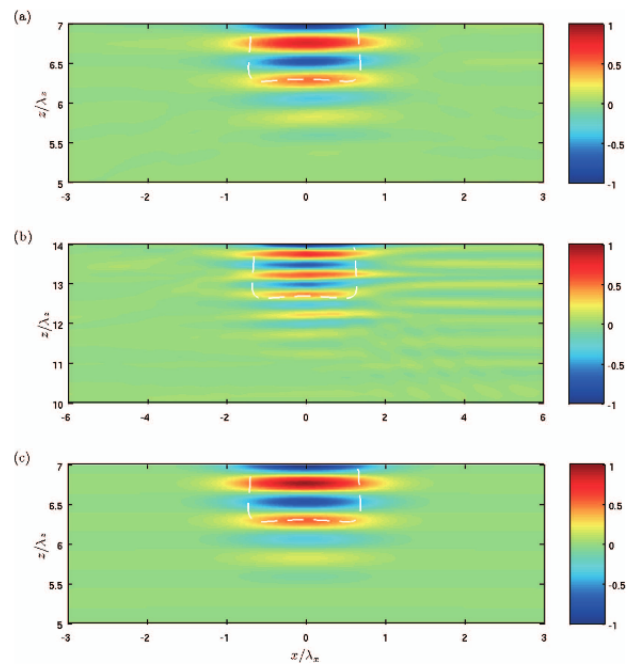

Figure 6.1: xz-contours of mean horizontal velocity $< u >$, normalized by its maximum observed magnitude in space, (a) at $t/T = 30$ for T01, and (b) at $t/T = 45$ for T07, in the wave reflection zone. The prediction by inviscid weakly nonlinear theory19 for a same wave geometry as T01, is shown in (c). The reflecting surface is at the top boundary of each contour plot and the centerline of the wave beam intersect with the surface at x = 0. The superimposed white dashed line is the contour of temporally averaged local intensity of wave kinetic energy $\rho_0(< u^2 > + < w^2 >)/2$ at 120%of the corresponding value on the centerline of the incident (reflected) beam outside the reflection zone [7].

Even though the presence of the pycnocline complicates the situtaion, the generation mechanism is the same. In the case of pycnocline, there is a reflection layer instead of the free slip surface. It causes the internal wave reflection. At the reflection level, the background BV frequency N matches the internal wave frequency ω. After that reflection occurs, the incident and the reflecting beam interact inside the overlap region as it is schematically shown in figure (1.3). The

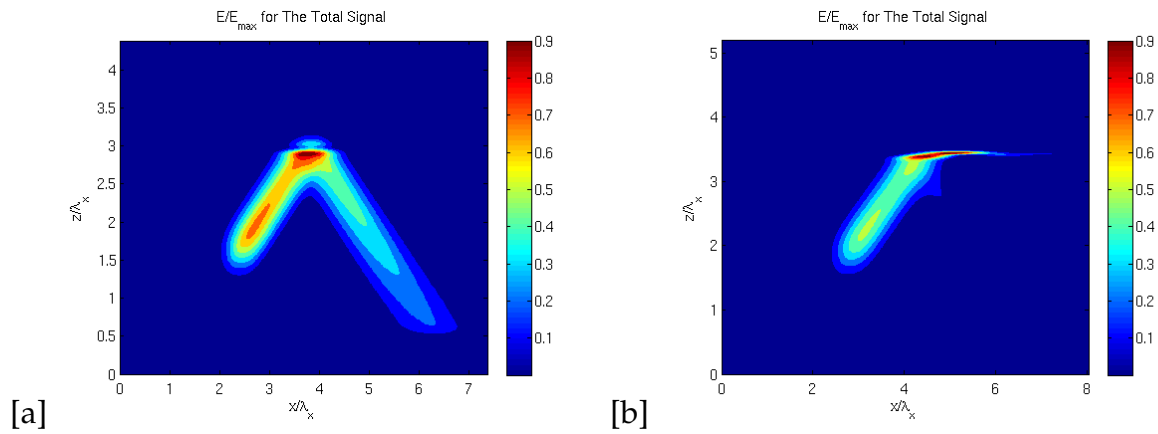

Figure 6.2: Mean energy intensity for $Re = 530$ a) $r = 2$, b) $r = 4$.

similar physics for the generation mechanism happens in the case of the pycnocline. However, the presence of the pycnocline changes both orientation and the magnitude of the group velocity which causes the wave refraction and the accumulation of the internal wave energy in some layers in which the group velocity decreases when the simulation reaches steady-state. The internal wave energy amplitude also increases with that energy accumulation in that particular layer. The internal wave accumulation occurs both for the incident and the reflecting internal wave beam. In our case, the group velocity in z direction decreases considerably inside the pycnocline as shown in figure (5.8). The harmonics and the mean flow generation is dependent on the product of the incident and the reflection internal wave beam amplitude as given in the equations (4.61), (4.63).

However the total energy accumulation is not just dependent on the varying group velocity. The internal wave amplitude could diminish due to the viscous losses. Those viscous losses are more effective inside the pycnocline as they are strongly dependent on the background BV frequency as given in the equation (4.19). Note that in the derivation of the equation (4.19), the effect of the reflec-

tion in accounted.

In the balance between the effect of the varying group velocity and the viscous losses, there is an optimal configuration for the nonlinear interaction. This optimal confiugration can be roughly observed by checking the energy intensity distribution of the internal wave field. As shown in the figure (6.2b), the energy inside the pycnacline more intense than the energy along IWB for $r = 6$ and $h/\lambda_x = 0.1$. However, in the case of $r = 2$ and $h/\lambda_x = 0.1$, the energy accumulation is not as high as $r = 6$ and $h/\lambda_x = 0.1$ as shown in the figure (6.2a). As given in the figure (5.11), it directly affects the amount of the harmonic and the mean flow energy generated. In the mean flow generation, it could also be observed it has both forward and backward propagating parts. That type of generation mechanicsm also observed in the colliding internal waves[5]. The pycnocline also affects the fate of the harmonic generated for the particular angle of propagation analyzed in the simulations, the first harmonic reaches the reflection levels both at the base and the top of the pycnocline at which $N = 2\omega$. Because of this, the harmonics generated gets trapped inside the pycnocline. It causes a reflection pattern of the harmonics inside the pycnocline. During those reflections, it interacts nonlinearly with the primary frequency wave and itself which generates the higher order harmonics and transfers energy into the primary frequency wave. The higher harmonics decays rapidly due to viscous effects. The energy transfered to the primary frequency wave may re-radiate back into the lower layer. Because of this and the fact that the mean flow losses less energy due to viscosity, the mean flow generated by the nonlinear interactions survives longer inside the pycnocline as shown in the figures (5.12b) and (5.11b). In the reduced viscosity simulation, the viscous loss decreased considerably along IWB, however it is still very effective inside the pycnocline due to

the focusing effect. In the reduced viscosity simulations, for $r = 8$ and $r = 10$, initially simulation did not yield a stable solution. To figure it out, the order of the spectral filter increased. It leads to a gap in the energy budget table.

CHAPTER 7

CONCLUSION AND THE FUTURE WORK

7.1 Conclusion

Harmonic and mean flow generation is analyzed in the study. It is done by analytical models and numerical simulations. Analytical model for the viscous decay shows an agreement with numerically computed viscous dissipaton despite the fact that it has some limitations like it can not capture the reflecting part of the internal wave beam. Moreover, the analytical model given by equations (4.61), (4.63) is not solve analytically, however it still gives important insight about the mean flow and harmonic generation. It shows that the rate of generation of both first harmonic and mean flow is correlated the product of the incident and the reflecting internal wave beam amplitude. Additionally, the amplitude of the internal wave is dependent on the amount of the energy accumulated on the region. The presence of the pycnocline leads to both energy accumulation around a particular region inside the pycnocline and it also causes an internal wave reflection. The effect of the energy accumulation increases with increasing r value as shown in figure (5.8). At the same time, the stronger pycnocline cause higher viscous dissipation as it increases the wavenumber which is also shown analytically. Nonetheless, analytical models don't give exact numerical results. In this way, the numerical simulations are performed for $r = 2, 4, 6, 8, 10$ and $Re = 530$ at $h/\lambda_x = 0.1$. The optimal configuration for the harmonic generation occurs are $r = 6$ in the thin pycnocline $h/\lambda_x = 0.1$ for the mean flow and the harmonic generation in the balance of the energy accumulation and the viscous loss. Some part of energy flux reflects back

into lower layer in the first reflection and some re-radiates back into the lower layer from the downstream pycnocline. The re-radiating part of the energy flux is enhanced by the interaction between the primary frequency wave and the first harmonics as it leads to and energy tranfer from the first harmonic to the primary frequency wave. Since there is another reflection level at the base of the pycnocline, only primary frequency wave can re-radiate back into the lower layer. The top and the base reflection layers for the first harmonic acts as a wave guide. The harmonic waves decays much faster than the mean flow as it shows oscillatory behavior which leads to higher viscous losses. In the reduced viscosity simulations, there is a significant reduction in the viscous loss along IWB, however inside the pycnocline, the viscosity is still very effective. It still leads to an increase in the first harmonic generation from 4% to 6% in $r = 6$ case, even though it dissipates quickly in both $Re = 530$ and $Re = 5300$ cases. Even though the mean flow generation at $r = 4$ case is not as strong, it survives further inside the pycnocline. The rate of the first harmonic generation is also affected by the phase difference between the incident and the reflected internal wave beam as given in the equation (4.61). The same argument applies for the mean flow generation as given in the equation (4.63). In those equation wave amplitude is not explicity dependent on the group velocities, however it is implicitly dependent on them via slow variables given in the derivation.

7.2 Future Work

The ideas developed could be improved further. First, the analytical model can be refined even further under further simplifying assumptions. One idea is to use an heat kernel and integrate it along the Ray paths via the convolution in-

tegral. It will gives us the Gaussianity required by the simulations. In terms of the simulations, to observe the propagation of harmonics in the lower layer, shallower angle of propagations could be run. In that case, the harmonics may survive longer as the effect of the viscous losses are less dominant in the lower layer. Furthermore, It is clearly observed viscous loss leads to significant energy loss. To get rid of the effect of viscous loss, inviscid simulations can be performed. The effect of wave steepening on harmonics generation can be tested, although it may cause an instability. In this study, the Coriolis effect and the background shear is not included, however these effects are considerable in real application. They can also be added to the current analysis. Moreover, the main generation mechanism is found to be the incident and the reflecting internal wave beam overlap, similar generation can be simulated by transverse localization of IWB.

APPENDIX A

SUPPLEMENTARY FIGURES

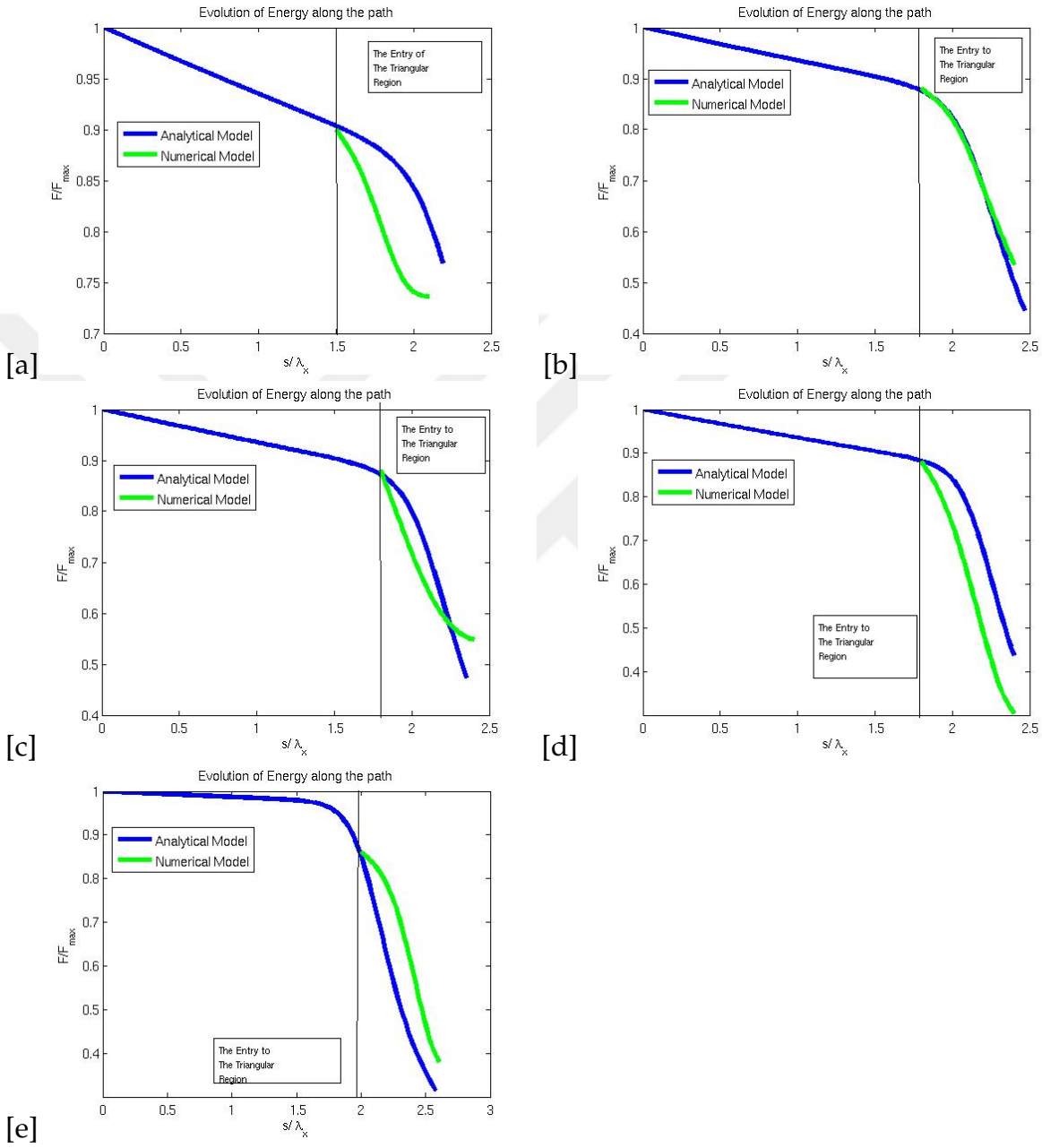

Figure A.1: Viscous dissipation inside triangular region numerical vs analytical Calculations for $Re = 530$ a) $r = 2$, $h/\lambda_x = 0.1$ b) $r = 4$, $h/\lambda_x = 0.1$ c) $r = 6$, $h/\lambda_x = 0.1$ d) $r = 8$, $h/\lambda_x = 0.1$ e) $r = 10$, $h/\lambda_x = 0.1$.

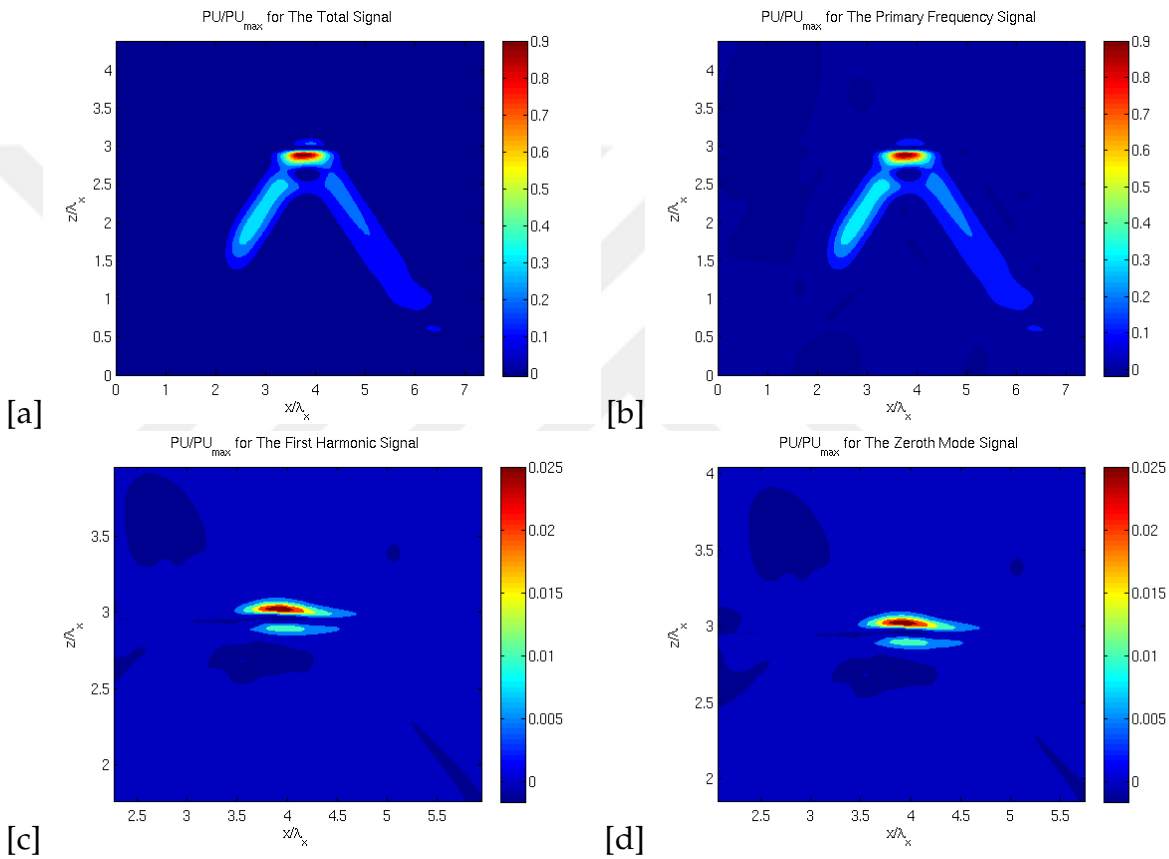

Figure A.2: Mean pressure velocity product for $r = 2$ and $Re = 530$a) PU_{Total}/PU_{max}, b) PU_{ω}/PU_{max}, c) $PU_{2\omega}/PU_{max}$ magnified, d) PU_{mean}/PU_{max} magnified.

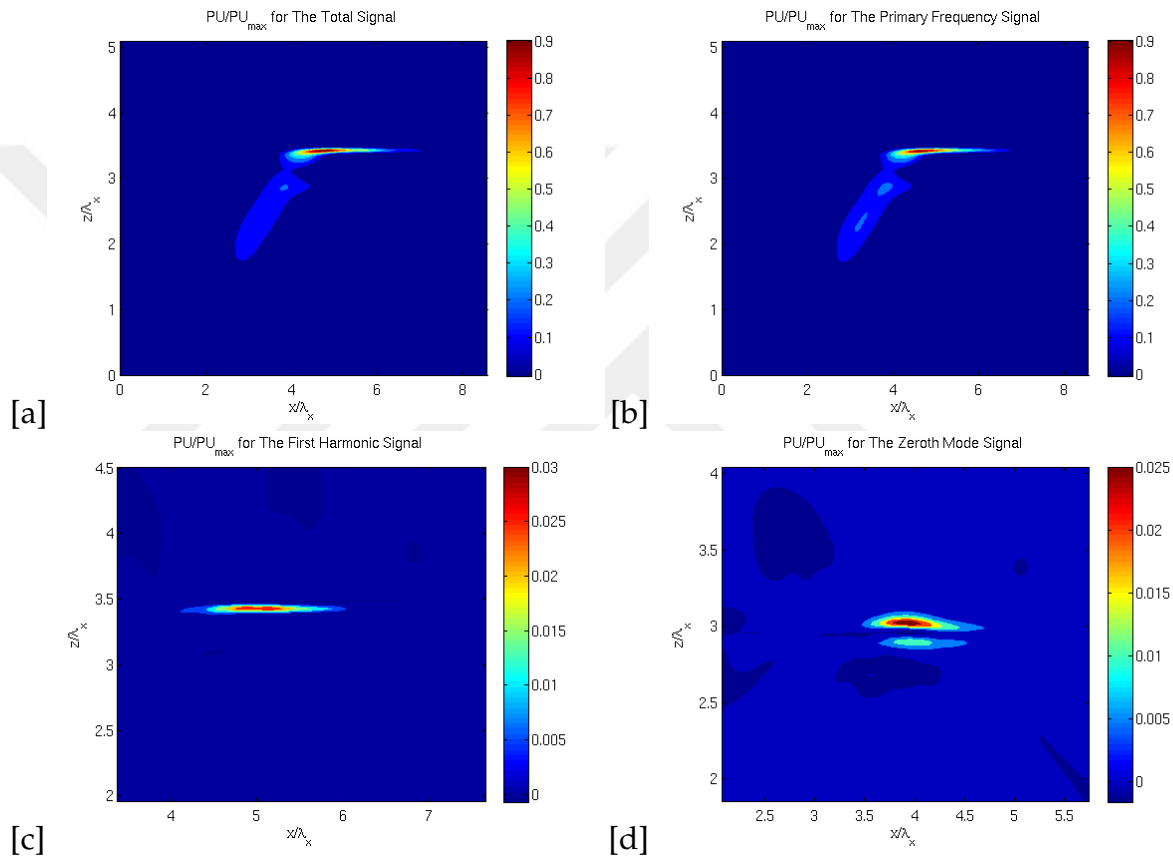

Figure A.3: Mean pressure velocity product for $r = 4$ and $Re = 530$ a) PU_{Total}/PU_{max}, b) PU_{ω}/PU_{max}, c) $PU_{2\omega}/PU_{max}$ magnified, d) PU_{mean}/PU_{max} magnified.

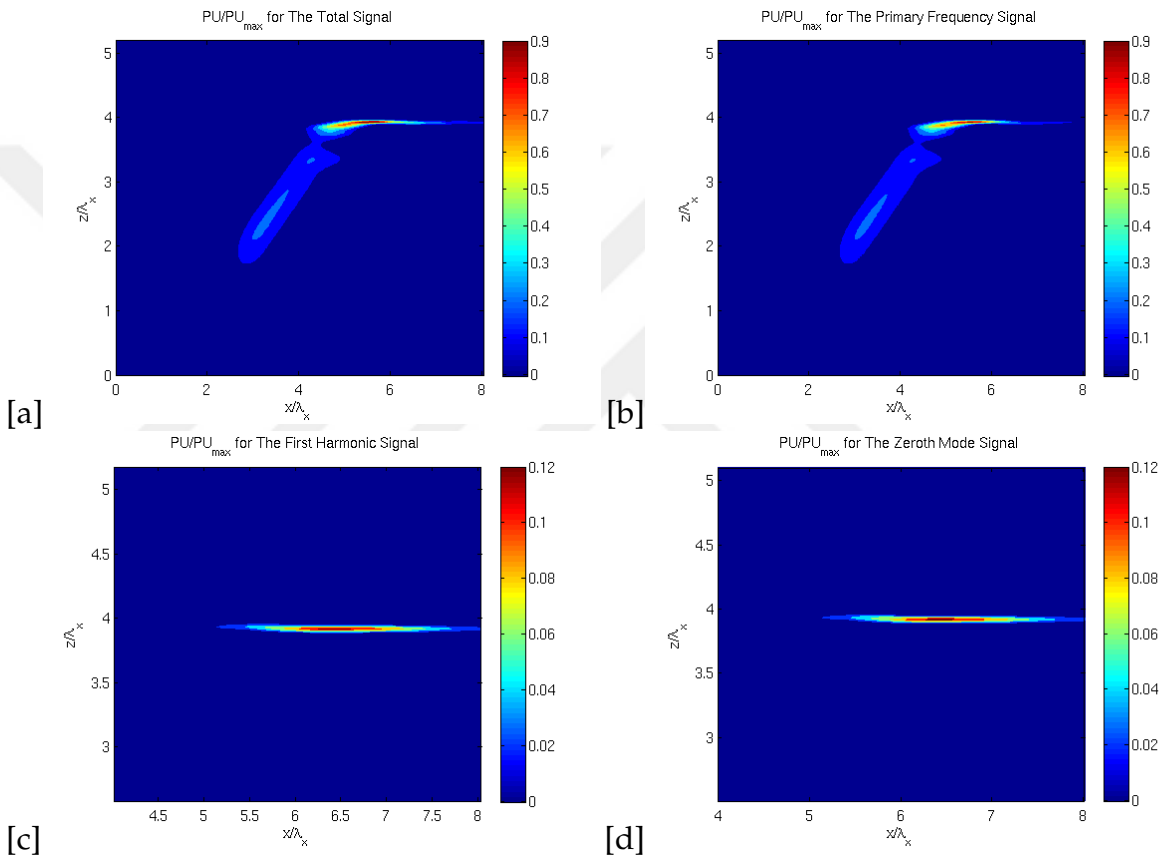

Figure A.4: Mean Pressure Velocity Product for $r = 6$ and $Re = 530$ a) PU_{Total}/PU_{max}, b) PU_{ω}/PU_{max}, c) $PU_{2\omega}/PU_{max}$ magnified, d) PU_{mean}/PU_{max} magnified.

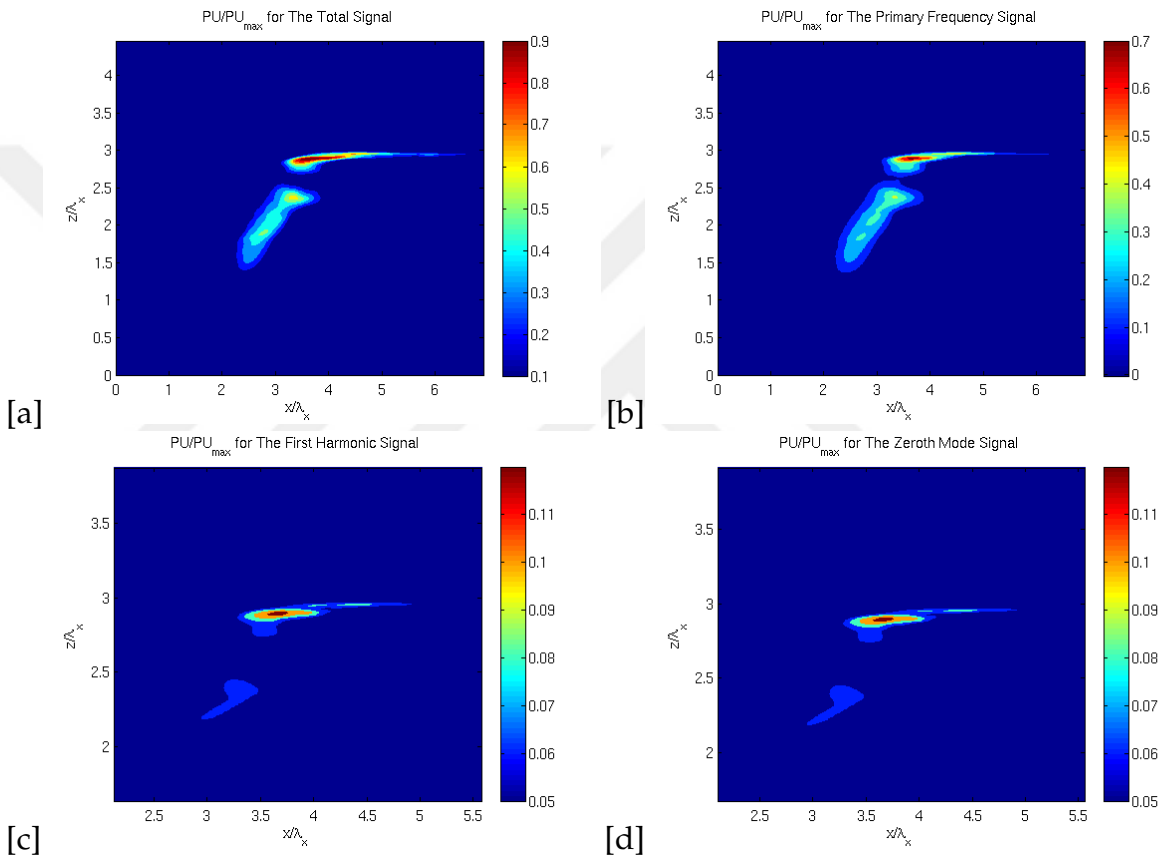

Figure A.5: Mean pressure velocity product for $r = 8$ and $Re = 530$ a) PU_{Total}/PU_{max}, b) PU_{ω}/PU_{max}, c) $PU_{2\omega}/PU_{max}$ magnified, d) PU_{mean}/PU_{max} magnified.

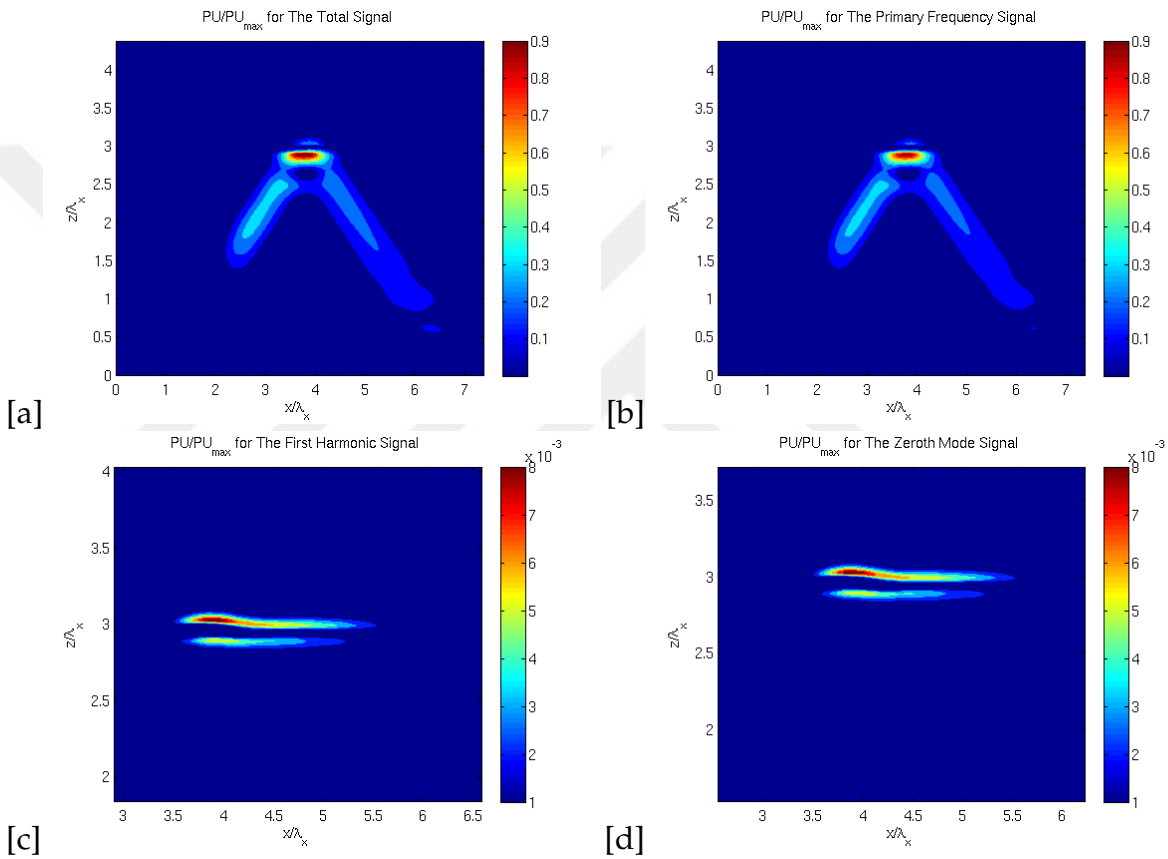

Figure A.6: Mean pressure velocity product for $r = 2$ and $Re = 5300$ a) PU_{Total}/PU_{max}, b) PU_{ω}/PU_{max}, c) $PU_{2\omega}/PU_{max}$ magnified, d) PU_{mean}/PU_{max} magnified.

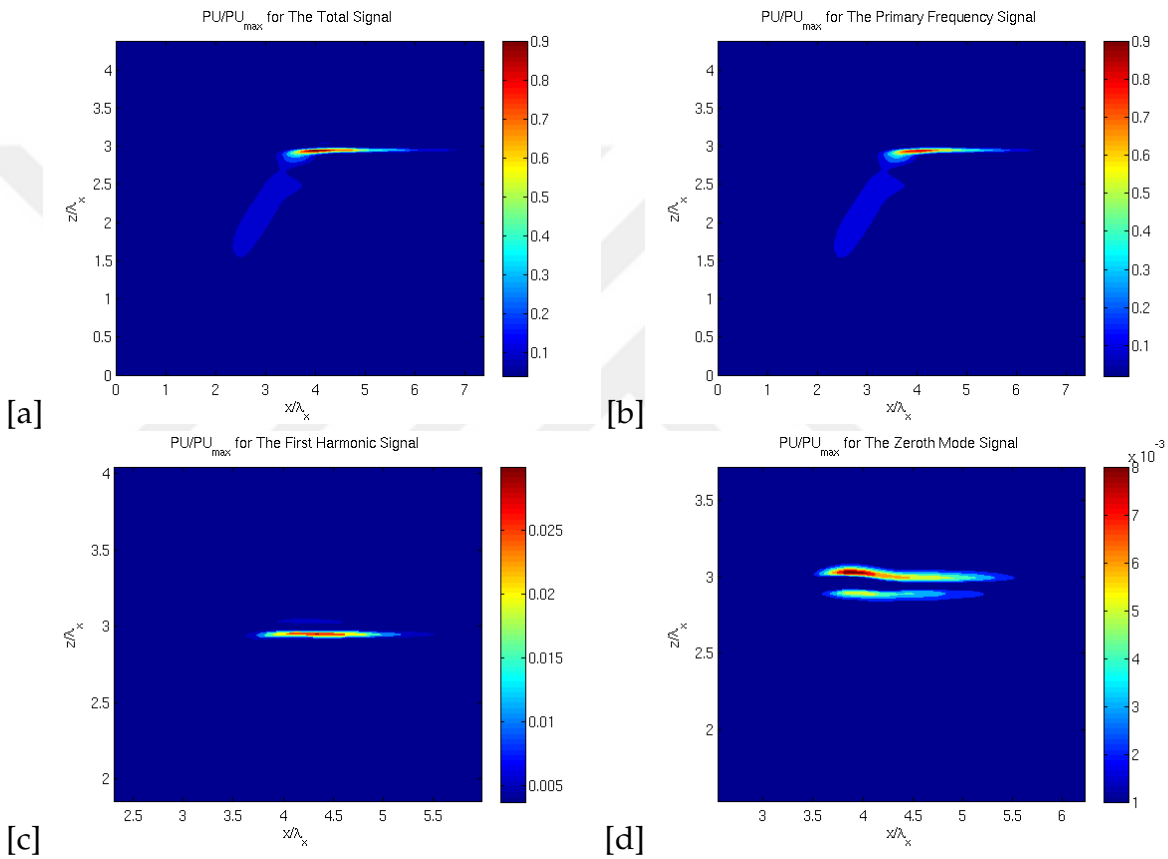

Figure A.7: Mean pressure velocity product for $r = 4$ and $Re = 5300$ a) PU_{Total}/PU_{max}, b) PU_{ω}/PU_{max}, c) $PU_{2\omega}/PU_{max}$ magnified, d) PU_{mean}/PU_{max} magnified.

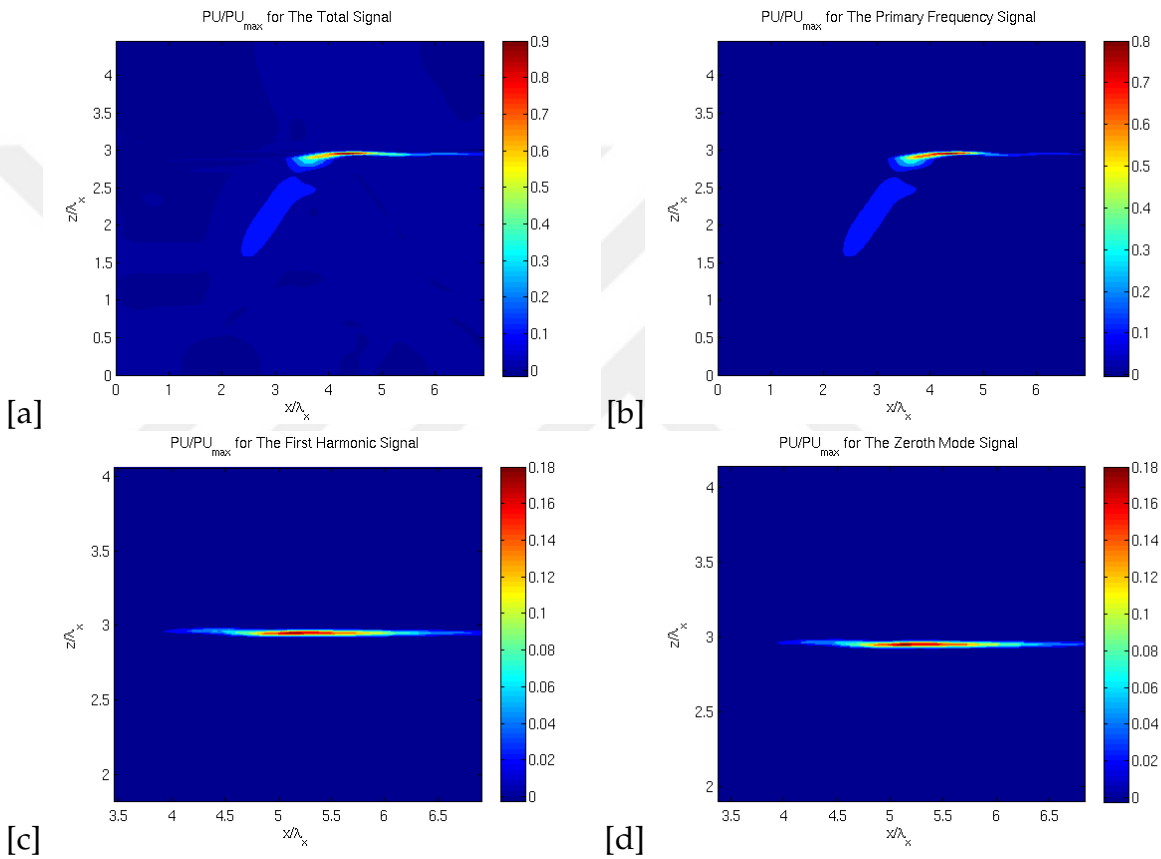

Figure A.8: Mean pressure velocity product for $r = 6$ and $Re = 5300$ a) PU_{Total}/PU_{max}, b) PU_{ω}/PU_{max}, c) $PU_{2\omega}/PU_{max}$ magnified, d) PU_{mean}/PU_{max} magnified.

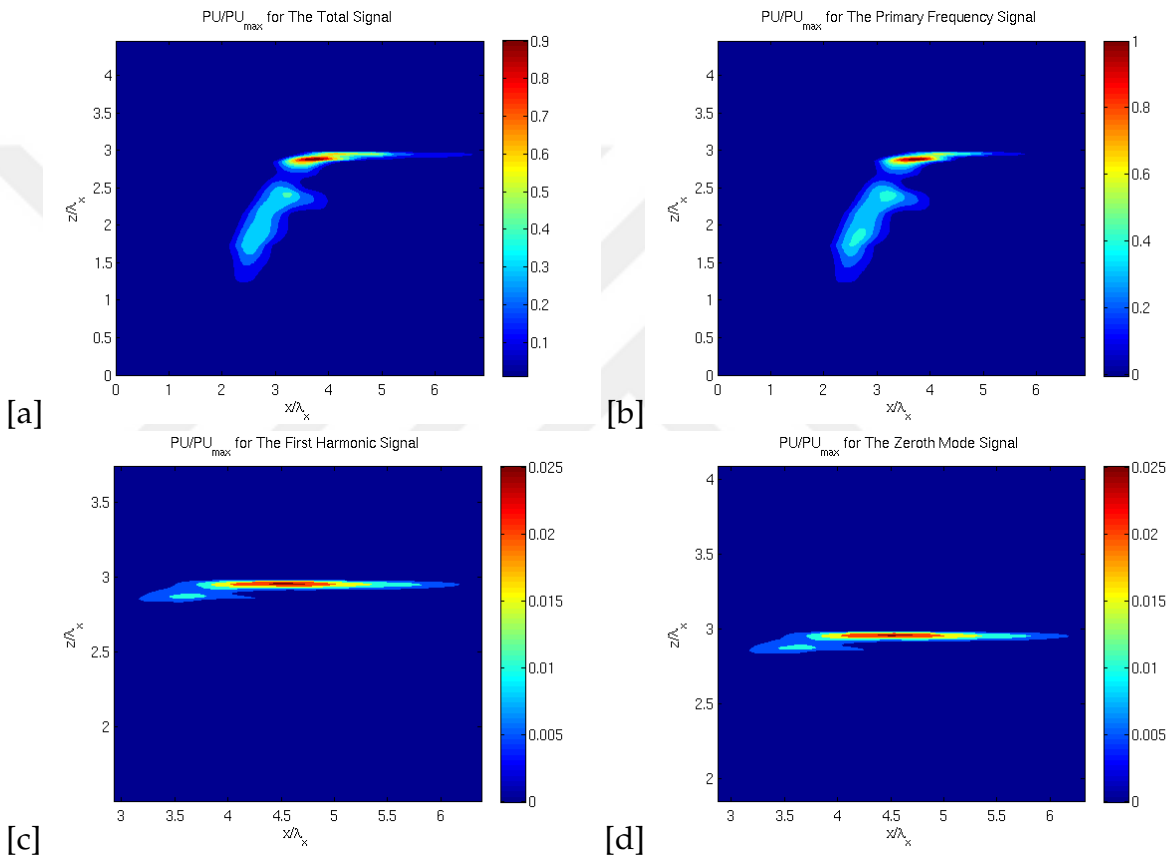

Figure A.9: Mean pressure velocity product for $r = 8$ and $Re = 5300$ a) PU_{Total}/PU_{max}, b) PU_{ω}/PU_{max}, c) $PU_{2\omega}/PU_{max}$ magnified, d) PU_{mean}/PU_{max} magnified.

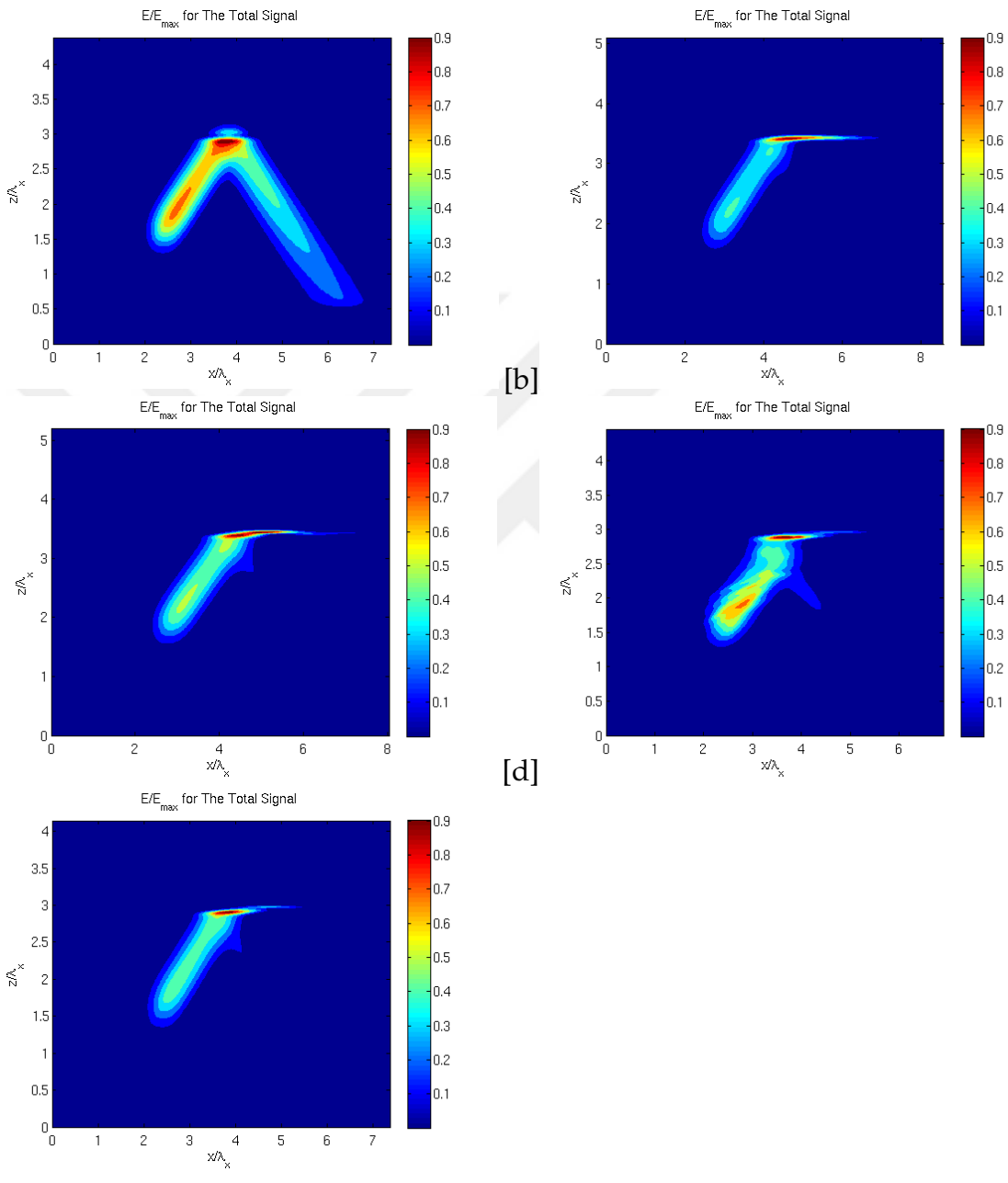

Figure A.10: Mean energy Intensity for $Re = 530$ a) $r = 2$, b) $r = 4$, c) $r = 6$, d) $r = 8$, e) $r = 10$.

APPENDIX B

THE VIRTAUL FORCING REGION

In the equations (2.1) and (2.2), the virtaul forcing terms are denoted as $\mathbf{F_u}$ and $\mathbf{F}_\rho$. Let's denote F_u for the forcing in x momentum equation and F_w for the forcing in z momentum equation. The same formulation is used as Zhou and Diamssis [7]:

$$F_u = \frac{U_f}{T}(-F\frac{k_z}{k_x}\cos\phi - \frac{\partial F}{\partial z}\frac{1}{k_x}\sin\phi + \frac{\partial F}{\partial x}\frac{k_z}{k_x^2}\sin\phi), \tag{B.1}$$

$$F_w = \frac{U_f}{T}F\cos\phi, \tag{B.2}$$

$$F_\rho = -\left|\frac{\mathrm{d}\bar{\rho}}{\mathrm{d}z}\right|\frac{U_f}{\omega_0 T}F\sin\phi. \tag{B.3}$$

where $\phi = k_x x - k_z z - \omega_0 t$, U_f is the reference velocity scale and T is the wave period. The gaussian forcing region is used to excite the localized wave packets [7].

$$F(x,z) = \exp[-\frac{(x-x_{cen})^2}{2\sigma_x^2} - \frac{(z-z_{cen})^2}{2\sigma_z^2}]. \tag{B.4}$$

The reference velocity is determined so that in the high viscosity simulations, the wave steepness could be arranged for the appropriate values at which wave would not steepen along IWB.

BIBLIOGRAPHY

[1] Bruce Sutherland, *Internal Gravity Waves.* Cambridge University Press 2010.

[2] Thorpe, *The Turbulent Ocean.* Cambridge University Press 2005.

[3] P. J. Diamessis, S. Wunsch, I. Delwiche, P. Richter, *Nonlinear generation of harmonics through thee interaction of an internal wave beam with a model oceanic pycnocline.* Dyn. of Atm. and Oceans. (2014)

[4] Chris Garrett, Eric Kunze *Internal Tide Generation in the Deep Ocean.* Annu. Rev. Fluid Mech. 39 57-87 (2007).

[5] Ali Tabaei, T. R. Akylas and Kevin G. Lamb *Nonlinear effects in reflecting and colliding internal wave beams.*J. Fluid Mech. 526, 217-243 (2005).

[6] A. M. Abdilghanie, *A Numerical Investigation of Turbulence-driven and Forced Generation of Internal Gravity Waves in Stratified Mid-water.* Ph.D. dissertation, Cornell University, Ithaca, New York, 2010.

[7] Qi Zhou and Peter J. Diamessis, *Reflection of an internal gravity wave beam off a horizontal free-slip surface.* Physics of Fluids 25 0366601 (2013).

[8] Scott Wunsch, Ian Delwiche, Gary Frecerick, Alan Brandt, *Experimental study of nonlinear harmonic generation by internal waves incident on a pycnocline.* Exp. Fluids 86 5 87 (2015)

[9] Scott Wunsch, Alan Brandt, *Laboratory experiments on internal waves interactions with a pycnocline.* Exp. Fluids 53 1663-1679 (2012).

[10] M. Mathur, T. Peacock, *Internal wave beam propagation in nonuniform stratifications.* J. Fluid Mech. 638 133-152 (2009).

[11] T. Gerkema, *Internal and interfacial tides: Beam scattering and local generation of solitary waves.* J. Mar. Res. 59, 227-255 (2001).

[12] G. Bordes, A. Venaille, S. Joubaud, P. Odier, T. Dauxois, *Experimental observation of a strong mean flow induced by internal gravity waves.* Phys. Fluids. 24 086602 (2012).

[13] Y. Dossmann, F. Auclair, A. Paci, *Topographically induced internal solitary waves in a pycnocline: secondary generation and selection criteria.* Phys. Fluids 25 (2013).

[14] N. Grisouard, C. Staquet, *Numerical Simulations of the local generation of internal solitary waves in the Bay of Biscay.* Nonlin. Proc. Geoph. 17, 575-584 (2010).

[15] N. Grisouard, C. Staquet, T. Gerkema *Generation of internal solitary waves in a pycnocline by an internal wave beam: a numerical study.* J. Fluid Mech. 676 491-513 (2011).

[16] N. H. Thomas, T. N. Stevenson, *A similarity solution for viscous internal waves.* J. Fluid Mech. 54 495-506 (1972).

[17] Ali Tabaei, T. R. Akylas, *Nonlinear internal gravity wave beams.* J. Fluid Mech. 482 141-161 (2003)

[18] Bruce Sutherland, *Finite-amplitude internal wavepacket dispersion and breaking.* J. Fluid Mech. 429 343-380 (2001).

[19] S. J. Ghaemsaidi, *Interference and resonance of internal gravity waves.* Ph.D. dissertation, MIT, Cambridge, Massachussets, 2015.

[20] B. Gayen, S. Sarkar, *Degradation of an internal wave beam by parametric subharmonic instability in an upper ocean pycnocline* J. Geophys. Res. 118, 4689-4698 (2013).

[21] C. Garrett, W. Munk, *Internal Waves in the ocean.* Ann. Rev. of Fluid Mech. 11, 339-369 (1979).

[22] S. Wunsch, H. Ku, I. Delwiche, R. Awadallah, *Simulations of nonlinear harmonic generation by an internal wave beam incident on a pycnocline.* Nonlinear Proc Geophys 21 855-868 (2014).

[23] D. Aguilar, Bruce Sutherland, D. J. Muraki, *Generation of Internal Waves over Sinusoidal Topography.*, Deep Sea Res. II (2006).

[24] J. C. B. da Silva, M. C. Bujisman, J. M. Magalhaes, *Internal waves on the upstream side of a large sill of the Mascarene Ridge: a comprehensive view of their generation mechanisms and evolution*, Deep-Sea Research Part 1 Oceanographic Research Papers 99 87-104 (2015).

[25] T. R. Akylas, R. H. J. Grimshaw, S. R. Clarke, Ali Tabaei, *Reflecting tidal wave beams and local generation of solitary waves in the ocean thermocline*, J. Fluid Mech. 593, 297-313 (2007).

[26] X. Xien, X. Shang, H. van Haren, G. Chen, *Observations of enhanced nonlinear instability in the surface reflection of internal tides.*, Geophys. Res. Lett. 40, 1580-1586 (2013).

[27] A. Azevedo, J. C. B. da Silva, A. L. New, *On the generation and propagation of internal solitary waves in hte southern Bay of Biscay.*, Deep-Sea Res. 1 53, 927-941 (2006).

[28] B. Rodenborn, D. Kifer, H. P. Zhang, H. L. Swiney, *Harmonic generation by reflecting internal waves*, Phys. Fluids 23 (2011).

[29] G. E. Karniadakis, M. Israeli, S. A. Orszag. *High-order splitting methods for the incompressible Navier-Stokes equations.* J. Comput. Phys. 97 414443 (1991).

[30] P. K. Kundu ,I. M. Cohen, *Fluid Mechanics.* Academic Press, San Diego, (2004).

[31] S. Wunsch, K. Keller, *Unstable modes of a sheared pycnocline above a stratified layer.* Dyn. Atmos. Ocean 60, 1-27 (2013).

[32] J. Lighthill, *Waves in Fluids.* Cambridge University Press, New York, 1978.

[33] P. Bonneton, J. M. Chomaz, E. J. Hopfinger, *Internal Waves produced by the turbulent wake of a sphere moving horizontally in a stratified fluid.* Journal Fluid Mech 254, 23-40 (1993).